The AMIGO1 adhesion protein modulates movement of Kv2.1 voltage sensors

Condensed Title: AMIGO1 modulates Kv2.1 voltage sensors

Rebecka J. Sepela[1], Robert G. Stewart[1], Luis A. Valencia[3], Parashar Thapa[1], Zeming Wang[3], Bruce E. Cohen[3,4], Jon T. Sack[1,2*]

[1]Department of Physiology and Membrane Biology, University of California, Davis, CA 95616
[2]Department of Anesthesiology and Pain Medicine, University of California, Davis, CA 95616
[3]Molecular Foundry, Lawrence Berkeley National Laboratory, Berkeley, CA 94720
[4]Division of Molecular Biophysics & Integrated Bioimaging, Lawrence Berkeley National Laboratory, Berkeley, CA 94720

*Correspondence to Jon T. Sack: jsack@ucdavis.edu
(ORCID https://orcid.org/0000-0002-6975-982X)
1 Shields Ave. 4148 Tupper Hall. Davis, California 95616

Summary

This work investigates the functional mechanism by which the AMIGO1 adhesion protein modulates the conductance of the Kv2.1 channel subtype. We find that AMIGO1 acts by altering movement of the voltage sensors and detabilizing their earliest resting conformation.

Abstract

Voltage-gated potassium (Kv) channels sense voltage and facilitate transmembrane flow of K^+ to control the electrical excitability of cells. The Kv2.1 channel subtype is abundant in most brain neurons and its conductance is critical for homeostatic regulation of neuronal excitability. Many forms of regulation modulate Kv2.1 conductance, yet the biophysical mechanisms through which the conductance is modulated are unknown. Here, we investigate the mechanism by which the neuronal adhesion protein AMIGO1 modulates Kv2.1 channels. With voltage clamp recordings and spectroscopy of heterologously expressed Kv2.1 and AMIGO1 in mammalian cell lines, we show that AMIGO1 modulates Kv2.1 voltage sensor movement to change Kv2.1 conductance. AMIGO1 speeds early voltage sensor movements and shifts the gating charge–voltage relationship to more negative voltages. Fluorescence measurements from voltage sensor toxins bound to Kv2.1 indicate that the voltage sensors enter their earliest resting conformation, yet this conformation is less stable upon voltage stimulation. We conclude that AMIGO1 modulates the Kv2.1 conductance activation pathway by destabilizing the earliest resting state of the voltage sensors.

Introduction

Voltage–gated potassium (Kv) channel proteins of the Kv2 family are critical regulators of neuronal electrical excitability. Kv2 channels are abundant (Vacher et al., 2008) homo- or heterotetramers of pore forming α subunits (Bocksteins, 2016; Kihira et al., 2010; Trimmer, 1993). The molecular architecture of Kv2.1 channels is similar to Kv1 channels for which atomic resolution structures have been solved (Long et al., 2005, 2007). Each α subunit monomer has six transmembrane helical segments, S1-S6. S1-S4 comprise a voltage sensor domain (VSD) while S5 and S6 together form one quarter of the central pore domain. In response to sufficiently positive intracellular voltages, gating charges within the VSD translate from an intracellular resting position to a more extracellular activated conformation (Armstrong & Bezanilla, 1974; Tao et al., 2010; Xu et al., 2019). This gating charge movement powers the conformational changes of voltage sensor activation, which are coupled to subsequent pore opening and potassium conduction (Zagotta et al., 1994; Islas & Sigworth, 1999). The progression of the α channel protein through the entire landscape of conformations leading to opening, define a pathway for the activation of the K^+ conductance.

Kv2 currents are present in most, if not all, central neurons. Genetic deletion of Kv2.1 leads to seizure susceptibility and behavioral hyperexcitability in mice (Speca et al., 2014), and human Kv2.1 mutations result in developmental epileptic encephalopathy (Bar et al., 2020; Kang et al., 2019; Niday & Tzingounis, 2018; Thiffault et al., 2015; Torkamani et al., 2014), underscoring the importance of these channels to brain function. The unique kinetics and voltage dependence of Kv2 currents are critical to neuronal activity, as they regulate action potential duration and can either support or limit repetitive firing (Du et al., 2000; Hönigsperger et al., 2017; Kimm et al., 2015; Liu & Bean, 2014; Malin & Nerbonne, 2002; Mohapatra et al., 2009; Palacio et al., 2017; Romer et al., 2019). Kv2.1 conduction is regulated by multiple mechanisms that homeostatically maintain neuronal excitability (Cerda & Trimmer, 2011; Misonou et al., 2006; Romer et al., 2019; Speca et al., 2014). Kv2.1 regulation by ischemia (Aras et al., 2009; Misonou et al., 2004, 2005, 2008), glutamate (Baver & O'Connell, 2012; Mulholland et al., 2008), N-methyl-D-aspartic acid (Mulholland et al., 2008), phosphorylation and sumoylation (Ikematsu et al., 2011; Murakoshi et al., 1997; Park et al., 2006; Plant et al., 2011) and auxiliary protein subunits (Maverick et al., 2021; Peltola et al., 2011) all change the dynamics of Kv2.1 channel activation to shift the midpoint of the conductance–voltage relation (*G–V*) to more positive or negative voltages. However, it is not known which steps in the conductance activation pathway are modulated by any of these forms of regulation.

To identify activation steps that are targeted to modulate Kv2.1 conductance, we investigated modulation by the extracellular adhesion protein AMIGO1. AMIGO1 (AMphoterin–Induced Gene and Open reading frame) is a single-pass transmembrane protein with an extracellular immunoglobulin domain and six leucine-rich repeats (Kuja-Panula et al., 2003) and is an auxiliary subunit of Kv2 channels (Peltola et al., 2011). AMIGO1 exhibits widespread subcellular colocalization with Kv2 in neurons throughout the brain and in multiple mammalian species (Bishop et al., 2018; Peltola et al., 2011, 2015). In vertebrate brain neurons, AMIGO1 is important for cell adhesion (Kajander et al., 2011; Kuja-Panula et al., 2003), neuronal tract development (Zhao et al., 2014), and circuit formation (Chen et al., 2012; Peltola et al., 2015; Zhao et al., 2014). AMIGO1 has been proposed to play a role in schizophrenia biology (Peltola et al., 2015). A robust association between AMIGO1 and Kv2.1 is evident by their coimmunoprecipitation from mouse and zebrafish brain samples (Peltola et al., 2011; Zhao et al., 2014) and their co-diffusion through neuronal membranes in response to stimuli that

reorganize Kv2.1 (Peltola et al., 2011). This robust association suggested that AMIGO1 modulation of Kv2.1 would be sufficiently stable for biophysical study of its mechanism.

In other voltage-gated ion channels, the step(s) in the conductance activation pathway that are targeted by modulators have been identified. The *G–V* relation can be shifted to more negative voltages by modulating pore opening (Dudem et al., 2020; Horrigan & Aldrich, 2002; Rockman et al., 2020), voltage sensor movement (Barro-Soria et al., 2015), or voltage sensor-pore coupling (Barro-Soria et al., 2017; Nakajo & Kubo, 2015; Yan & Aldrich, 2010). Single-pass transmembrane auxiliary subunits modulate other voltage-gated ion channel α subunits by a variety of mechanisms (Barro-Soria et al., 2014, 2017; Brackenbury & Isom, 2011; Dudem et al., 2020; Zhang & Yan, 2014). However, AMIGO1 only shares a limited degree of secondary sequence with other single-pass transmembrane auxiliary subunits (Chen et al., 2006), and divergent structural interactions have been observed among other single-pass transmembrane auxiliary subunits (Shen et al., 2019; Sun & MacKinnon, 2020). As there is no consensus binding pose or mechanism of interaction for auxiliary subunits, it is difficult to predict which step in the conductance activation pathway AMIGO1 acts on. A recent study proposed that AMIGO proteins shift Kv2.1 conductance by increasing voltage sensor-pore coupling, and that measurements of voltage sensor movement could test this hypothesis (Maverick et al., 2021).

Here we ask whether AMIGO1 alters conformational changes associated with pore opening or with voltage sensor movement. To interrogate the mechanism through which AMIGO1 modulates the Kv2.1 conductance activation pathway, we use a combination of electrophysiological and imaging approaches. We find that AMIGO1 affects conductance activation to a different degree when Kv2.1 gating is modified. We find no changes in single channel conductance. We find that AMIGO1 modulates voltage sensor movements, yet find no evidence that the large extracellular domain of AMIGO1 perturbs the electrostatic environment of the voltage sensor. We conclude that AMIGO1 destabilizes the earliest resting conformation in the pathway of channel activation.

Methods

Reagents

A conjugate of a cysteine–modified guangxitoxin–1E and the maleimide of fluorophore Alexa594 (GxTX Ser13Cys(Alexa594)) was used to selectively modulate Kv2.1 channel gating and to fluorescently identify surface-expressing Kv2.1 channels (Thapa et al., 2021). Conjugates of propargylglycine (Pra)–modified GxTX and the fluorophore JP–N_3 (GxTX Ser13Pra(JP) and GxTX Lys27Pra(JP)) were used to monitor the chemical environment surrounding GxTX when localized to the channel (Fletcher-Taylor et al., 2020). All modified GxTX–mutants were synthesized by solid phase peptide synthesis as described (Fletcher-Taylor et al., 2020; Tilley et al., 2014).

Cell culture

Maintenance

The HEK293 cell line subclone TS201A (Eaholtz et al., 1994) was obtained from Cell Genesis and maintained in DMEM (Gibco Cat# 11995-065) with 10% Fetal Bovine Serum (HyClone Cat# SH30071.03HI, LotAXM55317) and 1% penicillin/streptomycin (Gibco, 15-140-122) in a humidified incubator at 37°C under 5% CO_2. Channel expression was achieved by transient transfection.

The two different Tetracycline-Regulated Expression (T-REx™) Chinese Hamster Ovary (CHO) cell lines, both stably expressing the Tet repressor (pcDNA™6/TR plasmid) were cultured as described previously (Tilley et al., 2014). One "CHO cell" subclone (Invitrogen, Cat# R71807) only expressed pcDNA™6/TR and was used in experiments with pCAG-ChroME-mRuby2-ST transfection. The other "Kv2.1–CHO cell" subclone (Trapani & Korn, 2003) expressed pcDNA™6/TR and pCDNA™4/TO encoding the rat Kv2.1 (rKv2.1) channel. Within these Kv2.1-CHO cells, a dose of 1 μg/ml minocycline (Enzo Life Sciences), prepared in 70% ethanol, was added to the cellular media for indicated durations to induce rKv2.1 channel expression. (While minocycline is needed for appreciable Kv2.1 expression, there may be some residual Kv2.1 expression due to leakiness within the tet–repressor system (Trapani & Korn, 2003).) The Kv2.1-CHO cell line was negative for mycoplasma contamination by biochemical tests (LT07; MycoAlert; Lonza).

CHO cells were chosen as an expression system due to their lack of substantial endogenous K^+ currents (Gamper et al., 2005). The incorporation of the inducible expression system promotes less cell-to-cell variation in current density than transient transfection (Supplemental Fig. 2A, B vs. D, E, F, G), helps minimize issues associated with Kv2.1 current density being too high or too low, and can be tuned to achieve appropriate expression for different experiments. We choose to limit induction to 1.5 hours to minimize series resistance-induced voltage errors apparent in ionic K^+ current recordings (Fig. 4, 6, 10) and increased induction to 48 hours to produce sufficient Kv2.1 density necessary for recording gating currents (Fig. 7).

Transfection

5 minutes prior to transfection, cells were plated at 40% confluency in culture media free of antibiotics, selection agents, and serum and allowed to settle at room temperature. For imaging studies (except dose–response), cells were plated in 35 mm No. 1.5 glass–bottom dishes

(MatTek, P35G-1.5-20-C). For dose response time–lapse imaging, cells were plated onto 22 x 22 mm No. 1.5H coverglass (Deckglaser). For electrophysiological studies, cells were plated in 35 mm tissue culture treated polystyrene dishes (Fisher Scientific, 12-556-000). Transfections were achieved with Lipofectamine 2000 (Life Technologies, 11668-027). Each transfection included 220 μL Opti–MEM (Life Technologies, 31985062), 1.1 μL Lipofectamine, and the following amount of plasmid DNA. HEK293 cell experiments: 0.1 μg of mKv2.1 DNA and either 0.1 μg of pEGFP, mAMIGO1–pIRES2–GFP DNA, or hSCN1β–pIRES2–GFP. The pIRES2–GFP vector has an encoded internal ribosome entry site which promotes continuous translation of two genes from a singular mRNA (Liu et al., 2000) so that GFP fluorescence indicates the presence of AMIGO1 or SCN1β mRNA. Kv2.1–CHO cell experiments: 1 μg of either mAMIGO1–pEYFP–N1 or pEGFP. CHO cells experiments: 1 μg of both pCAG–ChroME–mRuby2-ST and mAMIGO1-pEYFP-N1. Cells were incubated in the transfection cocktail and 2 mL of unsupplemented, basal media for 6-8 hours before being returned to regular growth media. Cells were given 40-48 hours recovery following transfection before being used for experiments.

pEGFP, mAMIGO1–pEYFP–N1, and pCAG–ChroME-mRuby2-ST (Mardinly et al., 2018) plasmids were all kind gifts from James Trimmer, University of California, Davis. mAMIGO1–pEYFP–N1 uses a VPRARDPPVAT linker to tag the internal C–terminus of wild–type mouse AMIGO1 (NM_001004293.2 or NM_146137.3) with eYFP. pCAG–ChroME–mRuby2–ST is a vector encoding a soma–targeted and mRuby2–tagged opsin protein engineered by (Mardinly et al., 2018) using the Kv2.1–derived soma–targeting and ER–PM junction–remodeling amino acid sequence (Kirmiz et al., 2018a; Lim et al., 2000). mKv2.1 (NM_008420) was purchased from OriGene (MG210968). hSCN1β–pIRES2–GFP was a kind gift of Dr. Vladimir Yarov–Yarovoy (University of California, Davis). mAMIGO1–pIRES2–GFP was subcloned from hSCN1β–pIRES2–GFP by Mutagenex. NheI and BamHI restriction sites were used to subclone mAMIGO1 into the place of hSCN1β.

Electrophysiology

Voltage clamp was achieved with an Axopatch 200B patch clamp amplifier (Axon Instruments) run by Patchmaster software (HEKA).

Whole-cell macroscopic ionic current measurements

Recording solutions were prepared as follows:

Cell type	External Solution (in mM)	Internal Solution (in mM)
HEK293 cells LJP: 3.9 mV E_K: -89.0 mV	5 KCl, 160 NaCl, 10 HEPES, 2 $CaCl_2$, 2 $MgCl_2$, 10 glucose adjusted to pH 7.32 with NaOH. Osmolality: 345 mOsm	160 KCl, 5 EGTA, 10 HEPES, 1 $CaCl_2$, 2 $MgCl_2$, and 10 glucose, adjusted to pH 7.31 with KOH. Osmolality: 344 mOsm
Kv2.1–CHO cells LJP: 8.5 mV E_K: - 97.4 mV	3.5 KCl, 155 NaCl, 10 HEPES, 1.5 $CaCl_2$, 1 $MgCl_2$, adjusted to pH 7.4 with NaOH. Osmolality: 315 mOsm	70 KCl, 5 EGTA, 50 HEPES, 50 KF, and 35 KOH, adjusted to pH 7.4 with KOH. Osmolality: 310 mOsm*
Kv2.1–CHO cells With Mg^{2+} LJP: 13.1 mV E_K: -97.4 mV	3.5 KCl, 6.5 NaCl, 10 HEPES, 1.5 $CaCl_2$, 100 $MgCl_2$, adjusted to pH 7.41 with NaOH. Osmolality: 289 mOsm	70 KCl, 5 EGTA, 50 HEPES, 50 KF, and 35 KOH, adjusted to pH 7.4 with KOH. Osmolality: 298 mOsm*

Osmolality was measured by a VAPRO vapor pressure osmometer 5520. For each experiment/cell type, internal and external solutions were measured side-by-side on the same day. LJP values were tabulated using Igor's patchers power tools extension version 2.15 (Dr. Francisco Mendez and Frank Wurriehausen, Max-Planck-Institut fur biophysikalische chemie). LJP values were corrected for *post hoc*, offline. *The external solutions for Kv2.1CHO cells and for Kv2.1CHO cells with Mg^{2+} were prepared in two separate batches; osmolality measurements less than 10% of the theoretical (expected) value were tolerated for use.

Kv2.1 channel expression was achieved through transient transfection in HEK293 cells (see "*transfection*") and through 1-1.5 hours of incubation with minocycline administered in culture immediately prior to patching for Kv2.1–CHO cells. Prior to patch–clamp current recordings, Kv2.1–CHO cells were harvested by scraping in Versene (Gibco, 15040066) or TrypLE (Gibco, 12563011). HEK293 cells were dislodged by scraping. Dissociated cells were transferred to a polypropylene tube, washed three times by pelleting at 1,000 x *g* for 2 minutes and then resuspend in in the same external solution as used in the recording chamber bath. Cells were rotated in a polypropylene tube at room temperature (22-24 °C) until use. Cells were then pipetted into a 50 μL recording chamber (Warner Instruments, RC-24N) prefilled with external solution and allowed to settle for 5 or more minutes. For HEK293 experiments, the external solution was supplemented with TTX at 5 μM to block endogenous sodium channels which are sporadically expressed in HEK293 cells. After adhering to the bottom of the glass recording chamber, cells were thoroughly rinsed with external solution using a gravity–driven perfusion system. Cells showing plasma membrane-associated YFP expression or intracellular GFP expression of intermediate intensity were selected for patching.

Borosilicate glass recording pipettes (BF150-110-7.5HP, Sutter) were pulled with blunt tips, coated with silicone elastomer (Sylgard 184, Dow Corning), heat cured, and tip fire-polished to resistances less than 4 MΩ. Series resistances of 3–9 MΩ (before compensation) were estimated from the value arrived at during whole-cell capacitive transient subtraction by manual adjustment of the whole-cell parameters circuit of the amplifier. Series-resistance compensation lag was set to 10 μs. Series resistance compensation (of < 90%) was used as needed to constrain voltage error to less than 10 mV. Cell capacitances were 4–15 pF, resulting in cell membrane charging time constants of <50 μs before compensation. The series resistance compensation prediction (super-charging) circuit was not used. Remaining capacitance and Ohmic leak were subtracted using a P/5 protocol. Recordings were low–pass filtered at 10 kHz using the amplifier's built-in Bessel and digitized at 100 kHz.

Whole–cell macroscopic ionic current voltage protocols HEK293 cells

Conductance–voltage (*G–V*) profiles for HEK293 cells were derived from cells held at -80 mV and depolarized by steps ranging from -80 mV to +85 mV in increments of +5 mV (100 ms) before being returned to 0 mV (100 ms) to record tail currents. The intersweep interval was 2 s. The average current in the 100 ms prior to the voltage step was used to zero-subtract the recording. Mean outward current was quantitated as the mean amplitude between 90-100 ms post depolarization. Cells with less than 65 pA/pF of outward current at +85 mV were excluded because they lacked a 3–fold increase in the amount of cell size–normalized outward current compared to what could be expected from endogenous K^+ channels in HEK293 cells (Yu & Kerchner, 1998). Mean tail current was derived from the average amplitude between 0.2-1.2 ms into the 0 mV step.

Whole–cell macroscopic ionic current voltage protocols in Kv2.1–CHO cells

G–V profiles for Kv2.1–CHO cells were derived from cells held at -100 mV and depolarized by steps ranging from -80 mV to +120 mV in increments of +5 mV (100 ms) before being returned to 0 mV (100 ms). The intersweep interval was 2 s. The average current in the 100 ms prior to voltage step was used to zero–subtract the recording. Mean outward current was taken as the mean value between 190-200 ms. Mean tail current values were derived from the average current value between 200.2-201.2 ms.

Whole–cell macroscopic ionic current voltage protocols in Kv2.1–CHO cells with GxTX–594

Cells that maintained a membrane resistance greater than 1 GΩ (when held near the holding potential) after a first round of ionic current voltage protocols, were selected to be treated with GxTX–594. 5 minutes after the addition of 100 μL of 100 nM GxTX-594, the voltage–step protocol was run once more. GxTX–594 was diluted from a 13.1 μM stock (stored at -80 °C, thawed on ice) to its working concentration in the 3.5 mM K^+ patching solution. GxTX–594 was added manually while holding at -100 mV; during initial additions, the membrane potential was pulsed to 0 mV to gauge the time course of binding. To promote fluid exchange during the addition and to maintain constant bath fluid level, fluid from the chamber was removed distally through vacuum tubing.

Whole-cell macroscopic ionic current *G–V* analysis

Both HEK293 and Kv2.1–CHO voltage clamp data was adjusted for series–resistance induced voltage error and normalized in Microsoft Excel. Any datum from voltage steps that produced a series–resistance induced voltage error greater than 10 mV was excluded from analysis. Voltage error (V_{error}) was tabulated by the product of current amplitude taken from the zero–subtracted, mean outward current ($I_{avg,step}$), and estimated series resistance remaining after compensation ($R_{s,uncompensated}$) (Eqn. A).

$$V_{error} = I_{avg,step} * R_{s,uncompensated} \quad \text{(Eqn. A)}$$

Tail currents were normalized by the mean tail current elicited from 50-80 mV plotted against the estimated membrane potential ($V_{membrane}$), which accounted for both voltage–error and the calculated liquid junction potential (*LJP*) (Eqn. B),

$$V_{membrane} = V_{command} - V_{error} - LJP \quad \text{(Eqn. B)}$$

G–V relations were individually fit with a 4th power Boltzmann (Eqn. C) in order to represent the four independent and identical voltage sensors that must all activate for channels to open. Fitting was carried out using Igor Pro software, version 7 or 8 (Wavemetrics, Lake Oswego, OR) that employs nonlinear least squares curve fitting via the Levenberg-Marquardt algorithm.

$$\left(1 + e^{\frac{-(V-V_{i,1/2})z_i F}{RT}}\right)^x \quad \text{(Eqn. C)}$$

Within a 4th power Boltzmann *G* is conductance, *A* is maximum amplitude, $V_{i,1/2}$ is the activation midpoint for each of four independent transitions in units of millivolts, z_i is the minimum effective gating valence associated with channel activation in units of elementary charge e_0 as determined by ionic currents, *F* is the Faraday constant, *R* is the ideal gas constant, *T* is absolute temperature, and *x* represents the number of independent identical transitions required to open a

channel. To calculate the $V_{i,Mid}$ values corresponding to 4^{th} power Boltzmann fits, the $V_{i,1/2}$ and z_i fit values were input into (Eqn. D).

$$V_{i,Mid} = V_{i,1/2} + \frac{42.38}{z_i} \quad \text{(Eqn. D)}$$

For clarity of presentation, "average" G_K plots represent reconstructed Boltzmann curves that were formulated using the average $V_{i,1/2}$ and average z_i values obtained from the grouped individual fits. The shaded regions surrounding the reconstructed curve represent Boltzmann curves reconstructed using the average z_i and either $V_{i,1/2}$ + SD or $V_{i,1/2}$ - SD.

Whole-cell macroscopic ionic current free energy and K_{eq} calculations

To estimate of the Gibbs free energy (ΔG_{AMIGO1}) that AMIGO1 must impart onto Kv2.1 in order to produce the observed shift in the G–V, we used (Eqn. E).

$$\Delta G = -R \times T \times \ln(K_{eq}) \quad \text{(Eqn. E)}$$

Here R = 0.00199 kcal/(K*mol) and T = 298K. K_{eq}, or the equilibrium constant of channel opening, was approximated by $\frac{f_{Kv2.1+AMIGO1}(V_{i,Mid,Kv2.1})}{1-f_{Kv2.1+AMIGO1}(V_{i,Mid,Kv2.1})}$. Here $f_{Kv2.1+AMIGO1}(V_{i,Mid,Kv2.1})$ is the average conductance of Kv2.1 + AMIGO1 cells elicited at the voltage equivalent to $V_{i,Mid,Kv2.1}$, or the $V_{i,Mid}$ of Kv2.1 control cells (Table 1). $f_{Kv2.1+AMIGO1}(V_{i,Mid,Kv2.1})$ values were calculated by interpolation using the "reconstructed", normalized Boltzmann plots in Fig. 1F, 4F, 6F, or 10F. Fold K_{eq} values were calculated as the ratio of $K_{eq,Kv2.1+AMIGO1}$ to $K_{eq,Kv2.1}$. Measures of conductance such as those in Figs. 1, 4, 6, and 10 only approximate the fraction of channels open out of the total amount of channels available to open and are incapable of assessing the fraction of channels that exist while remaining electrically silent. A true measure of K_{eq} is the quotient describing the fraction of channels open to the fraction of channels closed. We acknowledge that this G–V-based measure is an underestimate and not an exact approximation for K_{eq}. As such, we expect our ΔG to be an overestimate.

Whole-cell macroscopic ionic current kinetic analysis

Activation time constants (τ_{act}) and sigmoidicity values (σ) (Sack & Aldrich, 2006) were derived from the current response to the same voltage protocol used to derive G–V relations. Currents were normalized from 0-100% with the average current elicited in the 100 ms prior to the voltage step as 0% and the average current from 190-200 ms as 100%. τ_{act} and σ were derived by fitting the 10-90% current rise with a power with delay function (Eqn. F):

$$I_K = A\left(1 - e^{\frac{-t}{\tau_{act}}}\right)^{\sigma} \quad \text{(Eqn. F)}$$

Eqn. F yields a curve that originates at I_K = 0 and asymptotically approaches its maximum current amplitude, A, with a time course determined by time constant τ_{act}, and sigmoidicity σ, which is unitless. The $t = 0$ mark was adjusted to 100 μs after voltage step start to correct for filter delay and cell charging. For representation, average τ_{act} and σ values are plotted against command voltage potentials. In summary plots, dots represent averages, while shaded regions bounded by bars represent the standard error of the mean. τ_{act} and σ values from individual fits were statistically evaluated at each command voltage in Igor Pro software using an unpaired, two-tailed, Student's T-test. Kv2.1 deactivation kinetics can become progressively slower after establishment of whole cell mode, similar to Shaker deactivation after patch excision (Schoppa

& Sigworth, 1998). Due to the ambiguity expected from this increased variability of deactivation kinetics, deactivation kinetics were not analyzed.

On-cell microscopic single channel current measurements

Recording solutions were prepared as follows:

Cell type	External Solution (in mM)	Internal Solution (in mM)
Kv2.1-CHO cells LJP: -3.3 mV	135 KCl, 50 HEPES, 20 KOH, 20 NaOH, 2 $CaCl_2$, 2 $MgCl_2$, and 0.1 EDTA, adjusted to pH 7.27 with HCl. Osmolality: 346 mOsm	155 NaCl, 50 HEPES, 20 KOH, 2 $CaCl_2$, 2 $MgCl_2$, 0.1 EDTA, and adjusted to pH 7.29 with HCl. Osmolality: 347 mOsm

Osmolality was measured by a VAPRO vapor pressure osmometer 5520. For each experiment/cell type, internal and external solutions were measured side-by-side on the same day. LJP values were tabulated using Igor's patchers power tools extension version 2.15 (Dr. Francisco Mendez and Frank Wurriehausen, Max-Planck-Institut fur biophysikalische chemie). LJP values were corrected for *post hoc*, offline.

Kv2.1 channel expression was achieved through 1-1.5 hours of incubation with minocycline administered in culture immediately prior to patching for Kv2.1–CHO cells. Prior to on–cell current recordings in a 50 μL recording chamber (Warner Instruments, RC-24N), Kv2.1–CHO cells were harvested, washed, resuspended, and stored by the same protocols detailed in "*Whole–cell macroscopic ionic current measurements.*" While YFP fluorescence enabled us to detect the presence of plasma membrane-associated AMIGO1 protein, a caveat of this experiment is that we are not able to definitely state whether recordings from a single Kv2.1 channel also included AMIGO1.

Sylgard-coated and fire–polished, thick-walled borosilicate glass (BF150-86-7.5HP; Sutter Instruments) were pulled to resistances were >10 MΩ. Single channel recordings were made from on-cell patches, to avoid Kv2.1 current rundown that occurs after patch excision (Lopatin et al., 1994). Pipette capacitance compensation was used to adjust for pipette charging, but series resistance compensation was not used. Recordings were low–pass filtered at 10 kHz using the amplifier's built-in Bessel and digitized at 100 kHz.

On–cell microscopic current voltage protocols in Kv2.1–CHO cells

Cells were held at -100 mV and depolarized by steps to +0 mV (1000 ms) before being returned to the holding potential of -100 mV. The intersweep interval was 2 s. The average current in the 100 ms prior to voltage step was used to normalize the baseline the recording and correct for any drift. To isolate single channel currents from leak current and uncompensated capacitive transients, multiple traces without openings were averaged and then subtracted from each trace with single-channel openings.

On-cell microscopic single channel current analysis

Single channel amplitude histograms were obtained from corrected traces at +0 mV that were clearly bimodal, and each peak was fitted (to its half maximum) with a Gaussian function. The single channel current amplitude was defined as the difference between the peaks of the fits (see Fig. 5C, D), and a half-amplitude threshold at the midpoint between them. Occurrences of K^+-sensitive sub–conductance levels were minimized to less than < 10% compared to fully open conductance levels by the 20 mM K^+ extracellular solution in the pipette (Trapani et al., 2006). The sub–conductance levels were not treated explicitly during analysis, as justified in (Tilley et al., 2019). All traces reported were idealized to include only a single fully open conductance level. Idealization of traces resulted in channel event artifacts occurring when variant sub–

conductance currents crossed the half–amplitude threshold or when capacitive artifacts were not entirely subtracted. This resulted in overrepresentation of fast, flickery openings and closings, especially at the initiation of the voltage pulse. Hence, no conclusions were made concerning the kinetics of fast, flickery states nor the latency to first open. Conclusions were drawn only from states with longer–lived dwell time constants.

Open probability was calculated as the fraction of the integral of the amplitude histogram above the half–amplitude threshold. The half–amplitude threshold of idealized traces was also used to determine the open and closed dwell times. The distributions of dwell times were analyzed, fitted, and displayed by quantifying the square–root of the number of events in logarithmic bins (Sigworth & Sine, 1987). Open dwell times were well described by a single exponential component which was used to derived $\tau_{closing}$. Average open dwell times were also described as the geometric mean of all open dwell times. Closed dwell times appeared to have multiple exponential components and were not fit. Average closed dwell times were solely described as the geometric mean of all closed dwell times.

Whole–cell gating current measurements

Recording solutions were prepared as follows:

Cell type	External Solution (in mM)	Internal Solution (in mM)
Kv2.1-CHO cells LJP: -3.3 mV	150 TEA-Cl, 41 HEPES, 1 $MgCl_2 \cdot 6$ H_2O, 1.5 $CaCl_2$, adjusted to pH to 7.32 with NMDG. Osmolality: 311 mOsm	90 NMDG, 1 NMDG-Cl, 50 HEPES, 5 EGTA, 50 NMDG-F, 0.01 CsCl, and adjusted to pH 7.36 with methanesulfonic acid Osmolality: 303 mOsm

To avoid KCl contamination of the recording solution from the pH electrode, pH was determined in small aliquots that were discarded. Osmolality was measured by a VAPRO vapor pressure osmometer 5520. For each experiment/cell type, internal and external solutions were measured side-by-side on the same day. LJP values were tabulated using Igor's patchers power tools extension version 2.15 (Dr. Francisco Mendez and Frank Wurriehausen, Max-Planck-Institut fur biophysikalische chemie). LJP values were corrected for *post hoc*, offline.

Kv2.1 expression was achieved by 48 hours incubation with minocycline during culture. Prior to whole–cell gating current recordings in a 50 μL recording chamber (Warner Instruments, RC-24N), Kv2.1–CHO cells were harvested, washed, resuspended, and stored by the same protocols detailed in "*Whole–cell ionic current measurements.*" To avoid contamination of the recording chamber with Kv2.1-permeant ions, cells were given > 4 min to adhere before gently washing with 10 mL of the gating current recording solution.

Recording pipettes were pulled from thin-walled borosilicate glass (BF150-110-7.5HP; Sutter Instruments) to resistances measured within gating current solutions of 6-14 MΩ. Patched cells had series resistance of 14-30 MΩ (before compensation), as estimated by the value arrived at during whole–cell capacitive transient subtraction by manual adjustment of the whole–cell parameters circuit of the amplifier. Series-resistance compensation lag was set to 10 μs. The series resistance compensation correction circuit was set to 50% when the estimated series resistance exceeded 10 MΩ. Cell capacitances were 6-10 pF, resulting in cell membrane charging time constants of <50 μs before compensation. The series resistance compensation prediction (super-charging) circuit was not used. Remaining capacitance and Ohmic leak were subtracted offline using the average of five traces recorded during P/5.9 voltage protocols executed from a -133 mV holding potential. Low-pass filtering at 10 kHz and digitization at 10 kHz were used during recordings.

Whole–cell gating current voltage protocols in Kv2.1–CHO cells

Gating charge–Voltage (*Q–V*) profiles for CHO cells were derived from patched cells held at -100 mV and step depolarized from -100 mV to +120 mV in increments of +5 mV (100 ms, to record ON gating currents) before being returned to -140 mV (100 ms, to record OFF gating currents). The intersweep interval was 2 s. Recordings were low–pass filtered at 10 kHz using the amplifier's built-in Bessel and digitized at 100 kHz. For representation, exemplar gating current traces were filtered at 2000 Hz.

Whole-cell gating current *Q-V* analysis

An early component ON gating charge movement was quantified by integrating ON gating currents in a 3.5 ms window ($Q_{ON,fast}$) following the end of any obvious fast capacitive artifacts created from the test voltage step. The tail of the ON charge movement is so slow that it is difficult to integrate in these cells, making the cutoff point for integration arbitrary. This 3.5 ms integration window resulted in a more positive $Q_{ON,fast}$–*V* midpoint than with a 10 ms window reported previously (Tilley et al., 2019), and more positive midpoint than the *G–V* relation. Differences in gating current solutions compared to prior studies may also contribute to the different midpoints reported (Jara-Oseguera et al., 2011; Scholle et al., 2004; Tilley et al., 2019). Currents were baseline-subtracted with the average current elicited during a 1 ms-long period after current decay has ceased. This window began 4 ms following the test voltage step stimuli.

Q_{OFF} gating charge movement was quantified by integrating the area under the gating currents in a 10.5 ms window following the end of any obvious fast capacitive artifacts created from the voltage step to -140 mV. Currents were baseline-subtracted with the average current elicited during a 10 ms-long period after current decay has ceased. This window began 10 ms following the initiation of the -120 mV voltage step stimuli. To determine the amount of gating charge per cell, $Q_{ON,fast}$ was normalized by cell–capacitance size (*fC/pF*). Since the level of series–resistance induced voltage error was negligible (< 1 mV), Kv2.1–CHO estimated membrane potential was only adjusted for LJP. *Q–V* curves were normalized to the average *Q* value elicited from 100-120 mV steps. Adjustments and normalizations were made in Microsoft Excel.

Q–V relations were individually fit with a 1st power Boltzmann (Eqn C.), as described previously, where $V_{g,Mid}$ is the voltage where the function reaches half maximal conductance, and z_g is valence in units of elementary charge (e_0) associated with gating machinery rearrangements. For clarity of presentation, the average max-normalized $Q_{ON,fast}$ and Q_{OFF} plots were "reconstructed" using the average and standard deviation from individual fits, as previously described in the methods "*Whole-cell ionic current G-V analysis"*. Our $V_{g,Mid,ON,fast}$ value is distinct from values we have reported previously (Tilley et al., 2019), potentially due to differences in recording solutions which can affect voltage sensor movement (Consiglio & Korn, 2004).

Whole–cell gating current kinetic analysis

Time constants (τ_{ON}) were derived from the $I_{g,ON}$ response to the same voltage protocol used to derive *Q–V* relations. Baseline-subtracted currents were fit with a double-exponential function (Eqn. G),

$$I_{g,ON} = A\left(e^{\frac{-t}{\tau_{ON}}}\right) + B - A_{rise}\left(e^{\frac{-t}{\tau_{rise}}}\right) \qquad \text{(Eqn. G)}$$

where current decays from maximum amplitude (A) to baseline (B) with a time constant of τ_{ON}. The rising phase of $I_{g,ON}$ was accounted for by A_{rise} and τ_{rise}. The rising phase was predicted to be affected by the rate of cell charging and was not used in analyses. The rising phase of $I_{g,OFF}$ was not well fit by Eqn. G and thus τ_{OFF} was not analyzed.

The voltage-dependence of the forward activation rate was determined by fitting the average τ_{ON}–V with an exponential function (Eqn. H) on a semi-logarithmic plot. Fitting was weighted by the standard error associated with the average.

$$\tau_{ON} = \frac{1}{\tau_{0mV,\alpha} e^{Vz_\alpha F/RT} + \tau_{0mV,\beta} e^{Vz_\beta F/RT}} \quad \text{(Eqn. H)}$$

Eqn. H yields a curve where the rate of gating charge activation, τ_{ON}, is predicted by the forward ($\tau_{0mV,\alpha}$) and reverse ($\tau_{0mV,\beta}$) rates of activation at the neutral voltage of 0 mV and a voltage dependence in units of elementary charge, z. All other values have the same meaning as stated in Eqn. C. To constrain fits encompassing the entire τ_{ON}-V plot, the forward activation rate and charge dependence were first determined by fitting Eqn. H (with $\tau_{0mV,\beta} = 0$, $z_\beta = 0$) to the portion of τ_{ON}–V that was linear and steep. Since $I_{g,ON}$ was not always well approximated by Eqn. G at low voltages where reverse rates are suspected to be large, fit values from Eqn. H for reverse rates were not analyzed.

Whole–cell gating current kinetic analysis free energy calculations

The estimate of the minimum Gibbs free energy of activation ($\Delta G^{\ddagger}$) required to produce the observed change in the forward rate of gating current activation, $\tau_{0mV\alpha}$, was determined using (Eqn. I). R and T have been previously described.

$$\Delta G^{\ddagger} = -4 \times R \times T \times \ln\left(\frac{\tau_{0mV,a_{AMIGO1}}}{\tau_{0mV,a_{Control}}}\right) \quad \text{(Eqn. I)}$$

Whole–cell gating current free energy calculations (Eqn. E, Eqn. J*, and Eqn. J*°)

The estimate of the Gibbs free energy (ΔG_{AMIGO1}) required for AMIGO1 to impart onto Kv2.1 in order to produce the shift in the gating charge–voltage response was determined using (Eqn. E), as previously described in the methods of macroscopic free energy calculations. $\frac{f_{Kv2.1+AMIGO1}(V_{g,Mid,Kv2.1})}{1-(f_{Kv2.1+AMIGO1}(V_{g,Mid,Kv2.1}))}$ was derived using the "reconstructed" Q–V relations in Fig. 7I and 7T. Again, $V_{g,Mid,Kv2.1}$ represents $V_{g,Mid}$ of Kv2.1 control cells (Table 2). While we expect ΔG_{AMIGO1} approximates made from conductance measurements and Q_{ON} recordings to be overestimates, we expect $\frac{f_{Kv2.1+AMIGO1}(V_{g,Mid,Kv2.1})}{1-(f_{Kv2.1+AMIGO1}(V_{g,Mid,Kv2.1}))}$ to closely approximate a K_{eq} of channel activation since Q_{OFF} captures all gating current movement. ΔG_{AMIGO1} was also calculated using Eqn. J, which utilizes inputs derived from the 1st order Boltzmann fit to calculate a minimum energetic input for AMIGO1.

$$\Delta G = V_{1/2} \times Q \times F \quad \text{(Eqn. J)}$$

All variables have been previously described. F = 23.06 kcal/volt gram equivalent. $V_{1/2}$ was defined as either $V_{g,Med}$ (denoted by "°", see below for methods of calculation) or $V_{g,Mid}$. Since this method assumes that Kv2.1 channels progress from their resting state to an activated state by moving gating charges on 4 independent voltage sensors, Q was defined as the theoretical value associated with ion channel activation, 12.5 e_0 (denoted by "*"). 12.5 e_0 represents the charge

associated with channel activation as determined from a limiting slope analysis of the Kv2.1 open probability-voltage relation (Islas & Sigworth, 1999).

Whole–cell gating current median voltage analysis (°)

Implicit in our calculations of z_g (and z_i) is the assumption that voltage sensors adopt only two conformations, resting and activated, yet many more conformations are involved in Kv channel activation (Bezanilla et al., 1994; Zagotta et al., 1994). As a model-independent method to estimate the minimum ΔG_{AMIGO1}, we employed a median voltage analysis (Chowdhury & Chanda, 2012) which makes no assumptions about the conformations underlying the gating process. Briefly, the median voltage ($V_{g,Med}$) describes the voltage at which half of the gating charge is fully activated, while half of the charge is still in the resting conformation. Mathematically this state can be described as the voltage that bisects the max-normalized Q–V relation into two portions: a portion to the left of the bisecting line, where the area under the normalized Q–V relation is equivalent to amount of charge that has activated fully, and a portion to the right of the bisecting line, where the area above the normalized Q–V relation is equivalent to the amount of charge that has yet to activate.

We used the average curves describing all Kv2.1 control or Kv2.1 + AMIGO1 normalized Q_{OFF}–V relations to define $V_{g,Med}$. Integration above and below the curve was carried out using a trapezoidal rule. For calculating areas above the curve integration values were adjusted to reflect a transposition of axis upon curve inversion. The AMIGO1–induced change in median voltage ($\Delta V_{g,Med}$) from the Q_{OFF}–V relation was -9.5 mV.

All of the aforementioned methods for calculating the ΔG approximate the minimum total change movement associated with conformation change (Zagotta et al., 1994), and thus these energy calculations also represent a minimum estimate of AMIGO1's impact.

Imaging

Fluorescence imaging instrumentation

Images were obtained with an inverted confocal system (Zeiss LSM 880, 410900-247-075) run by ZEN black v2.1. Images were acquired with a Plan-Apochromat 1.4 NA 63x DIC M27 oil immersion objective (Zeiss 420782-9900-799), an EC Plan-Neofluar 1.30 NA 40x apochromatic oil immersion objective (Zeiss 420462-9900-000), or a LD C-Apochromat 1.15 NA 63x M27 water immersion objective (Zeiss 421887-9970-000). Images were taken in either confocal imaging mode, lambda scan mode or in Airyscan superresolution imaging mode.

In confocal and lambda scan imaging mode fluorescence was collected with the microscope's 32–detector gallium arsenide phosphide photomultiplier tube detector array arranged in a linear fashion with a diffraction grating to measure 400-700 nm emission in 9.6 nm bins. In confocal imaging mode, user defined detection filters sum the fluorescence from the encompassed bins, while in spectral imaging mode, the bins are left un-summed so spectral information can be retained. The point spread functions for confocal images with the 63x/1.40 Oil DIC objective in the X-Y direction were 228 nm (488 nm excitation) and 316 nm (594 nm excitation). Point spread functions were calculated using ZEN black software using emissions from 0.1 nm fluorescent microspheres, prepared on a slide according to manufacturer's instructions (T7279, Thermo Fisher).

In Airyscan superresolution imaging mode, the gallium arsenide phosphide photomultiplier tube array of 32 elements is arranged in a compound eye (or honeycomb) fashion (Zeiss Airyscan 410900-2058-580) to improve the efficiency of light capture compared to a

standard confocal point detector. Images were collected and deconvolved using ZEN black software version 2.1. After deconvolution, the point spread functions for the 63x/1.40 NA objective with 488 nm excitation was 124 nm in X-Y and 216 nm in Z; with 594 nm excitation 168 nm in X-Y and 212 nm in Z. For the 63x/1.2 NA objective, the point spread function with 488 nm excitation was 187 nm in X-Y and 214nm in Z; the point spread function with 594 nm excitation was 210 nm in X-Y and 213 nm in Z.

GxTX–594 dose response time–lapse imaging

Cells were transfected, induced, and plated as described in the "*Transfection*" methods section. ~5 min prior to imaging, the cell culture exchanged in the dish containing the cell–plated coverglass was exchanged with an "imaging solution". The imaging solution consisted of the same 3.5 mM KCl / 1 mM $MgCl_2$ solution used for electrophysiological recordings (see *"Whole–cell ionic current measurements in Kv2.1-CHO cells"*) but was additionally supplemented with 0.1% Bovine serum albumin and 10 mM glucose. Cells were washed in this solution with three, 1 mL washes. The coverslip was then mounted on an imaging chamber (Warner Instrument, Catalog # RC-24E) with vacuum grease. During time lapse imaging, indicated concentrations of GxTX–594 were applied by manual pipetting of a 100 μL bolus that was allowed to sit for 10 minutes. Manual wash–out was accomplished by flushing ~10 mL of imaging solution through the bath using an input syringe and a clearance vacuum. Solutions were added to and removed from the imaging chamber using a syringe at a flow rate of ~1 mL / 10 sec. 15 minutes after wash–out, the next GxTX–594 concentration was added. Temperature inside the microscope housing was 24-28 °C.

Images were taken every 5 sec in Airyscan superresolution imaging mode using the 63x oil objective. The field of view that included cells both positive and negative for AMIGO1–YFP fluorescence to be used as an in-frame imaging control. YFP was excited with the 488 nm line from an argon laser (3.2 mW at installation) powered at 2% through a MBS 488/594 and MBS - 405 beam splitter. YFP emission was detected through a BP 420-488 + BP 495-550 filter. GxTX–594 was excited with 594 nm helium–neon laser (0.6 mW at installation) powered at 2% through a MBS 488/594 beam splitter. GxTX–594 emission was detected through a BP 420-480 and a BP 495-620 filter. Images were collected as 16-bit, 512 x 512 pixel (0.13 μm x 0.13 μm pixel size) images with no averaging and a pixel dwell of 0.85 μs. Images were exported as .czi files and the intensity data was extracted using FIJI (Schindelin et al., 2012). Representative images shown in Fig. 2 were taken with the same aforementioned parameters, but FIJI (Schindelin et al., 2012) was used to linearly adjust the brightness and contrast to optimize display.

To calculate the dissociation constant (K_d) of GxTX–594 binding, the maximum, background–subtracted, fluorescence intensity following GxTX–594 addition was quantified. Plots of fluorescence intensity vs. GxTX–594 concentration curves were normalized to the maximum intensity recorded within each individual experiment and were constrained to 0 by setting the fluorescence intensity at 0 nM GxTX–594 = 0. The resulting curve was fit with a Langmuir binding isotherm to characterize maximum amplitude (A), and K_d (Eqn. K).

$$f(x) = A * \frac{1 - x}{(K_d + x)} \qquad \text{(Eqn. K)}$$

Three individual K_d fit values were derived from independent biological replicates and the reported K_d values represents their average.

Environment–sensitive fluorescence and imaging

GxTX mutants were synthesized by solid phase peptide synthesis as described (Stewart et al., 2021; Fletcher-Taylor et al., 2020; Tilley et al., 2014) with propargylglycine (Pra) substituents at either Ser13 or Lys27. Purified GxTX mutants were conjugated with JP–N_3 as reported (Fletcher-Taylor et al., 2020). Stock solutions of 7 and 73 μm, respectively, were dissolved in 1 mM Arginine buffer (1 M Arg-HCl, 50 mM Glu, pH 5.0 with NaOH) and stored at -80 ºC and thawed on ice. JP conjugates were diluted to 100 nM working concentration using the same 3.5 mM KCl / 1 mM $MgCl_2$ solution used for electrophysiological recordings. Cells were transfected, induced and plated as described in the "*Transfection*" methods section and washed with imaging solution as described in "*GxTX–594 dose response time–lapse imaging*". Following washing, the imaging solution was removed and cells were incubated in 100 μL of GxTX-based labeling solutions for 5-10 minutes in the dark before 1 mL of the imaging solution was used to wash out the excess. All cells were imaged in 1 mL of fresh imaging solution. Temperature inside the microscope housing was 24-28 °C.

Images were taken in lambda scan imaging mode using the 63x oil objective. JP was excited with 543 nm helium–neon laser (0.6 mW at installation) laser powered at 60% through a MBS 488/543 beam splitter. JP emission was detected between 553-695 nm in 9 nm bin spacing. Images were collected as 16-bit, 512 x 512 pixel (0.24 μm x 0.24 μm pixel size) images with 2x averaging and a pixel dwell of 8.24 μs. Images were exported as .czi files and the spectral data was extracted from the converted 8-bit image in Zen Blue.

To better visualize JP labeling, representative images shown in Fig. 9 were taken using confocal imaging mode. These images were not used in analysis but instead used in conjunction with the lambda scan spectral images, (which display a clear YFP emission tail in AMIGO1–positive cells) to identify the AMIGO1–YFP positive cells in each lambda scan image. YFP was excited with the 514 nm line from an argon laser (3.2 mW at installation) laser powered at 2% through a MBS 458/514/594 beam splitter. YFP emission was detected between 519-589 nm. JP was excited with 594 nm helium–neon laser (0.6 mW at installation) powered at 2% through a MBS 458/514/594 beam splitter. JP emission was detected between 599-734 nm. Images were collected as 16-bit, 512 x 512 pixel (0.24 μm x 0.24 μm pixel size) images with 4x averaging and a pixel dwell of 16.5 μs. Representative image contrast and brightness settings were linearly adjusted in FIJI (Schindelin et al., 2012) to optimize display.

Split Pseudo-Voigt fitting

JP emission spectra were fit with two-component split pseudo-Voigt functions using the curve fitting software Fityk 1.3.1 (https://fityk.nieto.pl/), which employed a Levenberg−Marquardt algorithm. Goodness of fit was determined by root-mean-squared deviation (R^2) values, which are listed in Supplemental Table 1 along with the parameters of each component function. Fittings for JP spectra from cells without AMIGO1-YFP included all data from 550-700 nm. To avoid YFP overlap, fittings for spectra from cells expressing AMIGO1-YFP include emission data points from 613-700 nm for GxTX Ser13Pra(JP) and 582-700 nm for GxTX Lys27Pra(JP).

Pearson's correlation coefficient

Pearson's correlation coefficient (PCC) measurements assay protein colocalization at a resolution defined by the point-spread function of the microscope, and encapsulate both signal cooccurrence and correlation (McDonald & Dunn, 2013). For PCC analysis, cells were

transfected and/or induced and plated as described in the "*Transfection*" methods section and washed as described in the "*GxTX–594 dose response time–lapse imaging*" section. ~5 min prior to imaging, cell culture media was exchanged with an "imaging solution". In instances where Kv2.1 was labeled with GxTX–594, cells were then incubated in 100 μL of 100 nM GxTX–594 as described in "*Environment–sensitive fluorescence and imaging".* Cells were incubated in the labeling solutions for 5-10 minutes before 1 mL of the imaging solution was used to wash out fluorescent dyes. All cells were imaged in 1 mL of fresh imaging solution. Temperature inside the microscope housing was 24-28 °C.

Confocal images were collected using the 40x oil objective. YFP was excited with the 514 nm helium-neon laser (0.6 mW at installation) powered at 1% through a MBS 458/514/594 beam splitter. YFP emission was detected between 519-589 nm. GxTX-594 and mRuby were excited with the 594 nm helium-neon laser powered at 2% through the same beam splitter. Emission was detected between 599-734 nm. Images were collected as optically sectioned 8-bit, 2048 x 2048 pixel (0.03 μm x 0.03 μm pixel size) images with 2 averaging and a pixel dwell of 2.06 μs. For glass–adhered images, ROIs were drawn around the inner perimeter of each individual cell. These circular ROIs encapsulated all of the punctae, and the "negative space" between punctae. For solution–exposed membrane images, annulus-shaped regions of interest (ROIs) were drawn manually around the apparent inner and outer boundary of an individual cell to isolate the surface-exposed membrane perimeter. After automatic Costes thresholding, PCC values were calculated using the colocalization function in Zen Blue software. Costes thresholding uses an algorithm to distinguish labeled structures from background and then removes low-intensity values from analysis (Costes et al., 2004; Dunn et al., 2011). Although Costes thresholding decreases the empirical value of a PCC measurement, it is an unbiased form of thresholding designed to account for nonuniformities in background fluorescence both within a singular image and between images (Dunn et al., 2011). High PCC values are only obtained when two fluorescent signals overlap spatially and have linked fluorescent intensities (bright with bright and dim with dim). Perfect colocalization is represented by a value of +1, while a value of -1 represents fluorophores with mutually exclusive compartmentalization. A value of 0 indicates no colocalization, and intermediate positive values indicate some extent of colocalization (McDonald & Dunn, 2013). Representative images in Fig. 3 and Fig. 4 were taken with the 40x objective using confocal mode and exported as 8-bit .czi files to FIJI (Schindelin et al., 2012) to linearly adjust the brightness and contrast linearly to optimize display.

Coefficient of variation

For coefficient of variation (COV) analysis, cells were prepared as described in "*Pearson's correlation coefficient*". COV describes the degree of variability and non-uniformity of a fluorescence signal (Bishop et al., 2018) and has previously been used to describe the degree of punctate-like nature of an ROI as described previously (Bishop et al., 2015; Jensen et al., 2017; Kirmiz, et al., 2018a). Cells with highly clustered fluorescence will have high COV values, while cells with more uniformly distributed fluorescence will have low COV values. COV is calculated as the quotient of the standard deviation of fluorescence intensity between pixels in the ROI and the mean fluorescence intensity of the total ROI. Whenever possible, the same images collected for Pearson's correlation analyses (by the settings detailed in "*Pearson's correlation coefficient*") were used for COV analysis. Since PCC analyses were designed to sample at a rate beyond the Nyquist limit, images were Gaussian filtered (sigma = 1) for COV analyses. Circular ROIs were drawn around the inner perimeter of the glass–adhered membrane

of AMIGO1–YFP expressing cells. All instances of cellular overlap and saturated intracellular expression were excluded from the ROI. Mean fluorescence intensity values and the standard deviation of the means were calculated using Zen Blue software. COV values were computed in Microsoft Excel as standard deviation divided by the mean intensity. Representative images of the Gaussian filtered data were exported as 8-bit .czi files to FIJI to linearly adjust the brightness and contrast to optimize display.

Voltage clamp fluorimetry with GxTX–594

Recording solutions were prepared as follows:

Cell type	External Solution (in mM)	Internal Solution (in mM)
Kv2.1-CHO cells LJP: -5.3 mV	3.5 KCl, 155 NaCl, 10 HEPES, 1.5 $CaCl_2$, 1 $MgCl_2$, adjusted to pH 7.4 with NaOH. Osmolality: 315 mOsm	70 mM CsCl, 50 mM CsF, 35mM NaCl, 1 mM EGTA, 10 mM HEPES, brought to pH 7.4 with CsOH. Osmolality: 310 mOsm

The patch pipette contained a potassium-deficient Cs^+ internal pipette solution to limit outward current and reduce voltage error. Osmolality was measured by a VAPRO vapor pressure osmometer 5520. For each experiment/cell type, internal and external solutions were measured side-by-side on the same day. LJP values were tabulated using Igor's patchers power tools extension version 2.15 (Dr. Francisco Mendez and Frank Wurriehausen, Max-Planck-Institut fur biophysikalische chemie). LJP values were corrected for *post hoc*, offline.

AMIGO1–YFP and Kv2.1 channel expression and GxTX–594 labeling was achieved following the same protocols as described in (Thapa et al., 2021) and were similar to those described in "*GxTX–594 dose response time–lapse imaging".* Briefly, instead of completely washing out GxTX–594 after incubation, the solution was diluted with 1 mL of a bovine serum albumin-deficient imaging solution for a working concentration of 9 nM GxTX-594 during experiments. Cells with obvious GxTX-594 surface staining were selected for whole-cell voltage-clamp stimulation with an EPC-10 patch clamp amplifier (HEKA) run by Patchmaster software, v2x90.2 (HEKA). Borosilicate glass pipettes (Catalog # BF 150-110-10HP, Sutter Instruments) were pulled with blunt tips to resistances less than 3.0 MΩ in these solutions. Cells were held at -100 mV for 30 images and stepped to +35 mV (which was effectively +30 mV, accounting for the -5.3 mV LJP). The voltage step stimulus was maintained until any observed change in fluorescence was complete.

Images were taken every 1 sec in Airyscan superresolution imaging mode using the 63x water objective. GxTX–594 was excited with 594 nm helium–neon laser (0.6 mW at installation) powered at 1% through a MBS 488/594 and MBS -405 beam splitter. GxTX–594 emission was detected through a BP 420-480 and a LP 605 filter. Images were collected as 16-bit, 256 x 256 pixel (0.11 μm x 0.11 μm pixel size) images with 2x averaging and a pixel dwell of 0.85 μs. Images were exported as .czi files and the intensity data was extracted using Zen Blue. Representative images shown in Fig. 8 were taken with the same aforementioned parameters, but FIJI (Schindelin et al., 2012) was used to linearly adjust the brightness and contrast to optimize display.

GxTX–594 dissociation rates

To extract the rate of GxTX–594 dissociation ($k_{\Delta F}$) annular regions of interest were drawn manually around the solution-exposed membrane. The average fluorescence intensity was evaluated over time. Immediately following the voltage stimulus, the fluorescence intensity decreased. The decay was fit with a monoexponential function as done in (Thapa et al., 2021). For presentation, fluorescence intensity traces were subtracted by the minimum intensity value and normalized to the maximum.

GxTX–594 dissociation rate free energy calculations (Method C)

As GxTX–594 binding is determined by the stability of Kv2.1 in the earliest resting conformation, we converted the $k_{\Delta F}$ of GxTX–594 dissociation at +30 mV into a 1.9-fold change in equilibrium constant (K_{eq}) for resting vs. activated voltage sensors (Thapa et al., 2021). To transform the experimentally measured $k_{\Delta F}$ into an approximate K_{eq}, we used the $k_{\Delta F}$ vs. V vs. $P_{Activated,Labeled}$ relationship described in (Thapa et al., 2021). Briefly, experimentally measured $k_{\Delta F}$ values were interpolated onto the $k_{\Delta F}$ vs. V relation. From this interpolation, the $k_{\Delta F}$ values we observed, corresponded to the rates Thapa et al., might observe when stimulating to +13.3 mV (Kv2.1–Control cells) or to +24.7 mV (Kv2.1–AMIGO1 cells). Minor differences in experimental methods made it so neither of these interpolations perfectly corresponded to the expected +30 mV stimuli. Once a representative voltage was identified, an estimate of $P_{Activated,Labeled}$ was also gathered by interpolation. Here $P_{Activated,Labeled}$ represents the probability that a GxTX–594-labeled channel occupies its activated conformation. The quotient of $P_{Activated,Labeled}$ and (1- $P_{Activated,Labeled}$) represents the K_{eq}. $K_{eq,\ Kv2.1}$ / $K_{eq,\ Kv2.1+AMIGO1}$ = 1.9. Summing this energetic perturbation over all 4 voltage sensors yields ΔG_{AMIGO1} was -1.50 kcal/mol (Eqn. L). R and T have been previously described.

$$\Delta G_{k\Delta F} = -4 \times R \times T \times \ln(K_{eq}) \qquad \text{(Eqn. L)}$$

Fluorescence intensity analysis

Fluorescence intensities were calculated from the dose-response data. Fluorescence intensity comparisons between test groups were made between in-frame controls only to control for any use- or time-dependent changes in microscope function or image acquisition that may unknowingly occur. To compare GxTX–594 intensities from CHO cells with or without AMIGO1–YFP, ROIs were drawn to encapsulate every cell for a particular test group (AMIGO1–YFP positive or negative) that was present in a single image. This resulted in two ensemble average intensities for each image, representing 3-8 cells each. Intensity values were background subtracted. GxTX–594 fluorescence intensity values originating from cells negative for AMIGO1–YFP fluorescence were normalized to 1 and the corresponding fluorescence intensities for the image–matched, GxTX–594 fluorescence intensities for AMIGO1–YFP positive cells were proportionally adjusted.

Summary of Supplemental Materials

Supplemental Fig. 1 describes an electrophysiology experiment in which HEK293 cells were transfected with mouse Kv2.1 along with the auxiliary subunit for voltage-gated sodium channels, human SCN1β. From this negative control experiment, we saw no statistically discernable effect on the G–V relation, which supports the conclusion that the G–V shift seen in HEK293 cells transfected with Kv2.1 channels is an effect specifically induced by AMIGO1. Supplemental Fig. 2 is a compilation of potassium current densities measured in HEK293 and Kv2.1–CHO cells. Current densities compared across different expression and cell systems revealed that the level of variation in channel expression was greater in the transient transfection approaches used in HEK293 cells compared to the stable induction approach used in Kv2.1–CHO cells. Supplemental Fig. 3 showcases a time course of confocal images of Kv2.1–CHO cells transfected with or without AMIGO1 and treated with progressively increasing concentrations of GxTX–594 to label Kv2.1 channels. In this experiment we track GxTX–594 intensity with respect to the added concentration of GxTX–594 and by fitting that relation with a

724 Langmuir binding isotherm, we extract a dissociation constant describing GxTX–594 binding
725 affinity. From this experiment, we see no indication that AMIGO1 expression adversely affects
726 GxTX–594 binding to Kv2.1 channels. Supplemental Table 1 is a list of the split pseudo–Voigt
727 fitting parameters used to quantitate the emission maxima of environmentally-sensitive
728 GxTX(JP) conjugates.
729

Results

AMIGO1 shifts the midpoint for activation of Kv2.1 conductance in HEK293 cells

Prior studies have found that AMIGO1 co-transfection shifts the *G–V* relation of GFP-tagged Kv2.1 channels (Maverick et al., 2021; Peltola et al., 2011). To determine whether AMIGO1 modulates the conductance of wild type Kv2.1 similarly, we transfected and voltage clamped cells under conditions similar to the original report (Peltola et al., 2011). HEK293 cells were transfected with either mouse Kv2.1 (mKv2.1 control cells) or mouse Kv2.1 and mouse AMIGO1 (mKv2.1 + AMIGO1 cells) (Fig. 1A). Macroscopic ionic current recordings were made in whole-cell voltage-clamp mode and K^+ conductance was measured from tail currents (Fig. 1B, C). To limit the proportion of currents from endogenous voltage-dependent channels (Ponce et al., 2018; Yu & Kerchner, 1998), we set a minimum outward current density as an inclusion threshold for analysis (65 pA/pF at +85 mV). Of the cells patched, 7 of 18 mKv2.1 control cells and 14 of 28 mKv2.1 + AMIGO1 cells satisfied this inclusion threshold and displayed currents consistent with a Kv2.1 delayed rectifier conductance (I_K) (Supplemental Fig. 1A, B respectively). The *G–V* relations were fit with a 4th power Boltzmann function (Eqn. C) (Fig. 1D, E, F), and average $V_{i,Mid}$ (Fig. 1H) and steepness equivalents (z_i) (Fig. 1G) were determined (Table 1). AMIGO1 did not change the steepness (Δz_i) of the Kv2.1 *G–V* relation, but did shift the $V_{i,Mid}$ ($\Delta V_{i,Mid}$) by -5.7 ± 2.3 mV (SEM). Consistent with the previous reports, these results indicate that AMIGO1 shifts activation of Kv2.1 to more negative voltages. Although this shift is smaller than the -15.3 mV shift of GFP-tagged mouse Kv2.1 induced by mouse AMIGO1–YFP (Peltola et al., 2011), it is on par with the - 6.1 mV shift observed from cotransfection of human AMIGO1–mRuby2 with a rat Kv2.1–GFP protein engineered to contain a biotin acceptor peptide (LB) between S1 and S2 (Maverick et al., 2021).

To test if the shift in Kv2.1 conductance was a nonspecific response of transfecting HEK293 cells with a transmembrane protein, we measured the *G–V* relation of K^+ conductance in cells transfected with Kv2.1 and the sodium channel β subunit SCN1β. SCN1β and AMIGO1 are both single-pass transmembrane proteins with an immunoglobulin domain. Co-transfection with SCN1β did not detectably modulate the Kv2.1 conductance (Table 1 and Supplemental Fig. 1, 2). This result suggests that modulation of Kv2.1 conductance is a specific property of AMIGO1.

Several aspects of the HEK293 cell co-transfection preparation complicated detailed biophysical investigations of the AMIGO1 mechanism. This included inconsistency in the expression level of Kv2.1 channels, endogenous voltage-activated conductances, and the increased variability in $V_{i,Mid}$ measurements made with AMIGO1. The increased variability is apparaent in Fig. 1H where the standard deviation of $V_{i,Mid}$ increased from ± 3.6 mV in control cells to ± 6.9 mV in mKv2.1 + AMIGO1 cells. From our data, we note that the $V_{i,Mid}$ values for mKv2.1 + AMIGO1 cells seemed to partition into two groups: a more negatively shifted group with an average $V_{i,Mid}$ of -13.9 mV (Fig. 1H, dark blue), and a group similar to mKv2.1 alone with an average $V_{i,Mid}$ of -2.5 mV (Fig. 1H, light blue). Although all cells analyzed had GFP fluorescence indicating transfection with the AMIGO1–pIRES2–GFP vector, it is possible that some cells were not expressing sufficient AMIGO1 to have a functional effect. These concerns led us to seek a different expression system for interrogating the AMIGO1–Kv2.1 interaction.

772 Figure 1. AMIGO1 modulates Kv2.1 conductance in HEK293 cells.

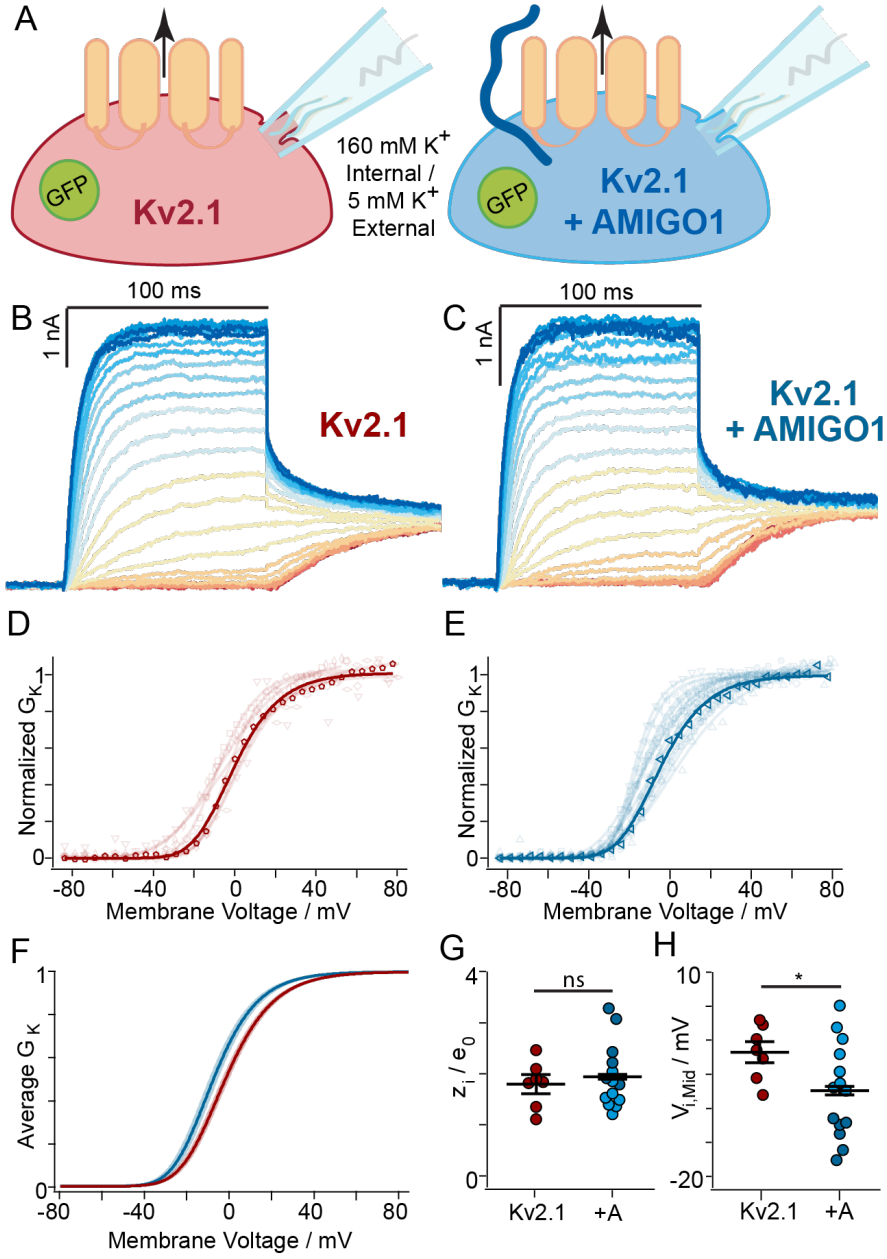

773

774 *Figure 1. AMIGO1 modulates Kv2.1 conductance in HEK293 cells.*

775 **(A)** Experimental set up: HEK293 cells were co-transfected 48 hours prior to whole-cell recording with either
776 mKv2.1 and either GFP (red) or AMIGO1–pIRES2–GFP (blue). K^+ ionic current was recorded (black arrow). (**B**, **C**)
777 Representative Kv2.1 current response elicited from a mKv2.1 control (14.8 pF) or mKv2.1 + AMIGO1 (9.6 pF)
778 HEK293 cell. Cells were given 100 ms voltage steps ranging from -80 mV (dark red trace) to +85 mV (dark blue
779 trace) and then stepped to 0 mV to record tail currents. The holding potential was -80 mV. (**D**, **E** respectively)
780 Normalized *G–V* relationships for mKv2.1 control or mKv2.1 + AMIGO1. Different symbols correspond to
781 individual cells and the bolded trace corresponds to the *G–V* derived from the exemplar cell shown in panels B, C
782 respectively. Solid lines represent 4th order Boltzmann relationships (Eqn. C). (**F**) Reconstructed 4th order
783 Boltzmann fits using the average $V_{i,Mid}$ and z_i (Table 1). Shaded areas represent $V_{i,Mid}$ ± SEM. (**G**) Steepness and (**H**)
784 midpoint of 4th order Boltzmann fits. Bars are mean ± SEM. Unpaired two-tailed, T–tests p-values are in Table 1. *:
785 $p = \leq 0.05$, ns: not significant.

Table 1. Fourth order Boltzmann parameters for G–V relationships.

	Activation (G–V)				ΔG_{AMIGO1} (kcal/mol)
	$V_{i,1/2}$ *(mV)*	$V_{i,Mid}$ *(mV)*	z_i *(e_0)*	*n*	*(Eqn. E)*
HEK293 cells					
mKv2.1 + GFP	-26.8 ± 3.0	-1.7 ± 1.4 [A]	1.79 ± 0.17 [D]	7	-0.32
mKv2.1+ AMIGO1 + GFP	-30.9 ± 0.8	-7.4 ± 1.8 [B]	1.95 ± 0.16 [E]	14	
mKv2.1 + SCNβ1 + GFP	-24.8 ± 1.5	0.2 ± 1.8 [C]	1.720 ± 0.074 [F]	8	
Kv2.1–CHO cells					
rKv2.1 + GFP	-33.4 ± 1.7	-1.8 ± 1.2 [G]	1.411 ± 0.070 [I]	20	-0.21
rKv2.1+ AMIGO1–YFP	-42.0 ± 3.3	-7.6 ± 1.8 [H]	1.40 ± 0.11 [J]	19	
Kv2.1–CHO cells + Mg^{2+}					
rKv2.1 + GFP	-13.8 ± 1.8	17.6 ± 2.2 [K]	1.51 ± 0.11 [M]	18	-0.37
rKv2.1+ AMIGO1–YFP	-16.3 ± 1.5	10.2 ± 1.0 [L]	1.682 ± 0.082 [N]	23	
Kv2.1–CHO cells + GxTX–594					
rKv2.1 + GFP	26.8 ± 2.9	73.2 ± 3.8 [O]	1.03 ± 0.11 [Q]	13	-0.79
rKv2.1+ AMIGO1–YFP	12.9 ± 4.4	50.9 ± 2.8 [P]	1.27 ± 0.14 [R]	12	

Table 1. Fourth order Boltzmann parameters for G–V relationships.

Average $V_{i,1/2}$, $V_{i,Mid}$, and z_i values were derived from a 4th order Boltzmann fits (Eqn. C) of *n* individual cells. All values are given ± SEM Corresponding p-values from unpaired, two-tailed, T–test comparisons are as follows: HEK293 Cells: AB: 0.024. BC: 0.008. AC: 0.41. DE: 0.51. EF: 0.22. DF: 0.71. Kv2.1–CHO Cells: GH: 0.012. IJ: 0.95. Kv2.1–CHO Cells with Mg^{2+}: KL: 0.0051. MN: 0.21. Kv2.1–CHO Cells with GxTX–594: OP: 0.00018. QR: 0.19. ΔG_{AMIGO1} was tabulated using Eqn. E, at the $V_{i,Mid}$ for Kv2.1 control cells, or $V_{i,Mid,Control}$.

Kv2.1 interacts with AMIGO1 in CHO cells

To overcome some of the limitations of the transiently transfected HEK293 system, we used a Chinese Hamster Ovary K1 cell line with inducible rat Kv2.1 expression (Kv2.1-CHO) and transfected this cell line with a YFP-tagged mouse AMIGO1. Unlike HEK293 cells, CHO cells lack the presence of endogenous voltage-gated K^+ currents (Gamper et al., 2005). Inducible Kv2.1 expression permits tight control of current density (Trapani & Korn, 2003) and fluorescence tagging of AMIGO1 permits visualization of protein expression and localization.

As expression systems can influence auxiliary protein interactions with ion channels (Isom et al., 1992; Isom et al., 1995; Kazarinova-Noyes et al., 2001; McEwen & Isom, 2004; Patino et al., 2009), we assessed Kv2.1–AMIGO1 association in these CHO cells. We evaluated two hallmarks of Kv2.1 and AMIGO1 association: whether Kv2.1 expression reorganizes AMIGO1, and whether AMIGO1 and Kv2.1 colocalize (Bishop et al., 2018; Maverick et al., 2021; Peltola et al., 2011).

In HEK293 cells, heterologously expressed AMIGO1 localization is intracellular and diffuse (Bishop et al., 2018; Maverick et al., 2021). However, when co-expressed with Kv2.1, AMIGO1 reorganizes into punctae with Kv2.1, similar to the expression patterns in central neurons (Bishop et al., 2018; Maverick et al., 2021). To determine whether Kv2.1 similarly reorganizes AMIGO1 in CHO cells, the degree of AMIGO1–YFP reorganization was quantified using the Coefficient of Variation (COV), which captures non–uniformity of YFP localization (Kirmiz et al., 2018a). COV was quantified following the limited 1.5 h Kv2.1 induction period used in macroscopic and microscopic K^+ current recordings (Fig. 4, 5, 6, 10) and the prolonged 48 h induction period used for gating current recordings (Fig. 7) or imaging studies (Fig. 8, 9). COVs were compared against an uninduced control (0 h induction) and against an engineered protein, ChroME-mRuby2, which contains the Kv2.1 clustering sequence, but lacks the Kv2.1 voltage sensing and pore forming domains (Lim et al., 2000; Mardinly et al., 2018). COVs were evaluated from the glass-adhered, basal membrane where evidence of reorganization is most notable (Fig. 2). Both $COV_{1.5h}$ and COV_{48h} were greater than the COV_{0h} or $COV_{ChroME\text{-}mRuby}$ control. This result is consistent with Kv2.1 and AMIGO1 association in CHO cells.

Figure 2. Kv2.1 reorganizes AMIGO1 in CHO cells.

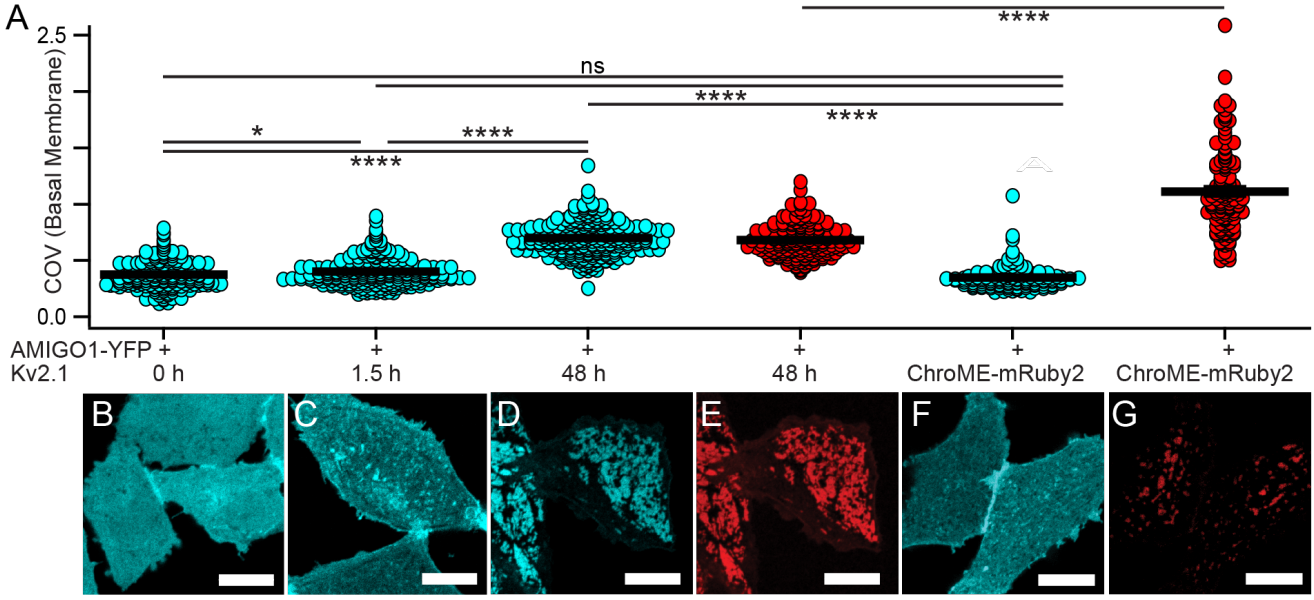

Figure 2. Kv2.1 reorganizes AMIGO1 in CHO cells.

(A) Coefficient of variation of fluorescence from AMIGO1–YFP (blue circles), GxTX–594 (red circles), or ChroME-mRuby2 (red circles). Bars are mean ± SEM. COV measurements were calculated from confocal images acquired from the glass–adhered basal membrane of the cell (exemplar confocal images in B-G). All cells were transfected with AMIGO1–YFP 48 h prior to imaging. AMIGO1–YFP fluorescence from cells (**B**) not induced for Kv2.1 expression (COV_{0h} = 0.3755 ± 0.0097, n = 171), (**C**) induced 1.5 h for Kv2.1 expression ($COV_{1.5h}$ = 0.4023 ± 0.0077, n = 244), (**D**) induced 48 h for Kv2.1 expression (COV_{48h} = 0.7007 ± 0.0086, n = 278). (**E**) GxTX–594 labeling of the cells in panel D ($COV_{48h(GxTX-594)}$ = 0.682 ± 0.010, n = 197 cells). (**F**) AMIGO1–YFP fluorescence from CHO cells lacking Kv2.1 co-transfected with ChroME-mRuby2 (COV = 0.3510 ± 0.0092 n = 129 cells). (**G**) ChroME-mRuby2 fluorescence of cells in panel F ($COV_{(ChroME-mRuby2)}$ = 1.114 ± 0.032, n = 129). Individual cell data from 4 separate transfections were combined for each experimental condition. All scale bars are 10 μm. (**Statistics**) Individual cells were treated as biologically distinct samples for statistical evaluation; a nested/hierarchical model was not used. ****: p = ≤0.0001, *: p = ≤0.05. Two–tailed, T–test: $COV_{0h} \neq COV_{1.5h}$, p = 0.03. $COV_{48h} \neq COV_{1.5h}$, $p = 2.2x10^{-95}$. $COV_{48h} \neq COV_{0h}$, $p = 1.1x10^{-83}$. $COV = COV_{0h}$, p = 0.067. $COV \neq COV_{1.5h}$, $p = 2.47x10^{-5}$. $COV \neq COV_{48h}$, $p = 1.01x10^{-88}$. $COV_{48h(GxTX-594)} \neq COV_{(ChroME-mRuby2)}$, $p = 1.4x10^{-24}$.

838 We also assessed AMIGO1–YFP and Kv2.1 colocalization using the Pearson's
839 correlation coefficient (PCC) (Manders et al., 1992). Surface-expressing Kv2.1 on live cells was
840 labeled with GxTX Ser13Cys(Alexa594) (referred to from here on as GxTX–594), the conjugate
841 of the voltage sensor toxin guangxitoxin-1E derivative Ser13Cys with the maleimide of
842 Alexa594 (Thapa et al., 2021). As auxiliary subunits can impede binding of toxins to voltage-
843 gated ion channels (Das et al., 2016; Gilchrist et al., 2013; Maffie et al., 2013; Messner et al.,
844 1986; Messner & Catterall, 1986; Wilson et al., 2011), we tested whether AMIGO1 impacted
845 GxTX–594 binding to Kv2.1. However, under conditions where AMIGO1 modulates most, if not
846 all, Kv2.1 subunits (Fig. 7, Fig. 8), we found no evidence that AMIGO1 impedes GxTX–594
847 binding to Kv2.1 (Supplemental Fig. 3). Colocalization between AMIGO1–YFP and GxTX–594
848 was apparent as $PCC_{48h,}$ measured from the glass-adhered basal membrane, was greater than the
849 negative control, $PCC_{ChroME\text{-}mRuby2}$ (Fig. 3K-Q). With a limited 1.5 h induction, Kv2.1 was
850 difficult to detect at the glass-adhered basal membrane surface, so we moved the confocal
851 imaging plane further from the cover glass to image Kv2.1 on apical cell surfaces where GxTX-
852 594 labeling was more apparent. On these apical surfaces, $PCC_{1.5h}$ and PCC_{48h} were greater than
853 PCC_{0h} (Fig. 3A-J), consistent with some colocalization of AMIGO1–YFP and Kv2.1. While the
854 increase at the $PCC_{1.5h}$ is minimal, the limited GxTX-594 signal skews signal proportionality,
855 and is expected to depress the PCC value (Dunn et al., 2011). Altogether, the reorganization of
856 AMIGO1 and colocalization with Kv2.1 indicate that AMIGO1 and Kv2.1 interact in the CHO
857 cells used for K^+ current recordings and for gating current measurements.
858

859 Figure 3. AMIGO1 colocalizes with Kv2.1 in CHO cells.

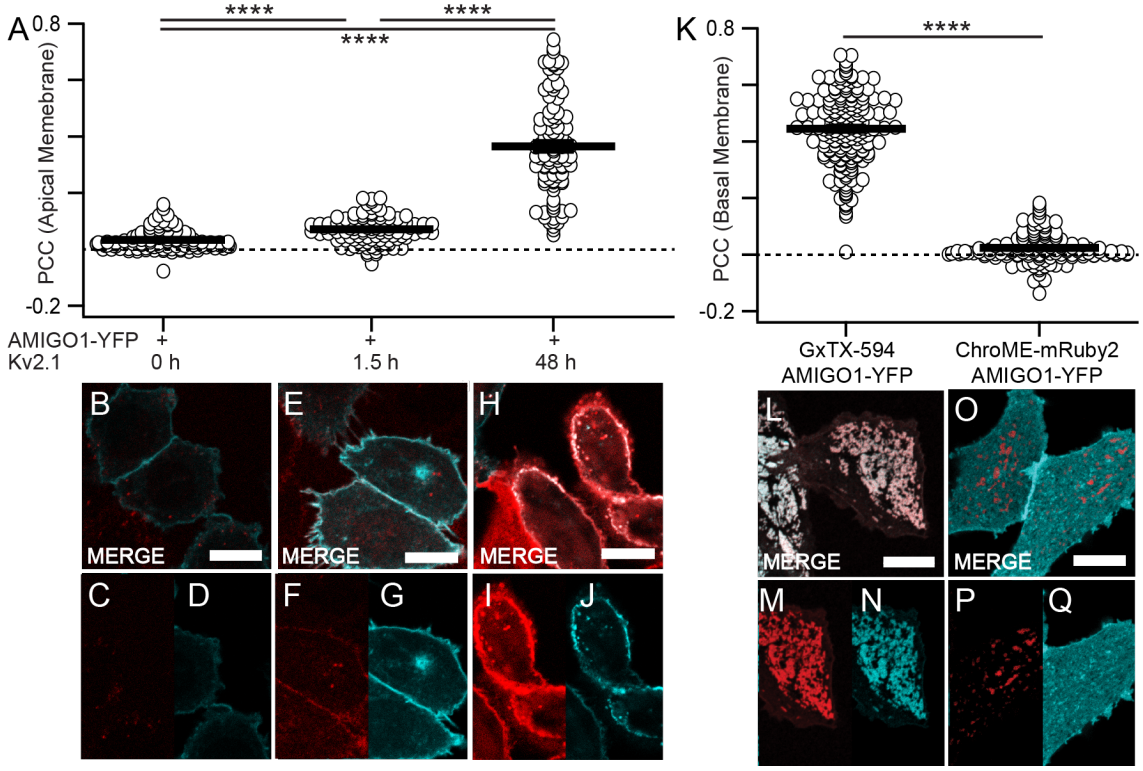

860

861 *Figure 3. AMIGO1 colocalizes with Kv2.1 in CHO cells.*

862 (**A**) Costes thresholded, Pearson's colocalization between AMIGO1–YFP and GxTX–594 at the solution-exposed
863 membrane of the cell following, from left to right, 0, 1.5, or 48 h of Kv2.1 induction (exemplar Confocal images in
864 B-J, brightness/contrast display settings were set to optimize visualization of GxTX–594 labeling at 1.5 h). Because
865 1.5 h of Kv2.1 induction significantly reduces the number of channels available for GxTX–594 labeling, the PCC
866 between AMIGO1–YFP and GxTX–594 was best assessed at a focal plane ~1 μm above the glass–adhered cell
867 surface. On these lateral surfaces, GxTX–594 labeling of surface–expressing Kv2.1 channels were isolated by
868 annular regions of interest bounded by concentric circles drawn around the inner and outer periphery of the cell
869 membrane. From left to right: $PCC_{0h} = 0.0344 \pm 0.0036, \geq 0$ (p–value = $6.7x10^{-16}$, one–tailed, T–test), $n = 103$,
870 $PCC_{1.5h} = 0.0718 \pm 0.0042, \geq 0$ (p–value = 0, one–tailed, T–test), $n = 118$, and $PCC_{48h} = 0.365 \pm 0.017, \geq 0$ (p–value
871 = 0, one–tailed, T–test), $n = 101$. Individual cell data from 3 separate transfections were combined for each
872 experimental condition. (**B**, **C**, **D respectively**) Merge overlay (white, B) shows colocalization between GxTX–594
873 (C) and AMIGO1–YFP (D) in cells not induced for Kv2.1 expression. (**E**, **F**, **G respectively**) Merge overlay (white,
874 E) shows colocalization between GxTX–594 (F) and AMIGO1–YFP (G) in cells induced for Kv2.1 expression 1.5 h
875 prior to imaging. (**H**, **I**, **J respectively**) Merge overlay (white, H) shows colocalization between GxTX–594 (I) and
876 AMIGO1–YFP (J) in cells induced for Kv2.1 expression 48 h prior to imaging. (**K**) Costes thresholded, Pearson's
877 colocalization between (left to right) AMIGO1–YFP/GxTX–594 and AMIGO1–YFP/ChroME-mRuby2 at the glass-
878 adhered basal membrane of the cell. Exemplar images in Fig. 2 D-G. From left to right: $PCC_{GxTX-594} = 0.4449 \pm$
879 $0.0090, \geq 0$ (p–value = 0, one–tailed, T–test), $n = 195$, from 3 transfections; $PCC_{ChroME-mRuby2} = 0.0242 \pm 0.0045, \geq 0$
880 (p–value = $1.7x10^{-7}$, one–tailed, T–test), $n = 129$, from 4 transfections. (**Statistics and plotting**) All scale bars are 10
881 μm. Arithmetic means and standard errors are plotted. Individual cells were treated as biologically distinct samples
882 for statistical evaluation; a nested/hierarchical model was not used. ****: $p = \leq 0.0001$. Two–tailed, T–test: $PCC_{0h} \neq$
883 $PCC_{1.5h}$, $p = 7.4x10^{-11}$, $PCC_{1.5h} \neq PCC_{48h}$, $p = 8.8x10^{-33}$, $PCC_{0h} \neq PCC_{48h}$, $p = 6.4x10^{-37}$. $PCC_{GxTX-594} \neq PCC_{ChroME-mRuby2}$, $p = 3.3x10^{-121}$. $PCC_{1.5h} \neq PCC_{ChroME-mRuby2}$, $p = 1.3x10^{-13}$. $PCC_{0h} \neq PCC_{ChroME-mRuby2}$, p = 0.039.

AMIGO1 shifts the midpoint of activation of Kv2.1 conductance in CHO cells

To determine whether AMIGO1 affected the macroscopic K^+ conductance in Kv2.1–CHO cells, we conducted whole-cell voltage clamp recordings. Cells were transfected with GFP (Kv2.1 control) or with AMIGO1–YFP (Kv2.1 + AMIGO1 cells) and identified for whole-cell voltage clamp based on the presence of cytoplasmic GFP fluorescence or plasma membrane-associated YFP fluorescence, respectively (Fig. 4A). K^+ conductance was measured from tail currents (Fig. 4B, C) and the resulting G–V relations were fit with a 4th power Boltzmann function (Eqn. C) (Fig. 4D, E, F) (Table 1). In Kv2.1 control cells, the $V_{i,Mid}$ was -1.8 mV (Fig. 4H), consistent with prior reports of $V_{i,Mid}$ ranging from -3 mV to +8 mV in CHO cells (Cobb et al., 2016; Maverick et al., 2021; Scholle et al., 2004; Tilley et al., 2014). In Kv2.1 + AMIGO1 cells, the $V_{i,Mid}$ was negatively shifted (Fig. 4H) producing a mean $\Delta V_{i,Mid}$ of -5.7 ± 2.2 mV (SEM) compared to control (Table 1).

To test if AMIGO1 also alters the rate of activation for Kv2.1 conductance we analyzed macroscopic activation kinetics. 10-90% of the rise of Kv2.1 currents following a voltage step (Fig. 4A, B) was fit with the power of an exponential function (Eqn. F), which has three free parameters: the final amplitude (A), the sigmoidicity (σ) which quantifies delay before current rise, and the activation time constant (τ_{act}) which is determined by the rate of the slowest step in the activation path. σ was not significantly altered by AMIGO1 (Fig. 4J, L, N), suggesting that the Kv2.1 activation pathway retains a similar structure with AMIGO1 (Tilley et al., 2019). At a subset of voltages less than +70 mV, AMIGO1 expression accelerated activation, decreasing τ_{act} (Fig. 4I, K, M). A similar trend was observed with AMIGO1–mRuby2 and GFP–Kv2.1–LB in HEK293 cells (Maverick et al., 2021). A model of Kv2.1 activation kinetics suggests that voltage sensor dynamics influence τ_{act} below ~+70 mV, and that at more positive voltages a slow pore opening step limits kinetics (Tilley et al., 2019). From this result we see no indication that AMIGO1 modulates the conformational change associated with the slow pore opening step, but do find evidence that suggests AMIGO1 speeds voltage sensor movement.

911 Figure 4. AMIGO1 shifts the midpoint and speeds activation of the Kv2.1 conductance in CHO
912 cells.

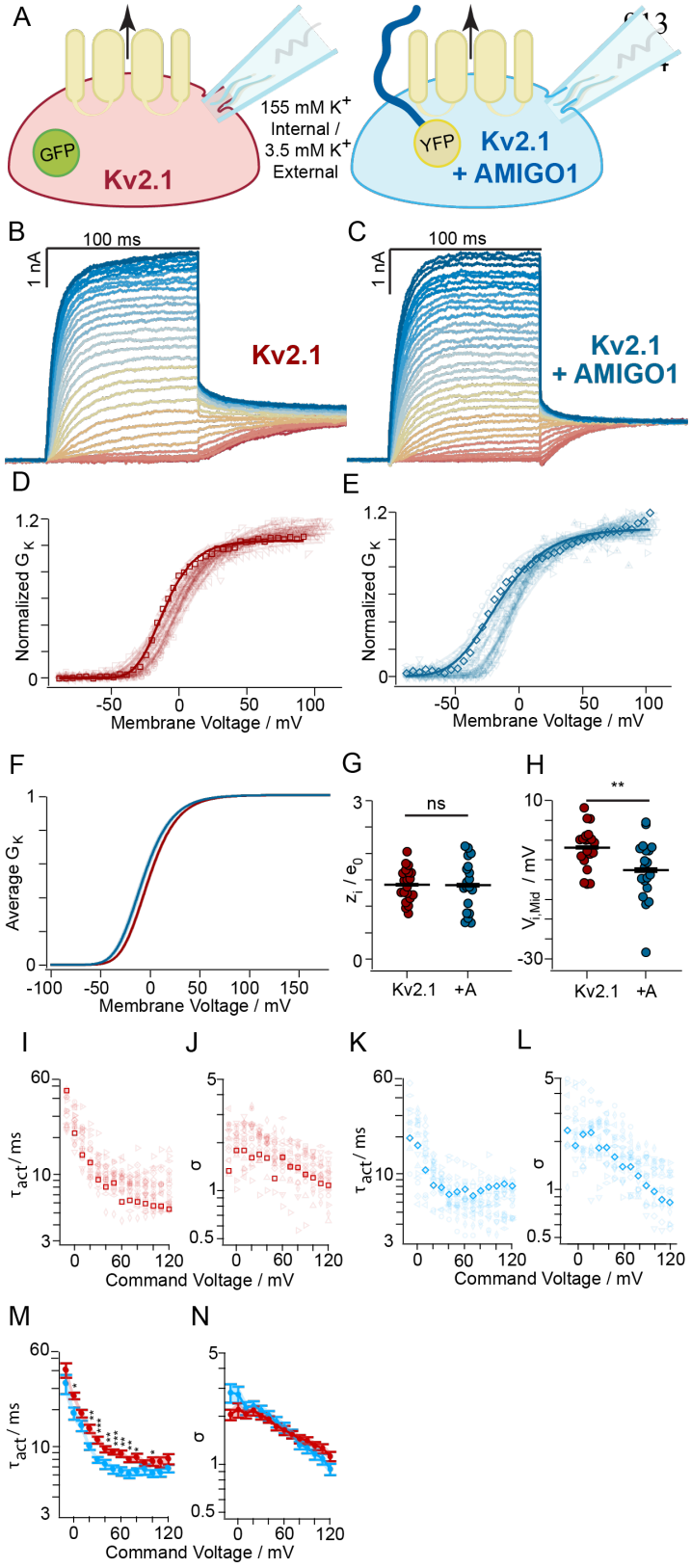

Figure 4. AMIGO1 shifts the midpoint and speeds activation of the Kv2.1 conductance in CHO cells.

(**A**) Experimental set up: Kv2.1–CHO cells were transfected 48 hours prior to whole-cell recording with either GFP (red) or AMIGO1–YFP (blue). Kv2.1 expression was induced by incubation with minocycline for 1–2 hours prior to recording. Macroscopic K^+ ionic current was recorded (black arrow). (**B**, **C**) Representative Kv2.1 current response elicited from a Kv2.1 control (6.0 pF) or Kv2.1 + AMIGO1 (14.5 pF) cell. Cells were given 100 ms voltage steps ranging from -80 mV (dark red trace) to +120 mV (dark blue trace) and then stepped to 0 mV to record tail currents. The holding potential was -100 mV. (**D**, **E respectively**) Normalized *G–V* relationships for Kv2.1 control or Kv2.1 + AMIGO1 cells. Different symbols correspond to individual cells and the bolded trace corresponds to the *G–V* derived from the exemplar cell shown in panels B, C respectively. Solid lines represent 4th order Boltzmann relationships (Eqn. C). (**F**) Reconstructed 4th order Boltzmann fits using the average $V_{i,Mid}$ and the average z_i (Table 1). Shaded areas represent $V_{i,Mid}$ ± SEM. (**G**) Steepness and (**H**) midpoint of 4th order Boltzmann fits. Bars are mean ± SEM. (**I**, **K respectively**) τ_{act} and (**J**, **L respectively**) σ from fitting of Eqn. F onto the activation phase of Kv2.1 control (n = 19) or Kv2.1 + AMIGO1 (n = 18) currents. The bolded symbols correspond to the representative current response shown in (B/D or C/E). (**M**) Mean τ_{act} and (**N**) σ following each command voltage step. Bars are mean ± SEM. (**Statistics G**, **H**, **M**, **N**) Unpaired two-tailed, T–test p-values are in Table 1. ***: $p = \leq 0.001$, **: $p = \leq 0.01$, *: $p = \leq 0.05$, ns: not significant.

Effects of AMIGO1 on pore opening conformational changes were not apparent in single channel recordings

To more directly assess whether the pore opening step of the Kv2.1 activation pathway is modulated by AMIGO1, we analyzed pore openings of single Kv2.1 channels (Fig. 5A, B). Neither the single channel current amplitude (Fig. 5C, D, E) nor the intra–sweep open probability (Fig. 5F) were significantly impacted by AMIGO1. AMIGO1 did not impact the single channel open or closed dwell times in a statistically significant manner (Fig. 5 G-L). In all analyses, effects of AMIGO1 on single channel openings were not apparent. The lack of a detectable difference in open probability was not surprising, given the substatial variability in open probability from patch to patch. These results constrain any impact of AMIGO1 coexpression on Kv2.1 pore opening to be smaller than the variability in these single channel measurements.

944 Figure 5. Effects of AMIGO1 on pore opening conformational changes were not apparent
945 in single channel recordings.

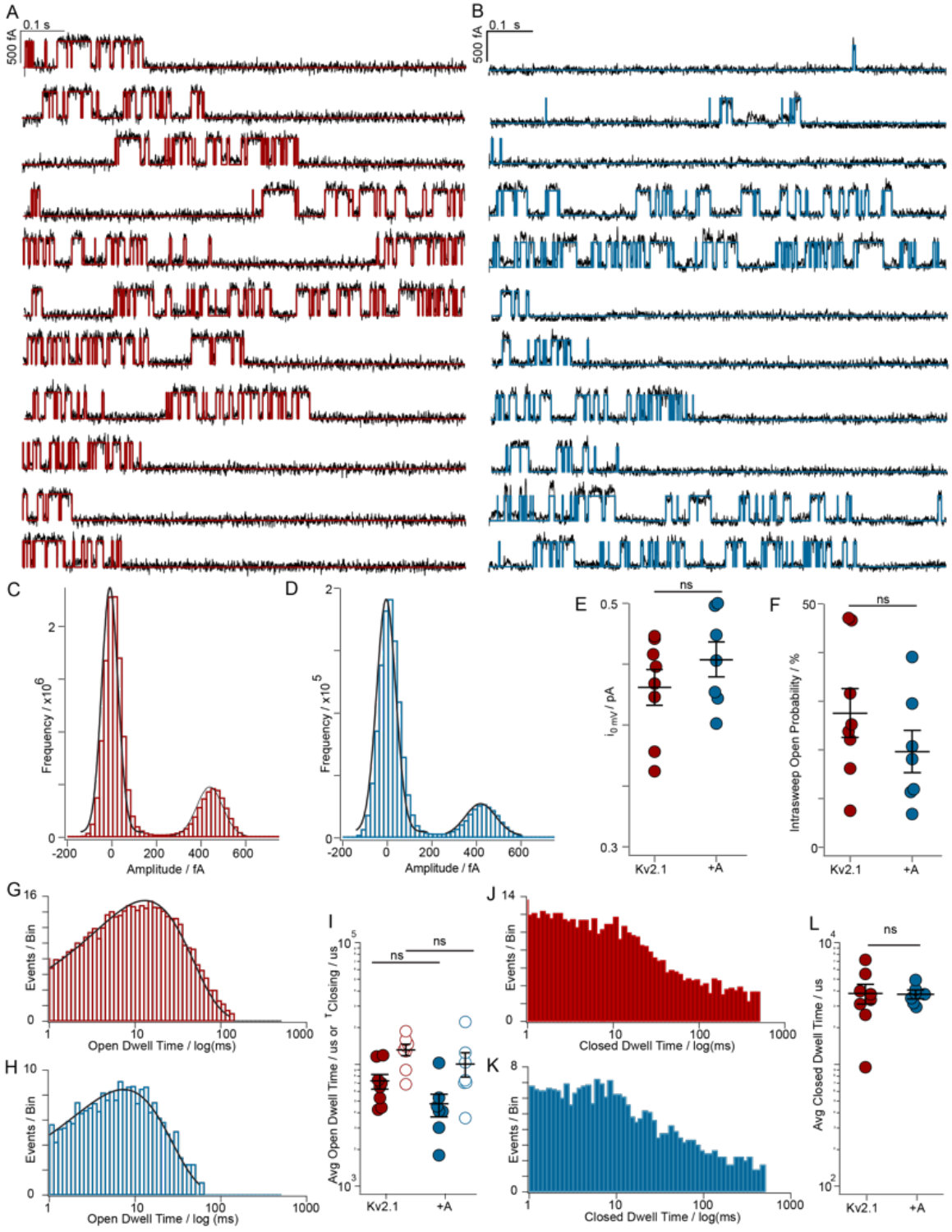

946

Figure 5. Effects of AMIGO1 on pore opening conformational changes were not apparent in single channel recordings.

(**A**, **B**) Representative single channel current responses from Kv2.1–CHO cells transfected 48 hours prior to on-cell recording with either GFP (red) or AMIGO1-YFP (blue). Kv2.1 expression was induced by incubation with minocycline for 1.5 hours prior to recording. Cells were given a 1 s long, 0 mV step from a -100 mV holding potential to stimulate Kv2.1 openings. Current responses were subtracted for leak currents and capacitive transients. Smooth lines represent idealization that was used to distinguish fully open state from the fully closed state. 8 Kv2.1–control single channel patches and 7 Kv2.1+AMIGO1 single channel patches were analyzed. (**C**, **D respectively**) Representative current histograms at +0 mV from the patched cell in A/B. Solid lines represent Gaussian fits to histogram peaks; the peak amplitudes of which were used to idealize the fully open and closed state. (**E**) Mean single channel current amplitude from Gaussian histogram fits to individual patches. Kv2.1 control: $4.3 \times 10^{-13} \pm 1.4 \times 10^{-14}$ A (SEM). Kv2.1 + AMIGO1: $4.5 \times 10^{-13} \pm 1.5 \times 10^{-14}$ A (SEM). Bars are mean ± SEM. Unpaired two-tailed, T–test p-value > 0.05. (**F**) Open probability of Kv2.1 channels was determined from the integral of current histograms above half-amplitude threshold. Kv2.1 control: 28 ± 4.9% (SEM). Kv2.1 + AMIGO1: 20 ± 4.2% (SEM). Bars are mean ± SEM. Two-tailed, T–test p-value > 0.05. (**G**, **H respectively**) Log-binned open dwell-time distributions and single exponential fits for Kv2.1 control or Kv2.1 + AMIGO1 cells. The distributions of open dwell times were determined from idealized currents which were classified as either open or closed using a half–amplitude threshold criterion. Y axis is square root scaling. (**I**) Open dwell times from all individual openings in a single patch were derived in two ways: from the arithmetic mean of all individual open dwell times and also from a single exponential fit of the log square root transform of all open dwell times (Sigworth & Sine, 1987). Arithmetic mean open dwell times (closed circles) Kv2.1 control: 12000 ± 1000 μs (SEM). Kv2.1 + AMIGO1, 9400 ± 2100 μs (SEM). Microscopic time constant of closing from individual patches derived from single exponential fits (open circles). Kv2.1 control: 13000 ± 1300 μs (SEM). Kv2.1 + AMIGO1: 9980 ± 2300 μs (SEM). Bars are mean ± SEM. Unpaired two-tailed, T–test p-value > 0.05. (**J**, **K respectively**) Log-binned closed dwell time distribution for Kv2.1 control or Kv2.1 + AMIGO1 cells. Similar to the open dwell time distributions, the distributions of closed dwell times were determined from idealized currents. (**L**) Arithmetic mean closed dwell time spanning all individual openings in a single patch (closed circles). Kv2.1 control: 3800 ± 670 μs (SEM). Kv2.1 + AMIGO1: 3730 ± 250 μs (SEM). Bars are mean ± SEM. Two-tailed, T–test p-value > 0.05.

A voltage sensor toxin enhances modulation AMIGO1 of the Kv2.1 conductance

To test whether AMIGO1 modulation is dependent on the conformation of the voltage sensors, we altered voltage sensor movement with a voltage sensor toxin. GxTX binds to the voltage sensing domain of Kv2.1 (Milescu et al., 2009), such that exit from the channel's earliest resting conformation is the primary limitation to opening (Tilley et al., 2019). If AMIGO1 modulates the earliest resting conformation of the voltage sensors, then AMIGO1 might have a greater impact when exit from that conformation limits opening. Hence, GxTX would be expected to amplify the AMIGO1 impact on the pore opening equilibrium. Alternately, if AMIGO1 acts directly on pore opening, the AMIGO1 impact on the pore opening equilibrium should be insensitive to voltage sensor modulation. To distinguish between these possibilities, we measured AMIGO1 modulation in the presence of GxTX–594, a GxTX derivative that acts by the same mechanism as GxTX (Thapa et al., 2021) and binds Kv2.1 similarly with or without AMIGO1 (Supp. Fig. 3). We applied 100 nM GxTX–594 to cells and activated the Kv2.1 conductance with 100-ms activating pulses, much shorter than the >2 second time constants of GxTX–594 dissociation at extreme positive voltages (Thapa et al., 2021), and we saw no evidence of GxTX–594 dissociation. The AMIGO1 $\Delta V_{i,Mid}$ of -22.1 ± 4.8 (SEM) with GxTX–594 was distinct from the AMIGO1 $\Delta V_{i,Mid}$ of -5.7 ± 2.2 mV (SEM) without GxTX–594 ($p = 0.00018$, unpaired, two-tailed T-test), suggesting AMIGO1 has a greater impact on the Kv2.1 conductance when voltage sensor movement was altered. The τ_{act} values of Kv2.1 + AMIGO1 cells were not statistically different from Kv2.1 control cells (Fig. 6M). Most σ values were not statistically different with the presence of AMIGO1 (Fig. 6J, L, N). We calculated a pore opening equilibrium constant (K_{eq}) from Boltzmann fits to G–V relations and estimated that AMIGO1 shifts K_{eq} for pore opening by 1.4-fold under control conditions or 3.7-fold in 100 nM GxTX. This result indicates that the impact AMIGO1 has on the Kv2.1 conductance is dependent on the details of the activation path. Further this result indicates that AMIGO1 opposes the action of GxTX, suggesting that AMIGO1 may destabilize the earliest resting conformations of Kv2.1 voltage sensor.

Figure 6. The voltage sensor toxin, GxTX–594, enhances modulation by AMIGO1 on Kv2.1 conductance.

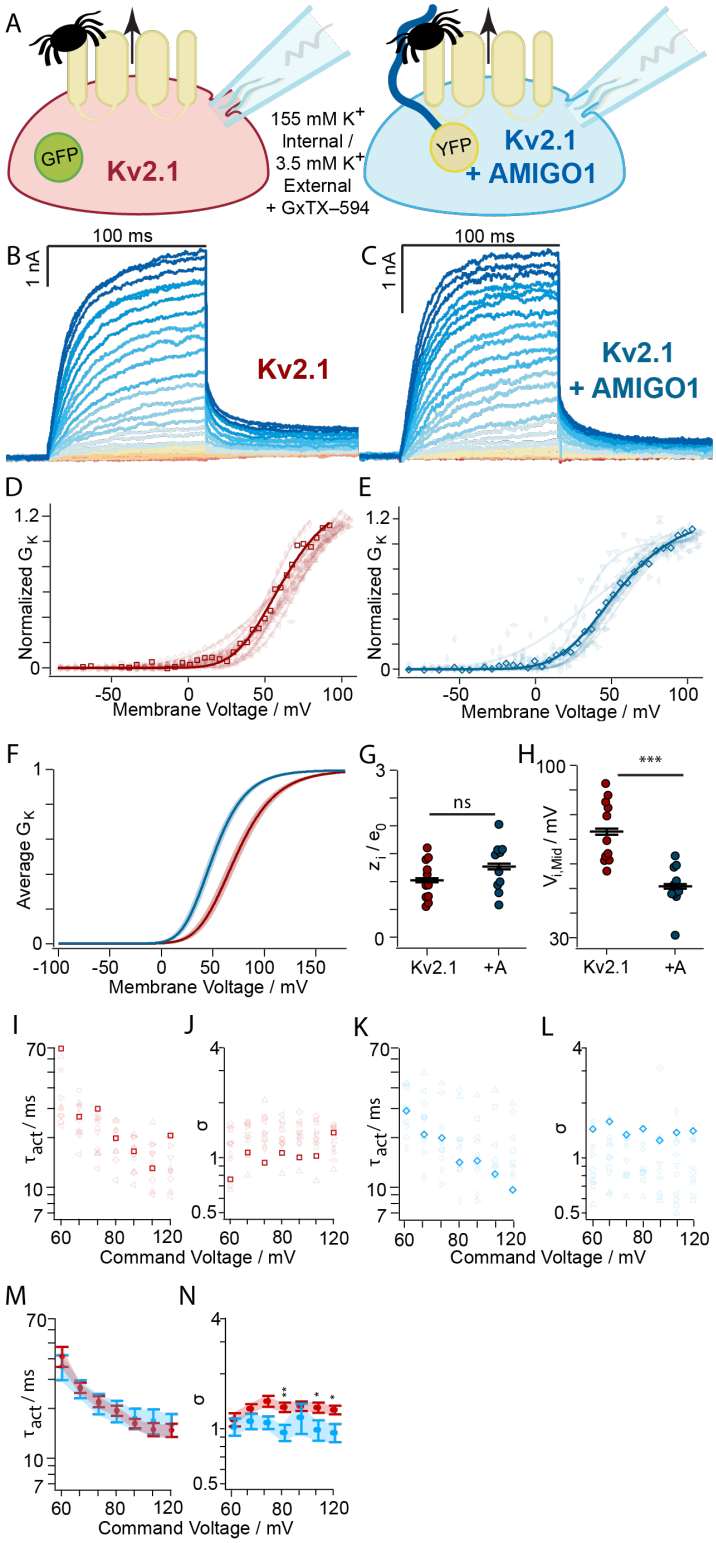

Figure 6. The voltage sensor toxin, GxTX–594, enhances modulation by AMIGO1 on Kv2.1 conductance.

(**A**) Experimental set up: Kv2.1–CHO cells were transfected 48 hours prior to whole–cell recording with either GFP (red) or AMIGO1-YFP (blue). Kv2.1 expression was induced by incubation with minocycline for 1-2 hours prior to recording. After initial whole cell recordings (Fig. 4), cells treated with 100 nM GxTX–594 (tarantulas), for 5 minutes and then additional macroscopic K^+ ionic currents were recorded (black arrow). (**B, C**) Representative Kv2.1 current response elicited from a Kv2.1 control (6.0 pF) or Kv2.1 + AMIGO1 (14.5 pF) cell. Cells were given 100 ms voltage steps ranging from -80 mV (dark red trace) to +120 mV (dark blue trace) and then stepped to 0 mV to record tail currents. The holding potential was -100 mV. (**D, E respectively**) Normalized *G-V* relationships for Kv2.1 control or Kv2.1 + AMIGO1 cells. Different symbols correspond to individual cells and the bolded trace corresponds to the *G–V* derived from the exemplar cell shown in panels B, C respectively. Solid lines represent 4th order Boltzmann relationships (Eqn. C). (**F**) Reconstructed 4th order Boltzmann fits using the average $V_{i,Mid}$ and the average z_i (Table 1). Shaded areas represent $V_{i,Mid}$ ± SEM. (**G**) Steepness and (**H**) midpoint of 4th order Boltzmann fits. Bars are mean ± SEM (**I, K respectively**) Values of τ_{act} from fitting of Eqn. F onto the activation phase of Kv2.1 control (n = 11) or Kv2.1 + AMIGO1 (n = 11) currents. The bolded symbols correspond to the representative current response shown in (B/D or C/E). (**J, L respectively**) Values of σ from fitting of Eqn. F onto the activation phase of Kv2.1 control or Kv2.1 + AMIGO1 currents. The bolded symbols correspond to the representative current response shown in (B/D or C/E). (**M**) Mean τ_{act} and (**N**) σ in the presence of 100 nM GxTX–594, following each command voltage step. Bars are mean ± SEM. (**Statistics G, H, M, N)** Unpaired, two-tailed T–test p-values are in Table 1. **: p = ≤0.01, *: p = ≤0.05, ns: not significant.

AMIGO1 facilitates the activation of Kv2.1 voltage sensors

To determine if AMIGO1 affects voltage sensor movement, we measured gating currents (I_g), which correspond to movement of Kv2.1 voltage sensors across the transmembrane electric field. Kv2.1–CHO cells were patch clamped in whole–cell mode in the absence of K^+ (Fig. 7A), and given voltage steps to elicit gating currents (Fig. 7B, C). The resolvable ON gating currents ($I_{g,ON}$) represent an early component of gating charge movement, but not all of the total gating charge; the later charge movements, which include any charge associated with the pore opening, move too slowly for us to resolve accurately in ON measurements (Scholle et al., 2004; Tilley et al., 2019). If AMIGO1 acts solely through the pore we would not expect to detect an impact on this early component of ON gating currents.

At voltages above 50 mV, the charge density translocated over the first 3.5 ms, $Q_{ON,fast}$, was not significantly different with AMIGO1 (Fig. 7D, E, F), indicating that AMIGO1 did not alter the total charge translocated during early conformational transitions. However, between -10 mV and +50 mV, Kv2.1 control cells did not move as much gating charge as Kv2.1 + AMIGO1 cells, indicating a shift in the threshold for gating current activation (Fig. 7F). The shift in voltage dependence was quantified by fitting the normalized $Q_{ON,fast}$–V with a single Boltzmann fit (Fig. 7G, H, I) yeilding $\Delta V_{g,Mid,ON,fast}$ of -12.8 ± 3.5 mV (SEM) (Fig. 7K) and a $\Delta z_{g,ON,fast}$ of 0.215 ± 0.058 e_0 (SEM) (Fig. 7J) (Table 2). This result indicates that AMIGO1 modulates the early gating charge movement which occurs before pore opening.

To determine whether AMIGO1 modulates the kinetics of early gating charge movement, we extracted a time constant (τ_{ON}) from the decay phase of $I_{g,ON}$ that occurs before 10 ms (Fig. 7B top, C top) (Eqn. G) as in (Tilley et al., 2019). In Kv2.1 + AMIGO1 cells, the τ_{ON}–V relation shifts to more negative voltages compared to control (Fig. 7L, M, N). Above +30 mV, the mean τ_{ON} for Kv2.1 + AMIGO1 cells was faster than the mean τ_{ON} from Kv2.1 control cells (Fig. 7N). Fitting the τ_{ON}-V with rate theory equations indicated AMIGO1 accelerates the foward rate of gating charge movement by 1.7x at neutral voltage and decreases the voltage dependence of this rate by 13% (Fig. 7N). This result indicates that voltage sensors activate faster in the presence of AMIGO1, consistent with destabilization of the earliest resting conformation of the the voltage sensors by AMIGO1.

To measure if AMIGO1 alters the total gating charge movement, we integrated OFF gating currents ($I_{g,OFF}$) at -140 mV after 100 ms voltage steps (Fig. 7B bottom, C bottom, O, P, Q). The density of Q_{OFF} elicited by voltage steps above -10 mV was not significantly different between Kv2.1 control and Kv2.1 + AMIGO1 cells (Fig. 7Q), indicating that AMIGO1 did not alter the density of channels expressed, nor the total gating charge per channel. However, between -25 mV and -10 mV, Kv2.1 control cells did not move as much gating charge as Kv2.1 + AMIGO1 cells, indicating a shift in voltage dependence (Fig. 7Q). Boltzmann fits (Fig. 7R, S, T), yeilded $\Delta V_{g,Mid,OFF}$ of -10.8 ± 2.4 mV (SEM) (Fig. 7V) and a $\Delta z_{g,OFF}$ of 0.43 ± 0.20 e_0 (SEM) (Fig. 7U) (Table 2), indicating that AMIGO1 shifts total gating charge movement to more negative voltages. Overall, we find that AMIGO1 affects every aspect of gating current movement. As both $Q_{ON,fast}$ –V and $\tau_{0mV,\alpha}$ measurements report the gating charge movements out of the earliest resting conformation, these results indicate that AMIGO1 destabilizes the earliest resting conformation relative to voltage sensor conformations later in the conduction activation pathway of Kv2.1.

1068 Figure 7. AMIGO1 facilitates the activation of Kv2 voltage sensors.

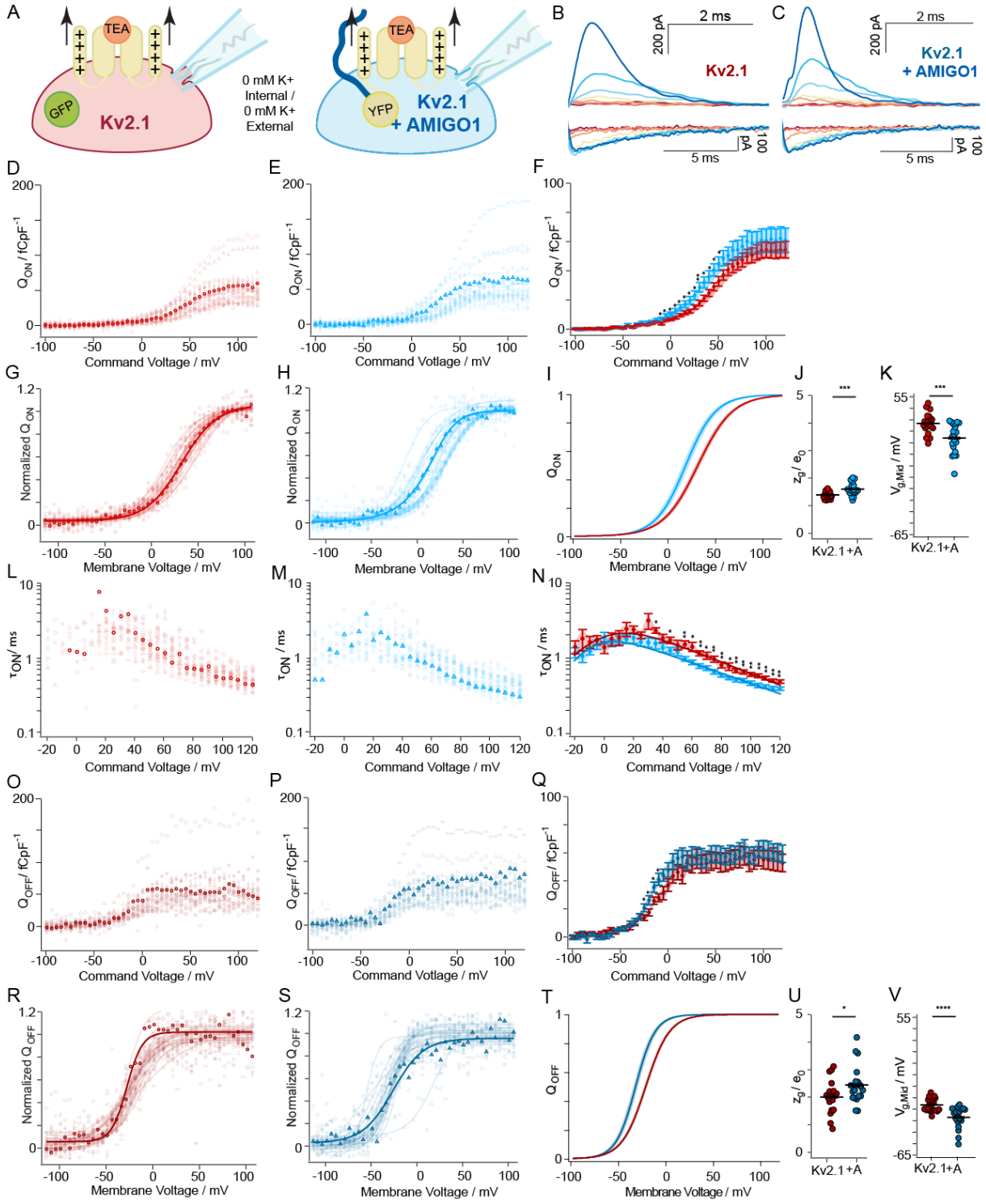

1069

Figure 7. AMIGO1 facilitates the activation of Kv2 voltage sensors.

Experimental set up: Kv2.1–CHO cells were simultaneously induced for Kv2.1 expression and transfected with either GFP (red) or AMIGO1-YFP (blue) 48 hours prior to whole–cell recording. Macroscopic K^+ currents were inhibited by the addition of the Kv2 pore-blocker, TEA (orange), and by removal of free K^+ ions. Gating currents (black arrows) were recorded. (**B, C**) Top/Bottom: Representative $I_{g,ON}/I_{g,OFF}$ response elicited from a Kv2.1 control (11.9 pF) or Kv2.1 + AMIGO1 (8.2 pF) cell. Cells were given 100 ms voltage steps ranging from -100 mV (dark red trace) to +120 mV to record $I_{g,ON}$ and then stepped to -140 mV to record $I_{g,OFF}$. The holding potential was -100 mV. For presentation, only voltage pulses to -100, -50, -25, +0, +25, +50, and +100 mV are presented. (**D, E respectively**) $Q_{ON,fast}/pF$ for Kv2.1 control and Kv2.1 + AMIGO1 cells was calculated by normalizing the area under the raw $I_{g,ON}$ traces by cell size. Bolded circle data corresponds to exemplar cell shown in B, C. (**F**) $Q_{ON,fast}/pF–V$ relation. Bars are mean ± SEM. (**G, H respectively**) Normalized $Q_{ON,fast}–V$ relation from D/E. The bolded trace corresponds to the representative current response shown in D, E. Solid lines represent 1st order Boltzmann relationship fit (Eqn. C). (**I**) Reconstructed Boltzmann fits using the average $V_{g,Mid,ON,fast}$ and the average $z_{g,ON,fast}$ (Table 2). Shaded areas represent $V_{g,Mid,ON,fast}$ ± SEM. (**J**) Steepness and (**K**) midpoint of 1st order Boltzmann fits. Bars are mean ± SEM. (**L, M respectively**) Values of τ_{ON} from fitting of Eqn. G to the rising and falling phase of the ON gating currents shown in B/C from Kv2.1 control cells (n = 20) or Kv2.1 + AMIGO1 cells (n = 20). (**N**) $\tau_{ON}–V$. Bars are mean ± SEM. Solid lines represent Eqn. H fit. Fit values for Kv2.1 control cells: $k_{0mV,\alpha}$ = 254 ± 26 s^{-1}, z_α = 0.468 ± 0.026 e_0, $k_{0mV,\beta}$ = 261 ± 50 s^{-1}, z_β = -1.31 ± 0.37 e_0. Fit values for Kv2.1 + AMIGO1 cells: $k_{0mV,\alpha}$ = 443 ± 26 ms^{-1}, z_α = 0.405 ± 0.019 e_0, $k_{0mV,\beta}$ = 157 ± 52 ms^{-1}, z_β = -2.00 ± 0.55 e_0.Fit values are reported ± SD. (**O, P respectively**) Q_{OFF}/pF for Kv2.1 control and Kv2.1 + AMIGO1 cells was calculated by normalizing the area under the raw $I_{g,OFF}$ traces by cell size. Bolded circle data corresponds to exemplar cell shown in B, C. (**Q**) $Q_{OFF}/pF–V$ relation. Bars are mean ± SEM. (**R, S respectively**) Normalized $Q_{OFF}–V$ relation from O/P. The bolded trace corresponds to the representative current response shown in D/O, E/P. Solid lines represent 1st order Boltzmann relationship fit (Eqn. C.). (**T**) Reconstructed Boltzmann fits using the average $V_{g,Mid,OFF,fast}$ and the average $z_{g,OFF,fast}$ (Table 2). Shaded areas represent $V_{g,Mid,OFF,fast}$ ± SEM (**U**) Steepness and (**V**) midpoint of 1st order Boltzmann fits. Bars are mean ± SEM. (**Statistics and plotting**) Unpaired, two-tailed, T–test p-values are in Table 2. ****: $p \leq$ 0.0001, ***: $p \leq$0.001, **: $p \leq$0.01, *: $p \leq$0.05, ns: not significant.

1097 Table 2. Boltzmann parameters and Δ*G* calculations for voltage sensor movement.

Kv2.1–CHO cells	Activation (*Q–V*)				ΔG_{AMIGO1} (kcal/mol)		
$Q_{ON,fast}$	$V_{g,Mid}$ *(mV)*		z_g (e_0)	*n*	*Eqn. E*		
rKv2.1 + GFP	30.6 ± 2.0 [S]		1.38 ± 0.03 [U]	20	-1.92		
rKv2.1+ AMIGO1–YFP	17.8 ± 2.9 [T]		1.61 ± 0.05 [V]	20			
Q_{OFF}	$V_{g,Mid}$ *(mV)*	$V_{g,Med}$ *(mV)*	z_g (e_0)	*n*	*Eqn. E*	*Eqn. J**	*Eqn. J*°*
rKv2.1 + GFP	-22.0 ± 1.3 [W]	-19.5	2.00 ± 0.13 [Y]	20	-2.45	-3.11 ± 0.69	-2.74
rKv2.1+ AMIGO1–YFP	-32.8 ± 2.0 [X]	-29.0	2.43 ± 0.15 [Z]	20			

1098 *Table 2. Boltzmann parameters and ΔG calculations for voltage sensor movement.*

1099 Average $V_{g,Mid}$ and z_g values were derived from 1st order Boltzmann fits of *n* individual cells. All values are given ±
1100 SEM. $V_{g,Mid}$, is calculated under the assumption that all voltage sensors activate in a two-state process and represents
1101 the voltage at which half of the total voltage sensors are fully activated. $V_{g,Med}$, represents the voltage at which half
1102 of the total voltage sensors are fully activated, but makes no assumptions about the number of conformational
1103 change that underly the process of voltage sensor activation. Corresponding p–values for comparisons are as
1104 follows: $Q_{ON,fast}$: ST: 0.00093. UV: 0.00084. OFF Gating currents: WX: 7.82×10^{-5}. YZ: 0.038. $V_{g,Med}$ was derived
1105 from median analysis fitting of the average *Q–V* relation. Δ*G* was tabulated using Eqn. E or Eqn. J as listed. * = the
1106 theoretical minimum amount of charge movement, 12.5 e_0, required for channel activation was used in these
1107 calculations. ° = $V_{g,Med}$ was used in this calculation.
1108

AMIGO1 accelerates voltage-stimulated GxTX–594 dissociation

To further test the hypothesis that AMIGO1 specifically destabilizes the earliest resting conformation of Kv2.1 voltage sensors, we probed the stability of this conformation with GxTX–594. The earliest resting conformation is stabilized by GxTX (Tilley et al., 2019) and when occupancy of this conformation is decreased by voltage activation, the rate of GxTX–594 dissociation accelerates (Thapa et al., 2021). Destabilization of the earliest resting conformation by AMIGO1 is expected to increase the rate of GxTX–594 dissociation when voltage sensors are partially activated. To test this prediction, we measured the rate of GxTX–594 dissociation at +30 mV, a potential at which about 20% of gating charge is activated with GxTX bound (Tilley et al., 2019) (Fig. 8A, B, C, D). The rate of GxTX–594 dissociation from Kv2.1 ($k_{\Delta F}$) accelerated from 0.073 ± 0.010 s^{-1} (SEM) in control cells to 0.115 ± 0.015 s^{-1} (SEM) in cells positive for AMIGO1–YFP fluorescence (Fig. 8E, F). As we see no evidence that AMIGO1 alters GxTX–594 affinity or binding in cells at rest (Supplemental Fig. 3, Fig. 9), this 1.6-fold acceleration of $k_{\Delta F}$ is consistent with AMIGO1 destabilizing the earliest resting conformation of voltage sensors. The thermodynamic model developed to interpret the $k_{\Delta F}$ of GxTX–594 dissociation (Thapa et al., 2021) estimates that AMIGO1 decreases the stability of the earliest resting conformation of each voltage sensor by 1.9-fold or a ΔG_{AMIGO1} of -1.5 kcal/mol for Kv2.1 tetramers (Eqn. L). This result suggests that AMIGO1 destabilizes the resting voltage sensor conformation to speed up voltage sensor activation and shift conductance to lower voltages.

Figure 8. AMIGO1 accelerates voltage-stimulated GxTX-594 dissociation.

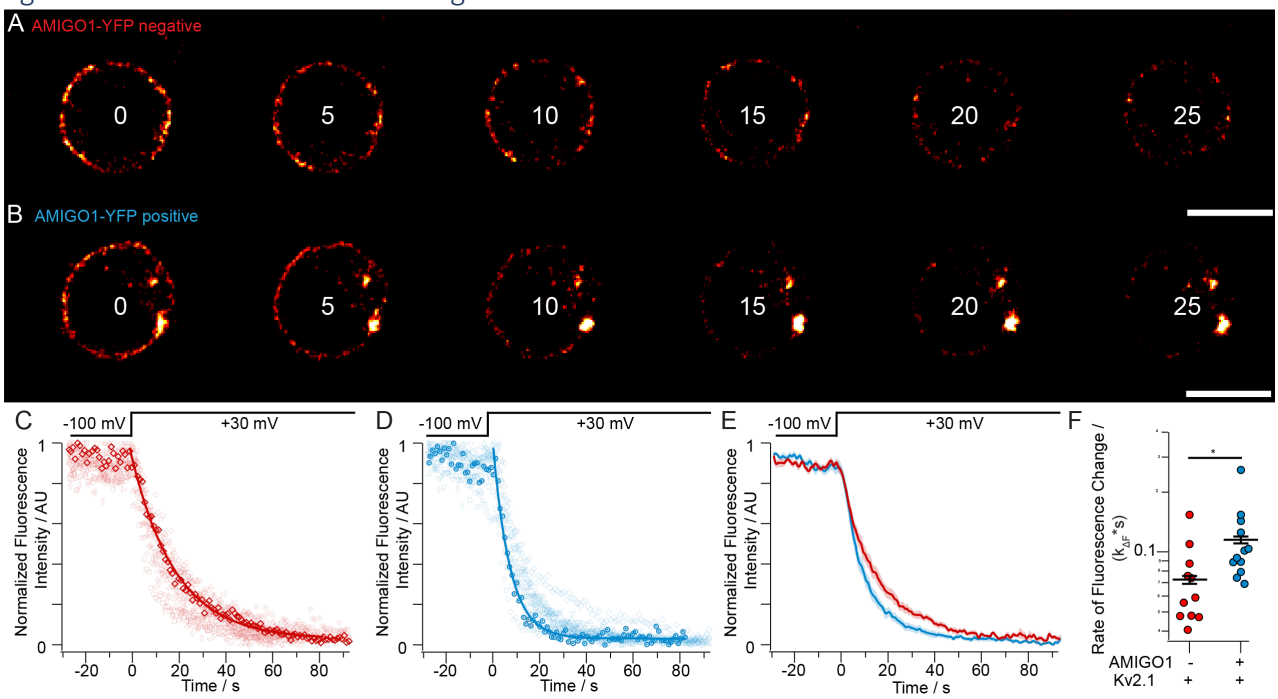

Figure 8. AMIGO1 accelerates voltage-stimulated GxTX-594 dissociation.

(**A, B**) Airyscan images of the solution-exposed membrane of Kv2.1–CHO cells concurrently transfected with AMIGO1–YFP and induced for 48 hours prior to GxTX–594 treatment and imaging. Cells were held -100 mV for 30 seconds before being stimulated to +30 mV (Time = 0 s) to trigger GxTX–594 dissociation. (A and B) showcase fluorescence intensities of two exemplar cells for the first 25 seconds following voltage stimuli. The time point of each image is listed. The scale bar represents 10 μm. (**C, D**) Normalized fluorescence intensity decay plots for Kv2.1–CHO cells without (C) AMIGO1–YFP fluorescence (n = 11) and with (D) AMIGO1-YFP fluorescence (n = 11). The bolded traces correspond to exemplar cells in (A) and (B). The solid line represents the monoexponential fit of fluorescence decay and was used to derive the τ. (**E**) Averaged fluorescence intensity decay for AMIGO1–YFP negative (red), and AMIGO1–YFP positive (blue) cells. Standard error is displayed. (**F**) Rates of fluorescence change ($k_{\Delta F}$) were calculated as $1/\tau$. (Statistics) The unpaired, two-tailed, T–test p-value comparing Kv2.1 control cells and Kv2.1 + AMIGO1 cells was $p = 0.03$. *: $p = \leq 0.05$.

Evidence against an extracellular surface potential mechanism of AMIGO1

We next aimed to differentiate between mechanisms through which AMIGO1 could change voltage sensor action. The destabilization of the early resting conformation could be allosteric or from a change in the electrostatic environment surrounding Kv2.1's gating charges. Per surface charge theory, local extracellular negative charges could attract positive gating charges to activate channels (Chandler et al., 1965; Gilly & Armstrong, 1982; Hille, 2001; Park et al., 2003). AMIGO1 possesses five extracellular glycosylation sites (Kajander et al., 2011), each potentially decorated with negatively-charged sugar moieties (Bishop et al., 2018). AMIGO1 also has a conserved negatively charged residue predicted to localize near the extracellular side of the membrane (Kajander et al., 2011; Kuja-Panula et al., 2003). Similar structural characteristics are found in the Nav β1 auxiliary subunit which, like AMIGO1, is a glycosylated, single transmembrane pass protein with an immunoglobulin-domain. Nav β1 has been proposed to interact with Nav1.4 α subunit through surface charge effects (Ednie & Bennett, 2012; Ferrera & Moran, 2006; D. Johnson et al., 2004). We tested if AMIGO1 likewise affects Kv2.1 activation through electrostatic surface charge interactions.

To measure the electrostatics of the environment immediately surrounding the Kv2.1 voltage sensor domain complex with and without AMIGO1, we employed far-red polarity-sensitive fluorescence (Cohen et al., 2005). The polarity-sensitive fluorophore, JP, was localized to the Kv2.1 voltage sensor by conjugating GxTX to JP at either residue Ser13 or Lys27 (Fletcher-Taylor et al., 2020). When GxTX binds to the S3-S4 extracellular region of the Kv2.1 channel (Gupta et al., 2015), Ser13 and Lys27 occupy positions of distinct polarity. At resting membrane potentials, GxTX Ser13Pra(JP) has an emission maximum of 644 nm, consistent with the homology-based prediction that Ser13 of GxTX localizes in an aqueous environment branched away from S4. Conversely, GxTX Lys27Pra(JP) has an emission maximum of 617 nm, consistent with the prediction that Lys27 sits in the polar region of the membrane adjacent to S4 (Fletcher-Taylor et al., 2020). If AMIGO1 were to alter the resting conformation of the Kv2.1 voltage sensor domain, we would expect either of these environmental point detectors, GxTX Ser13Pra(JP) or GxTX Lys27Pra(JP), to exhibit an altered emission maximum.

Full emission spectra of JP fluorescence from Kv2.1–CHO cells transfected with AMIGO1–YFP and treated with GxTX Ser13Pra(JP) or GxTX Lys27Pra(JP) were fitted with 2-component split pseudo-Voigt functions (Fig. 9C, F). Fitting shows emission peaks, 644 nm and 617 nm, respectively, are unchanged with or without AMIGO1–YFP, consistent with the local electrostatic environment surrounding the JP probes positioned on resting Kv2.1 voltage sensors not being altered by AMIGO1 expression. Previous work has shown that GxTX Lys27Pra(JP) emission peak wavelength is sensitive to conformational changes among early resting states of voltage sensors (Fletcher-Taylor et al., 2020). The absence of any AMIGO1-induced change in environment for either of these GxTX sidechains suggests that AMIGO1 does not cause significant changes to the local environment of the GxTX binding site on the S3b segment of Kv2.1, nor the GxTX position in the membrane when bound to the channel. These results indicate that any destabilization of the GxTX binding site by AMIGO1 is indirect, as the binding site itself appears to retain the same conformation and local environment in the presence of AMIGO1.

Figure 9. AMIGO1 does not alter the Kv2-1-GxTX interface on resting voltage sensors.

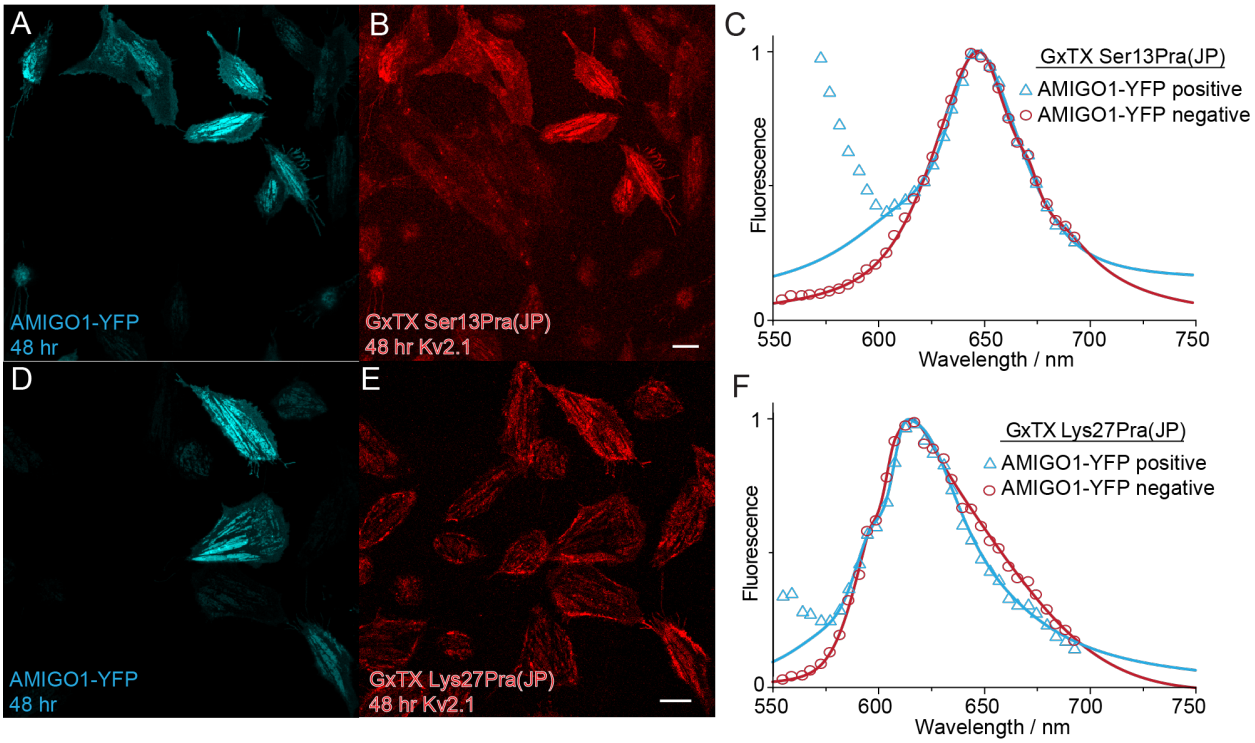

Figure 9. AMIGO1 does not alter the Kv2-1-GxTX interface on resting voltage sensors.

(**A,D**) Confocal image of AMIGO1–YFP fluorescence (blue) in Kv2.1–CHO cells concurrently transfected with AMIGO1–YFP and induced for Kv2.1 expression. (**B,E**) Cells were treated with GxTX Ser13Pra(JP) (B) or GxTX Lys27Pra(JP) (E) for five minutes before lambda imaging with 543 nm excitation. (**C,F**) Fitted emission spectra of GxTX Ser13Pra(JP) (B) and GxTX Lys27Pra(JP) (E) from Kv2.1–CHO cells positive (blue) and negative (red) for AMIGO1–YFP fluorescence. Data points for all spectra are the mean of normalized emission from 72 and 69 cells respectively. All spectra were fit with two–component split pseudo–Voigt functions with shape parameters and root–mean–squared values found in Supplemental Table 1. Fittings for spectra without AMIGO1–YFP included all data points as shown. Fittings for spectra with AMIGO1–YFP included emission data points starting at 613 nm and greater for GxTX Ser13Pra(JP) (B) and 582 nm and greater for GxTX Lys27Pra(JP) (E).

We also tested the whether AMIGO1 acts by a surface charge mechanism by a classical charge screening approach. Surface charge interactions can be revealed by increasing the concentration of Mg^{2+} to screen, or minimize, the impact of fixed negative charges near the voltage sensors (Elinder & Århem, 2003; Green & Andersen, 1991; Hille, 2001). If AMIGO1 alters surface potential, we would expect elevated Mg^{2+} to shrink $\Delta V_{i,Mid}$.

To determine whether surface charge screening suppresses the AMIGO1 effect, voltage clamp experiments were conducted as in Fig. 4, except external recording solutions contained 100 mM Mg^{2+} (Fig. 10A, B, C). Kv2.1 requires more positive voltage steps to activate in high Mg^{2+} solutions (Table 2) (Broomand et al., 2007). AMIGO1 effected a $\Delta V_{i,Mid}$ of -7.42 ± 2.41 mV (SEM) (Fig. 10H) but did not change z_i (Fig. 10G) (Table 1) . When compared to low Mg^{2+} conditions by Ordinary 2-way ANOVA, $\Delta V_{i,Mid}$ was not significantly different in normal versus 100 mM Mg^{2+} (interaction of $p = 0.33$). This result is inconsistent with AMIGO1 altering Kv2.1 activation by a surface charge mechanism and when combined with results from the environmentally sensitive imaging experiments, we find no evidence that AMIGO1's influence on Kv2.1 is mediated by extracellular electrostatic effects.

1211 Figure 10. Surface charge screening does not suppress the AMIGO1 effect.

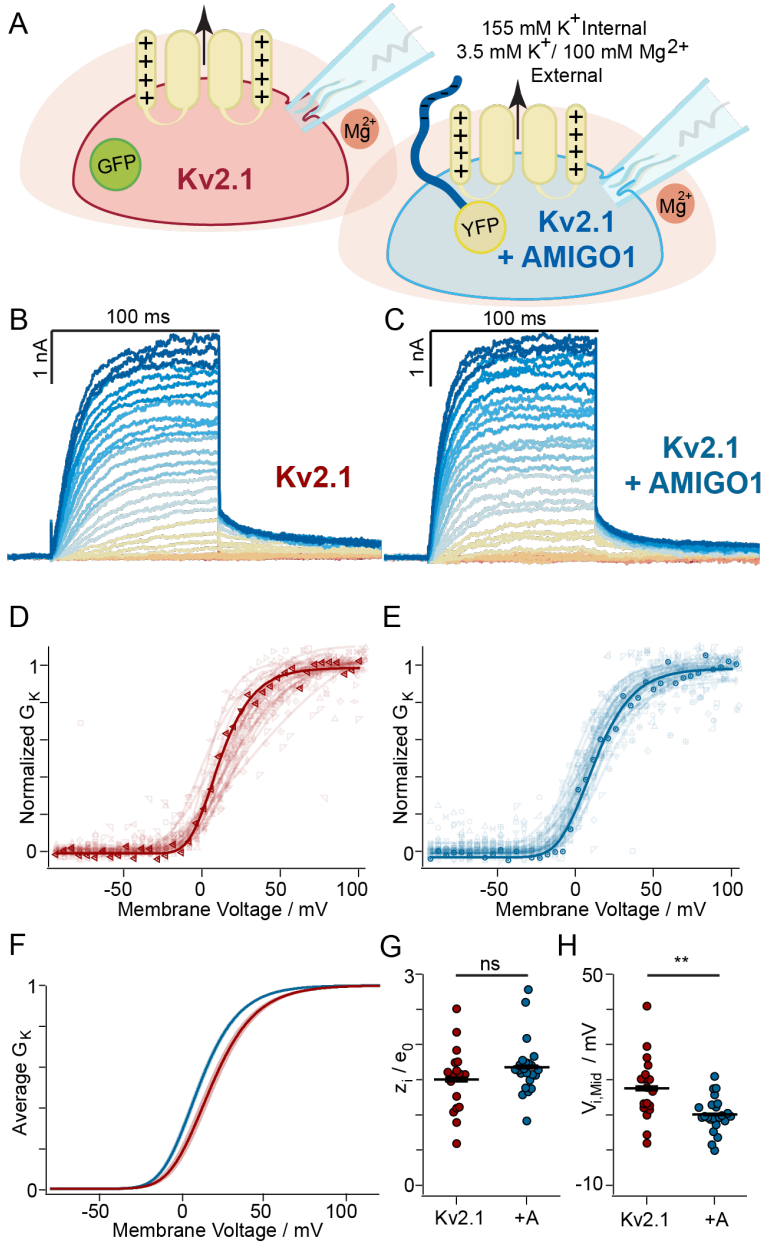

1212

1213 *Figure 10. Surface charge screening does not suppress the AMIGO1 effect.*

1214 **(A)** Experimental set up: Kv2.1-CHO cells were transfected 48 hours prior to whole-cell recording with either GFP
1215 (red) or AMIGO1-YFP (blue). Kv2.1 expression was induced by incubation with minocycline for 1-2 hours prior to
1216 recording. Macroscopic K^+ ionic current was recorded (black arrow). 100 mM magnesium was used to shield
1217 surface charges (peach halo). (**B, C**) Representative Kv2.1 current response elicited from a Kv2.1 control (10.0 pF)
1218 or Kv2.1 + AMIGO1 (6.3 pF) cell. Cells were given 100 ms voltage steps ranging from -80 mV (dark red trace) to
1219 +120 mV (dark blue trace) and then stepped to 0 mV to record tail currents. The holding potential was -100 mV. (**D,**
1220 **E respectively**) Normalized *G-V* relationships for Kv2.1 control or Kv2.1 + AMIGO1 cells. Different symbols
1221 correspond to individual cells and the bolded trace corresponds to the *G–V* derived from the exemplar cell shown in
1222 panels B, C respectively. Solid lines represent 4th order Boltzmann relationships (Eqn. C). (**F**) Reconstructed 4th
1223 order Boltzmann fits using the average $V_{i,Mid}$ and the average z_i (Table 1). Shaded areas represent $V_{i,Mid}$ ± SEM. (**G**)
1224 Steepness and (**H**) midpoint of 4th order Boltzmann fits. Bars are mean ± SEM. Unpaired, two-tailed T–tests p-
1225 values are in Table 1. **: $p = \leq 0.01$, ns: not significant.

Discussion

We asked whether AMIGO1 modulates the threshold for activation of Kv2.1 conductance by way of modulating conformational changes associated with either pore opening or voltage sensor activation. We found that AMIGO1 destabilizes the resting, inward conformation of Kv2.1 voltage sensors, causing channels to activate at more negative voltages. This conclusion is supported by three major results:

1) AMIGO1 destabilizes the earliest resting conformation of Kv2.1 voltage sensors.

Activation kinetics measurements from macroscopic currents revealed that AMIGO1 expression accelerated activation but only at the subset of voltages influenced by voltage sensor dynamics and not those limited by a slow pore opening step (Fig. 4). When voltage sensor movements were measured directly, gating current recordings revealed an increase in the forward rate constant of gating charge activation in cells with AMIGO1. Between 0 and 120 mV, pore opening is 10-30x slower than $I_{g,ON}$ decay (Fig. 4, 7), too slow to influence voltage sensor movement captured by these measurements. $Q_{ON,fast}$ is shifted to more negative voltages with AMIGO1, indicating that the earliest resting conformation is destabilized relative to more activated conformations. When estimates of the amount of energy AMIGO1 contributes to modulating Kv2.1 conformational bias were compared, we found that ΔG_{AMIGO1} was more extreme when calculated for voltage sensor movements (Table 2) as opposed to conductance changes (Table 1). When the entirety of the Kv2.1 charge movement was considered, as measured in the Q_{OFF}–V relation, ΔG_{AMIGO1} was ~3 kcal/mol. This value was consistent when calculated using three distinct methods, Eqn. E, Eqn. J*, and Eqn J*°. We also calculated that AMIGO1 imparted -1.3 kcal/mol (Eqn. I) to $\Delta G^{\ddagger}_{AMIGO1}$, which describes the rate of conformational change between the resting and transitional state. We captured this measurement from the change in the forward rate $\tau_{0mV,\alpha}$ measured from ON gating current decays (Fig. 7). From these results we can conclude that AMIGO1 destabilizes the fully resting conformation of Kv2.1 channels by ~3 kcal/mol, relative to the fully active open state, and that about half of this energy lowers the barrier for the initial exit of voltage sensors from their resting conformation (Fig. 11).

2) AMIGO1 opposes the action of a toxin which stabilizes resting voltage sensors

GxTX and its GxTX–594 analog detain Kv2.1 voltage sensors in their earliest resting conformation (Tilley et al., 2019; Thapa et al., 2021). In the presence of GxTX–594, the AMIGO1 G–V shift widens to -22.3 ± 4.8 (SEM) from -5.74 ± 2.15 mV (SEM) without GxTX–594 (Fig. 4, 6) and ΔG_{AMIGO1} is increased (Table 1), consistent with AMIGO1 liberating voltage sensors from detention in their earliest resting conformation. The enhancement of GxTX–594 dissociation at +30 mV by AMIGO1 is consistent with enhancement of voltage sensor activation by AMIGO1 (Fig. 8). All GxTX–594 evidence supports the hypothesis that AMIGO1 destabilizes the earliest resting conformation of voltage sensors, allosterically opposing the detention of voltage sensors at rest by GxTX–594.

3) AMIGO1 has a greater impact on the voltage sensors than the pore opening.

Free energy estimates indicate more AMIGO1 perturbation of the Q–V measurements than the G–V. The ΔG for AMIGO1's impact on voltage sensor activation ranged from -1.92 kcal/mol to -3.11 kcal/mol depending on the calculation method (Table 2). Yet, the ΔG_{AMIGO1} calculated for

ionic conductance was only -0.21 to -0.37 kcal/mol (Table 1). This lesser impact on pore opening is consistent with a direct impact of AMIGO1 on voltage sensor movements which are coupled to pore opening. When we looked at pore opening directly, we saw no evidence suggesting a direct effect of AMIGO1. We saw no change in the slope of the *G–V* relationship with AMIGO1 (Fig. 1, 4, 6, 10), nor sigmoidicity (Fig. 4), nor single channel measurements (Fig. 5). While such negative results cannot eliminate the possibility that AMIGO1 has a small direct effect on pore opening, these negative results constrain the effect size of AMIGO1 on pore opening equilibria or voltage sensor–pore coupling to be smaller than the error associated with our measurements.

1279 Figure 11. AMIGO1 destabilizes the resting conformation of Kv2.1 voltage sensors.

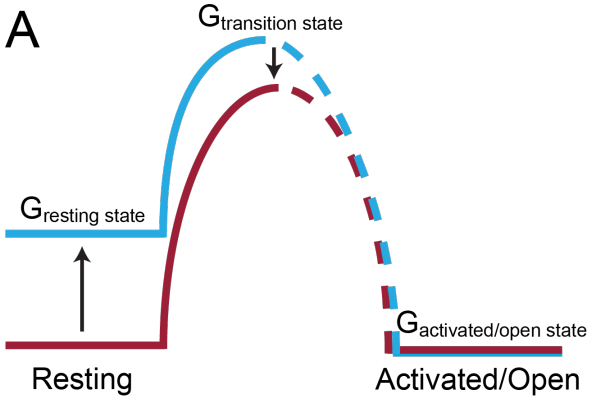

$\Delta G^{\ddagger}_{kinetics} = G_{transition\ state} - G_{resting\ state}$

$\Delta G^{\ddagger}_{kinetics,\ AMIGO1\text{-}control} = -1\ kcal/mol$

$\Delta G_{Q_{OFF}} = G_{activated/open\ state} - G_{resting\ state}$

$\Delta G_{Q_{OFF},\ AMIGO1\text{-}control} = -3\ kcal/mol$

1280

1281 *Figure 11. AMIGO1 destabilizes the resting conformation of Kv2.1 voltage sensors.*

1282 AMIGO1 destabilizes the resting state conformation of Kv2.1 voltage sensors. AMIGO1 also lowers the activation
1283 energy barrier needed for Kv2.1 activation.

Limitations

More detailed investigation of the AMIGO1 impact on the Kv2.1 activation pathway was limited by the relatively small magnitude of AMIGO1-dependent effects versus the cell–to–cell variability, with $\Delta V_{i,Mid}$ of 5 to 7 mV, and standard deviations for $V_{i,Mid}$ of 4 to 9 mV (Table 1, excluding GxTX–594). This degree of cell-to-cell variability does not appear to be unique to our laboratory. Midpoints reported for rat Kv2.1 activation in HEK293 cells span a 36 mV range, from -20.2 mV to 16.4 mV (Aréchiga-Figueroa et al., 2015, 2017; David et al., 2015; Delgado-Ramírez et al., 2018; Kirmiz et al., 2018a; Li et al., 2015; Liu et al., 2016; Liu et al., 2017; Maverick et al., 2021; Milescu et al., 2009; O'Connell et al., 2010; Park et al., 2006; Peltola et al., 2011). When we calculated V_{Mid} standard deviation values from the standard errors and n-values in these studies, standard deviations ranged from 1 to 17 mV, a range consistent with our standard deviations. We suspect these notable V_{Mid} deviations result from the many different types of regulation to which Kv2.1 channels are susceptible (MacDonald et al., 2003; Murakoshi et al., 1997; Plant et al., 2011; Ramu et al., 2006). Means to constrain the cell-to-cell variability in Kv2.1 function could allow more precise mechanistic studies of AMIGO1 modulation.

Inconsistent action by auxiliary subunit(s) on a pore forming subunit counterpart is also a common problem, requiring controls to asses interaction (Jain et al., 2001; Laedermann et al., 2013; Meadows & Isom, 2005; Moran et al., 2000, 2003; Ponce et al., 2018). Variability in channel-auxiliary subunit complexes can be due to inconsistent assembly. While some channel-auxiliary subunit complexes coassemble after translocation to the plasma membrane (Froehner et al., 1990), others must coassemble at earlier stages (Eichel et al., 2019; Nagaya & Papazian, 1997; Schmidt & Catterall, 1986; Yan & Aldrich, 2012). Further, abrogated or uncoupled channel-auxiliary subunit trafficking can alter the glycosylation state of the auxiliary subunit and further alter ion channel activity from conditions where trafficking is coupled (Bishop et al., 2018; Vagin et al., 2009). As auxiliary subunits can have dose-dependent effects (Gonzalez-Perez et al., 2014, 2018; Trapani & Korn, 2003; Wang et al., 2002), the method for coassembly could contribute to variations in biochemical modification and auxiliary subunit function. While our colocalization and reorganization assays offer evidence of AMIGO1 and Kv2.1 coassembly, our approach may not have achieved homogenous coassembly or a uniform state of biochemical modification. We have not eliminated the possibility that apparent excesses of AMIGO1 proteins are unable to assemble with Kv2.1. If AMIGO1 coassembly is heterogenous, one might expect increased cell-to-cell variability with AMIGO1. However, in CHO cells, the cell-to-cell variability and slopes of Boltzmann fits are similar between AMIGO1 and control cells. Although the most parsimonious explanation for the effect AMIGO1 has on the Kv2.1 conduction–voltage relation is a direct interaction with Kv2.1 voltage sensors, we have not eliminated the possibility that unassociated AMIGO1 proteins could change cellular regulation of Kv2.1. It is possible that AMIGO1 could destabilize resting voltage sensors not by physically interacting with them, but through a mechanism involving intermediary molecules. Even if AMIGO1 acts by an indirect mechanism, our mechanistic conclusions remain valid, as they are not predicated on a direct protein–protein interaction between AMIGO1 and Kv2.1.

Conclusions

In order to shift the threshold for the activation of Kv2.1 conductance to lower voltages, AMIGO1 destabilizes the earliest resting conformations of Kv2.1 voltage sensors relative to more activated conformations. While we cannot completely rule out a direct influence on pore dynamics, we saw no indication of such. Thus, we propose that AMIGO1 shifts the voltage–

dependence of Kv2.1 conduction to more negative voltages by modulating early voltage sensor movements.

The impact of AMIGO1 on Kv2.1 voltage sensors suggests that all voltage-dependent functions are modulated by AMIGO1. In addition to electrical signaling, Kv2 proteins have important nonconducting functions (Bishop et al., 2018; Fox et al., 2013; Johnson et al., 2018; Kirmiz et al., 2018a; Kirmiz et al., 2018b; Vierra et al., 2019). As AMIGO1 is colocalized with all Kv2 proteins in many, if not all, mammalian brain neurons (Bishop et al., 2018; Mandikian et al., 2014; Peltola et al., 2011), our results suggest that AMIGO1 acts as a functional unit of the Kv2.1 voltage sensing domain and causes all voltage–dependent functions of Kv2-containing proteins to occur at more negative potentials in many neurons throughout the brain.

Acknowledgements

We thank Vladimir Yarov-Yarovoy, James Trimmer, Karen Zito, and Tsung-Yu Chen of University of California Davis for constructive feedback integral to design and synthesis of experimental ideas. The authors would like to thank the UC Davis statisticians Dr. Sandra Taylor and Dr. Susan Stewart and as well as Karl Brown for their consultation on statistical approaches.

This research was funded by National Institutes of Health grants R01NS096317 (JTS), R21EY026449 (JTS), T32GM007377 (RJS), and F31NS108614 (RJS). The GxTX-Ser13Cys peptide was synthesized at the Molecular Foundry of the Lawrence Berkeley National Laboratory under U.S. Department of Energy contract DE-AC02-05CH11231. The authors declare no competing financial interests.

Author Contributions

Rebecka J. Sepela
Conceptualization, Data curation, Formal analysis, Funding acquisition, Investigation, Methodology, Project administration, Visualization, Writing – original draft, Writing – review and editing

Robert G. Stewart
Formal analysis, Investigation, Visualization

Luis A. Valencia
Formal analysis, Visualization

Parashar Thapa
Resources

Zeming Wang
Resources

Bruce E. Cohen
Conceptualization, Project administration, Writing – review and editing

Jon T. Sack
Conceptualization, Data curation, Funding acquisition, Methodology, Project administration, Supervision, Writing – original draft, Writing – review and editing

Competing Interests

We declare no competing interests.

References

Aras, M. A., Saadi, R. A., & Aizenman, E. 2009. Zn^{2+} regulates Kv2.1 voltage-dependent gating and localization following ischemia. *Eur J Neurosci*, **30**(12): 2250–2257. https://doi.org/10.1111/j.1460-9568.2009.07026.x

Aréchiga-Figueroa, I. A., Delgado-Ramírez, M., Morán-Zendejas, R., & Rodríguez-Menchaca, A. A. 2015. Modulation of Kv2.1 channels inactivation by curcumin. *Pharmacol Rep*, **67**(6): 1273–1279. https://doi.org/10.1016/j.pharep.2015.05.019

Aréchiga-Figueroa, I. A., Morán-Zendejas, R., Delgado-Ramírez, M., & Rodríguez-Menchaca, A. A. 2017. Phytochemicals genistein and capsaicin modulate Kv2.1 channel gating. *Pharmacol Rep*, **69**(6): 1145–1153. https://doi.org/10.1016/j.pharep.2017.05.018

Armstrong, C. M., & Bezanilla, F. 1974. Charge movement associated with the opening and closing of the activation-gates of the Na channels. *J Gen Physiol*, **63**: 533–552. https://doi.org/10.1085/jgp.63.5.533

Bar, C., Kuchenbuch, M., Barcia, G., Schneider, A., Jennesson, M., Le Guyader, G., Lesca, G., Mignot, C., Montomoli, M., Parrini, E., Isnard, H., Rolland, A., Keren, B., Afenjar, A., Dorison, N., Sadleir, L. G., Breuillard, D., Levy, R., Rio, M., … Nabbout, R. 2020. Developmental and epilepsy spectrum of KCNB1 encephalopathy with long-term outcome. *Epilepsia*, **61**(11): 2461–2473. https://doi.org/https://doi.org/10.1111/epi.16679

Barro-Soria, R., Perez, M. E., & Larsson, H. P. 2015. KCNE3 acts by promoting voltage sensor activation in KCNQ1. *Proc Natl Acad Sci U S A*, **112**(52): E7286–E7292. https://doi.org/10.1073/pnas.1516238112

Barro-Soria, R., Ramentol, R., Liin, S. I., Perez, M. E., Kass, R. S., & Larsson, H. P. 2017. KCNE1 and KCNE3 modulate KCNQ1 channels by affecting different gating transitions. *Proc Natl Acad Sci U S A*, **114**(35): E7367–E7376. https://doi.org/10.1073/pnas.1710335114

Barro-Soria, R., Rebolledo, S., Liin, S. I., Perez, M. E., Sampson, K. J., Kass, R. S., & Larsson, H. P. 2014. KCNE1 divides the voltage sensor movement in KCNQ1/KCNE1 channels into two steps. *Nat Commun*, **5**(3750): 1-12. https://doi.org/10.1038/ncomms4750

Baver, S. B., & O'Connell, K. M. S. 2012. The C-terminus of neuronal Kv2.1 channels is required for channel localization and targeting but not for NMDA-receptor-mediated regulation of channel function. *Neuroscience*, **217**: 56–66. https://doi.org/10.1016/j.neuroscience.2012.04.054

Bezanilla, F., Perozo, E., & Stefani, E. 1994. Gating of Shaker K^+ channels: II. The components of gating currents and a model of channel activation. *Biophys J*, **66**(4): 1011–1021. https://doi.org/10.1016/S0006-3495(94)80882-3

Bishop, H. I., Cobb, M. M., Kirmiz, M., Parajuli, L. K., Mandikian, D., Philp, A. M., Melnik, M., Kuja-Panula, J., Rauvala, H., Shigemoto, R., Murray, K. D., & Trimmer, J. S. 2018. Kv2 ion channels determine the expression and localization of the associated AMIGO-1 cell adhesion molecule in adult brain neurons. *Front Mol Neurosci*, **11**(1): 1-20. https://doi.org/10.3389/fnmol.2018.00001

Bishop, H. I., Guan, D., Bocksteins, E., Parajuli, L. K., Murray, K. D., Cobb, M. M., Misonou, H., Zito, K., Foehring, R. C., & Trimmer, J. S. 2015. Distinct cell- and layer-specific expression patterns and independent regulation of Kv2 channel subtypes in cortical pyramidal neurons. *J Neurosci*, **35**(44): 14922–14942.

https://doi.org/10.1523/JNEUROSCI.1897-15.2015

Bocksteins, E. 2016. Kv5, Kv6, Kv8, and Kv9 subunits: No simple silent bystanders. *J Gen Physiol*, **147**(2): 105–125. https://doi.org/10.1085/jgp.201511507

Brackenbury, W. J., & Isom, L. L. 2011. Na^+ channel β subunits: Overachievers of the ion channel family. *Front Pharmacol*, **2**(53): 1–11. https://doi.org/10.3389/fphar.2011.00053

Broomand, A., Österberg, F., Wardi, T., & Elinder, F. 2007. Electrostatic domino effect in the Shaker K channel turret. *Biophys J*, **93**(7): 2307–2314. https://doi.org/10.1529/biophysj.107.104349

Cerda, O., & Trimmer, J. S. 2011. Activity-dependent phosphorylation of neuronal Kv2.1 potassium channels by CDK5. *J Biol Chem*, **286(**33): 28738–28748. https://doi.org/10.1074/jbc.M111.251942

Chandler, W. K., Hodgkin, A. L., & Meves, H. 1965. The effect of changing the internal solution on sodium inactivation and related phenomena in giant axons. *J Physiol*, **180**(4): 821–836. https://doi.org/10.1113/jphysiol.1965.sp007733

Chen, Y., Aulia, S., Li, L., & Tang, B. L. 2006. AMIGO and friends: An emerging family of brain-enriched, neuronal growth modulating, type I transmembrane proteins with leucine-rich repeats (LRR) and cell adhesion molecule motifs. *Brain Res Rev*, **51**(2): 265–274. https://doi.org/10.1016/j.brainresrev.2005.11.005

Chen, Y., Hor, H. H., & Tang, B. L. 2012. AMIGO is expressed in multiple brain cell types and may regulate dendritic growth and neuronal survival. *J Cell Physiol*, **227**(5): 2217–2229. https://doi.org/10.1002/jcp.22958

Chowdhury, S., & Chanda, B. 2012. Estimating the voltage-dependent free energy change of ion channels using the median voltage for activation. *J Gen Physiol*, **139**(1): 3–17. https://doi.org/10.1085/jgp.201110722

Cobb, M. M., Austin, D. C., Sack, J. T., & Trimmer, J. S. 2016. Cell cycle-dependent changes in localization and phosphorylation of the plasma membrane Kv2.1 K^+ channel impact endoplasmic reticulum membrane contact sites in COS-1 cells. *J Biol Chem*, **291**(11): 5527. https://doi.org/10.1074/jbc.A115.690198

Cohen, B. E., Pralle, A., Yao, X., Swaminath, G., Gandhi, C. S., Jan, Y. N., Kobilka, B. K., Isacoff, E. Y., & Jan, L. Y. 2005. A fluorescent probe designed for studying protein conformational change. *Proc Natl Acad Sci U S A*, *102*(4), 965–970. https://doi.org/10.1073/pnas.0409469102

Consiglio, J. F., & Korn, S. J. 2004. Influence of permeant ions on voltage sensor function in the Kv2.1 potassium channel. *J Gen Physiol*, **123**(4): 387–400. https://doi.org/10.1085/jgp.200308976

Costes, S. V., Daelemans, D., Cho, E. H., Dobbin, Z., Pavlakis, G., & Lockett, S. 2004. Automatic and quantitative measurement of protein-protein colocalization in live cells. *Biophys J*, **86(**6): 3993–4003. https://doi.org/10.1529/biophysj.103.038422

Das, S., Gilchrist, J., Bosmans, F., & Van Petegem, F. 2016. Binary architecture of the Nav1.2-β2 signaling complex. *Elife*, **5**(e10960): 1-21. https://doi.org/10.7554/eLife.10960

David, J.-P., Stas, J. I., Schmitt, N., & Bocksteins, E. 2015. Auxiliary KCNE subunits modulate both homotetrameric Kv2.1 and heterotetrameric Kv2.1/Kv6.4 channels. *Sci Rep*, **5**(1): 12813. https://doi.org/10.1038/srep12813

Delgado-Ramírez, M., De Jesús-Pérez, J. J., Aréchiga-Figueroa, I. A., Arreola, J., Adney, S. K., Villalba-Galea, C. A., Logothetis, D. E., & Rodríguez-Menchaca, A. A. 2018. Regulation of Kv2.1 channel inactivation by phosphatidylinositol 4,5-bisphosphate. *Sci Rep*, **8**(1): 1769.

https://doi.org/10.1038/s41598-018-20280-w

Du, J., Haak, L. L., Phillips-Tansey, E., Russell, J. T., & McBain, C. J. 2000. Frequency-dependent regulation of rat hippocampal somato-dendritic excitability by the K^+ channel subunit Kv2.1. *J Physiol*, **522 Pt 1**(1): 19–31. https://doi.org/10.1111/j.1469-7793.2000.t01-2-00019.xm

Dudem, S., Large, R. J., Kulkarni, S., McClafferty, H., Tikhonova, I. G., Sergeant, G. P., Thornbury, K. D., Shipston, M. J., Perrino, B. A., & Hollywood, M. A. 2020. LINGO1 is a regulatory subunit of large conductance, Ca^{2+}-activated potassium channels. *Proc Natl Acad Sci U S A*, **117**(4): 2194–2200. https://doi.org/10.1073/pnas.1916715117

Dunn, K. W., Kamocka, M. M., & McDonald, J. H. 2011. A practical guide to evaluating colocalization in biological microscopy. *Am J Physiol Cell Physiol*, **300**(4): C723-742. https://doi.org/10.1152/ajpcell.00462.2010

Eaholtz, G., Scheuer, T., & Catterall, W. A. 1994. Restoration of inactivation and block of open sodium channels by an inactivation gate peptide. *Neuron*, **12**(5): 1041–1048. https://doi.org/10.1016/0896-6273(94)90312-3

Ednie, A. R., & Bennett, E. S. 2012. Modulation of voltage-gated ion channels by sialylation. *Compr Physiol*, **2**(2): 1269–1301. https://doi.org/doi:10.1002/cphy.c110044

Eichel, C. A., Ríos-Pérez, E. B., Liu, F., Jameson, M. B., Jones, D. K., Knickelbine, J. J., & Robertson, G. A. 2019. A microtranslatome coordinately regulates sodium and potassium currents in the human heart. *Elife*, **8**(e52654): 1-21. https://doi.org/10.7554/eLife.52654

Elinder, F., & Århem, P. 2003. Metal ion effects on ion channel gating. *Quarterly Reviews of Biophysics*, **36**(4): 373–427. https://doi.org/10.1017/s0033583504003932

Ferrera, L., & Moran, O. 2006. β1-subunit modulates the Nav1.4 sodium channel by changing the surface charge. *Exp Brain Res*, **172**(2): 139–150. https://doi.org/10.1007/s00221-005-0323-4

Fletcher-Taylor, S., Thapa, P., Sepela, R. J., Kaakati, R., Yarov-Yarovoy, V., Sack, J. T., & Cohen, B. E. 2020. Distinguishing potassium channel resting state conformations in live cells with environment-sensitive fluorescence. *ACS Chem Neurosci*, **11**(15). https://doi.org/10.1021/acschemneuro.0c00276

Fox, P. D., Loftus, R. J., & Tamkun, M. M. 2013. Regulation of Kv2.1 K(+) conductance by cell surface channel density. *J Neurosci*, **33**(3): 1259–1270. https://doi.org/10.1523/JNEUROSCI.3008-12.2013

Froehner, S. C., Luetje, C. W., Scotland, P. B., & Patrick, J. 1990. The postsynaptic 43K protein clusters muscle nicotinic acetylcholine receptors in Xenopus oocytes. *Neuron*, **5**(4): 403–410. https://doi.org/10.1016/0896-6273(90)90079-u

Gamper, N., Stockand, J. D., & Shapiro, M. S. 2005. The use of Chinese hamster ovary (CHO) cells in the study of ion channels. *J Pharmacol Toxicol Methods*, **51**(3): 177–185. https://doi.org/10.1016/j.vascn.2004.08.008

Gilchrist, J., Das, S., Van Petegem, F., & Bosmans, F. 2013. Crystallographic insights into sodium-channel modulation by the β4 subunit. *Proc Natl Acad Sci U S A*, **110**(51): E5016-E5024. https://doi.org/10.1073/pnas.1314557110

Gilly, W. F., & Armstrong, C. M. 1982. Slowing of sodium channel opening kinetics in squid axon by extracellular zinc. *J Gen Physiol*, **79**(6): 935–964. https://doi.org/10.1085/jgp.79.6.935

Gonzalez-Perez, V., Johny, M. Ben, Xia, X. M., & Lingle, C. J. 2018. Regulatory γ1 subunits defy symmetry in functional modulation of BK channels. *Proc Natl Acad Sci U S A*,

115(40): 9923–9928. https://doi.org/10.1073/pnas.1804560115

Gonzalez-Perez, V., Xia, X.-M., & Lingle, C. J. 2014. Functional regulation of BK potassium channels by γ1 auxiliary subunits. *Proc Natl Acad Sci U S A*, **111**(13): 4868–4873. https://doi.org/10.1073/pnas.1322123111

Green, W. N., & Andersen, O. S. 1991. Surface charges and ion channel function. *Annu Rev Physiol*, **53**(1): 341–359. https://doi.org/10.1146/annurev.ph.53.030191.002013

Gupta, K., Zamanian, M., Bae, C., Milescu, M., Krepkiy, D., Tilley, D. C., Sack, J. T., Yarov-Yarovoy, V., Kim, J. Il, & Swartz, K. J. 2015. Tarantula toxins use common surfaces for interacting with Kv and ASIC ion channels. *Elife*, **4**(e06774): 1–20. https://doi.org/10.7554/eLife.06774

Hille, B. 2001. Ion Channel Excitable Membranes. In *Sunderland Massachusetts USA* (pp. 646–659). https://doi.org/10.1007/3-540-29623-9_5640

Hönigsperger, C., Nigro, M. J., & Storm, J. F. 2017. Physiological roles of Kv2 channels in entorhinal cortex layer II stellate cells revealed by Guangxitoxin-1E. *J Physiol*, **595**(3): 739–757. https://doi.org/10.1113/JP273024

Horrigan, F. T., & Aldrich, R. W. 2002. Coupling between voltage sensor activation, Ca^{2+} binding and channel opening in large conductance (BK) potassium channels. *J Gen Physiol*, **120**(3): 267–305. https://doi.org/10.1085/jgp.20028605

Ikematsu, N., Dallas, M. L., Ross, F. A., Lewis, R. W., Rafferty, J. N., David, J. A., Suman, R., Peers, C., Hardie, D. G., & Evansc, A. M. 2011. Phosphorylation of the voltage-gated potassium channel Kv2.1 by AMP-activated protein kinase regulates membrane excitability. *Proc Natl Acad Sci U S A*, **108**(44): 18132–18137. https://doi.org/10.1073/pnas.1106201108

Islas, L. D., & Sigworth, F. J. 1999. Voltage sensitivity and gating charge in Shaker and Shab family potassium channels. *J Gen Physiol*, **114**(5): 723–742. https://doi.org/10.1085/jgp.114.5.723

Isom, L., De Jongh, K., Patton, D., Reber, B., Offord, J., Charbonneau, H., Walsh, K., Goldin, A., & Catterall, W. 1992. Primary structure and functional expression of the beta 1 subunit of the rat brain sodium channel. *Science*, **256**(5058): 839–842. https://doi.org/10.1126/science.1375395

Isom, L. L., & Catterall, W. A. 1996. Na^+ channel subunits and Ig domains. *Nature*, **383**(6598): 307–308. https://doi.org/10.1038/383307b0

Isom, L. L., Ragsdale, D. S., De Jongh, K. S., Westenbroek, R. E., Reber, B. F. X., Scheuer, T., & Catterall, W. A. 1995. Structure and function of the β2 subunit of brain sodium channels, a transmembrane glycoprotein with a CAM motif. *Cell*, **83**(3): 433–442. https://doi.org/10.1016/0092-8674(95)90121-3

Jain, L., Chen, X.-J. J., Ramosevac, S., Brown, L. A., & Eaton, D. C. 2001. Expression of highly selective sodium channels in alveolar type II cells is determined by culture conditions. *Am J Physiol Lung Cell Mol Physiol*, **280(**4): 646–658. https://doi.org/10.1152/ajplung.2001.280.4.l646

Jara-Oseguera, A., Ishida, I. G., Rangel-Yescas, G. E., Espinosa-Jalapa, N., Pérez-Guzmán, J. A., Elías-Viñas, D., Le Lagadec, R., Rosenbaum, T., & Islas, L. D. 2011. Uncoupling charge movement from channel opening in voltage-gated potassium channels by ruthenium complexes. *J Biol Chem*, **286**(18): 16414–16425. https://doi.org/10.1074/jbc.M110.198010

Jensen, C. S., Watanabe, S., Stas, J. I., Klaphaak, J., Yamane, A., Schmitt, N., Olesen, S.-P., Trimmer, J. S., Rasmussen, H. B., & Misonou, H. 2017. Trafficking of Kv2.1 channels to the axon initial segment by a novel nonconventional secretory pathway. *J Neurosci*, **37**(48):

11523–11536. https://doi.org/10.1523/JNEUROSCI.3510-16.2017

Johnson, B., Leek, A. N., Solé, L., Maverick, E. E., Levine, T. P., & Tamkun, M. M. 2018. Kv2 potassium channels form endoplasmic reticulum/plasma membrane junctions via interaction with VAPA and VAPB. *Proc Natl Acad Sci U S A*, **115**(31): E7331 LP-E7340. https://doi.org/10.1073/pnas.1805757115

Johnson, D., Montpetit, M. L., Stocker, P. J., & Bennett, E. S. 2004. The sialic acid component of the β1 subunit modulates voltage-gated sodium channel function. *J Biol Chem*, **279**(43): 44303–44310. https://doi.org/10.1074/jbc.M408900200

Kajander, T., Kuja-Panula, J., Rauvala, H., & Goldman, A. 2011. Crystal structure and role of glycans and dimerization in folding of neuronal leucine-rich repeat protein AMIGO-1. *J Membr Biol*, **413**(5): 1001–1015. https://doi.org/10.1016/j.jmb.2011.09.032

Kang, S. K., Vanoye, C. G., Misra, S. N., Echevarria, D. M., Calhoun, J. D., O'Connor, J. B., Fabre, K. L., McKnight, D., Demmer, L., Goldenberg, P., Grote, L. E., Thiffault, I., Saunders, C., Strauss, K. A., Torkamani, A., van der Smagt, J., van Gassen, K., Carson, R. P., Diaz, J., … Kearney, J. A. 2019. Spectrum of K(v) 2.1 dysfunction in KCNB1-associated neurodevelopmental disorders. *Ann Neurol*, **86**(6): 899–912. https://doi.org/10.1002/ana.25607

Kazarinova-Noyes, K., Malhotra, J. D., McEwen, D. P., Mattei, L. N., Berglund, E. O., Ranscht, B., Levinson, S. R., Schachner, M., Shrager, P., Isom, L. L., & Xiao, Z. C. 2001. Contactin associates with Na^+ channels and increases their functional expression. *J Neurosci*, **21**(19): 7517–7525. https://doi.org/10.1523/jneurosci.21-19-07517.2001

Kihira, Y., Hermanstyne, T. O., & Misonou, H. 2010. Formation of heteromeric Kv2 channels in mammalian brain neurons. *J Biol Chem*, **285**(20): 15048–15055. https://doi.org/10.1074/jbc.M109.074260

Kimm, T., Khaliq, Z. M., & Bean, B. P. 2015. Differential regulation of action potential shape and burst-frequency firing by BK and Kv2 channels in substantia nigra dopaminergic neurons. *J Neurosci*, **35**(50): 16404–16417. https://doi.org/10.1523/JNEUROSCI.5291-14.2015

Kirmiz, M., Palacio, S., Thapa, P., King, A. N., Sack, J. T., & Trimmer, J. S. 2018. Remodeling neuronal ER–PM junctions is a conserved nonconducting function of Kv2 plasma membrane ion channels. *Mol Biol Cell*, **29**(20): 2410–2432. https://doi.org/10.1091/mbc.E18-05-0337

Kirmiz, M., Vierra, N. C., Palacio, S., & Trimmer, J. S. 2018. Identification of VAPA and VAPB as Kv2 channel-interacting proteins defining endoplasmic reticulum–plasma membrane junctions in mammalian brain neurons. *J Neurosci*, **38**(35): 7562–7584. https://doi.org/10.1523/JNEUROSCI.0893-18.2018

Kuja-Panula, J., Kiiltomäki, M., Yamashiro, T., Rouhiainen, A., & Rauvala, H. 2003. AMIGO, a transmembrane protein implicated in axon tract development, defines a novel protein family with leucine-rich repeats. *J Cell Bio*, **160**(6): 963–973. https://doi.org/10.1083/jcb.200209074

Laedermann, C. J., Syam, N., Pertin, M., Decosterd, I., & Abriel, H. 2013. β1- and β3- voltage-gated sodium channel subunits modulate cell surface expression and glycosylation of Nav1.7 in HEK293 cells. *Front Cell Neurosci*, **7**: 137. https://doi.org/10.3389/fncel.2013.00137

Li, X.-T., Li, X.-Q., Hu, X.-M., & Qiu, X.-Y. 2015. The inhibitory effects of Ca^{2+} channel blocker nifedipine on rat Kv2.1 potassium channels. *PLoS One*, **10**(4): e0124602.

https://doi.org/10.1371/journal.pone.0124602

Lim, S. T., Antonucci, D. E., Scannevin, R. H., & Trimmer, J. S. 2000. A novel targeting signal for proximal clustering of the Kv2.1 K^+ channel in hippocampal neurons. *Neuron*, **25**(2): 385–397. https://doi.org/10.1016/S0896-6273(00)80902-2

Liu, P. W., & Bean, B. P. 2014. Kv2 channel regulation of action potential repolarization and firing patterns in superior cervical ganglion neurons and hippocampal CA1 pyramidal neurons. *J Neurosci*, **34**(14): 4991–5002. https://doi.org/10.1523/JNEUROSCI.1925-13.2014

Liu, R., Yang, G., Zhou, M.-H., He, Y., Mei, Y.-A., & Ding, Y. 2016. Flotillin-1 downregulates K(+) current by directly coupling with Kv2.1 subunit. *Protein Cell*, **7**(6): 455–460. https://doi.org/10.1007/s13238-016-0276-3

Liu, X., Fu, Y., Yang, H., Mavlyutov, T., Li, J., McCurdy, C. R., Guo, L.-W., & Pattnaik, B. R. 2017. Potential independent action of sigma receptor ligands through inhibition of the Kv2.1 channel. *Oncotarget*, **8**(35): 59345–59358. https://doi.org/10.18632/oncotarget.19581

Liu, X., Constantinescu, S. N., Sun, Y., Bogan, J. S., Hirsch, D., Weinberg, R. A., & Lodish, H. F. (2000). Generation of mammalian cells stably expressing multiple genes at predetermined levels. *Anal Biochem*, **280(**1): 20–28. https://doi.org/10.1006/abio.2000.4478

Long, S. B., Campbell, E. B., & MacKinnon, R. 2005. Voltage sensor of Kv1.2: Structural basis of electromechanical coupling. *Science*, **309**(5736): 903–908. https://doi.org/10.1126/science.1116270

Long, S. B., Tao, X., Campbell, E. B., & MacKinnon, R. 2007. Atomic structure of a voltage-dependent K^+ channel in a lipid membrane-like environment. *Nature*, **450**(7168): 376–382. https://doi.org/10.1038/nature06265

Lopatin, A. N., Makhina, E. N., & Nichols, C. G. 1994. Potassium channel block by cytoplasmic polyamines as the mechanism of intrinsic rectification. *Nature*, **372**(6504): 366–369. https://doi.org/10.1038/372366a0

MacDonald, P. E., Salapatek, A. M. F., & Wheeler, M. B. 2003. Temperature and redox state dependence of native Kv2.1 currents in rat pancreatic beta-cells. *J Physiol*, **546**(Pt 3): 647–653. https://doi.org/10.1113/jphysiol.2002.035709

Maffie, J. K., Dvoretskova, E., Bougis, P. E., Martin-Eauclaire, M.-F., & Rudy, B. 2013. Dipeptidyl-peptidase-like-proteins confer high sensitivity to the scorpion toxin AmmTX3 to Kv4-mediated A-type K^+ channels. *J Physiol*, **591**(10): 2419–2427. https://doi.org/10.1113/jphysiol.2012.248831

Malin, S. A., & Nerbonne, J. M. 2002. Delayed rectifier K currents, I_K, are encoded by Kv2-subunits and regulate tonic firing in mammalian sympathetic neurons. *J Neurosci*, **22**(23): 10094–10105. https://doi.org/10.1523/JNEUROSCI.22-23-10094.2002

Manders, E. M. M., Stap, J., Brakenhoff, G. J., Van Driel, R., & Aten, J. A. 1992. Dynamics of three-dimensional replication patterns during the S-phase, analysed by double labelling of DNA and confocal microscopy. *J Cell Sci*, **103**(3): 857–862.

Mandikian, D., Bocksteins, E., Parajuli, L. K., Bishop, H. I., Cerda, O., Shigemoto, R., & Trimmer, J. S. 2014. Cell type-specific spatial and functional coupling between mammalian brain Kv2.1 K^+ channels and ryanodine receptors. *J Comp Neurol*, **522**(15): 3555–3574. https://doi.org/10.1002/cne.23641

Mardinly, A. R., Oldenburg, I. A., Pégard, N. C., Sridharan, S., Lyall, E. H., Chesnov, K., Brohawn, S. G., Waller, L., & Adesnik, H. 2018. Precise multimodal optical control of neural ensemble activity. *Nat Neurosci*, **21**(6): 881–893. https://doi.org/10.1038/s41593-

018-0139-8
Marionneau, C., Carrasquillo, Y., Norris, A. J., Townsend, R. R., Isom, L. L., Link, A. J., & Nerbonne, J. M. 2012. The sodium channel accessory subunit Nav 1 regulates neuronal excitability through modulation of repolarizing voltage-gated K^+ channels. *J Neurosci*, **32**(17): 5716–5727. https://doi.org/10.1523/JNEUROSCI.6450-11.2012
Maverick, E. E., Leek, A. N., & Tamkun, M. M. 2021. Kv2 channel/AMIGO β-subunit assembly modulates both channel function and cell adhesion molecule surface trafficking. *J Cell Sci*. https://doi.org/10.1242/jcs.256339
McDonald, J. H., & Dunn, K. W. 2013. Statistical tests for measures of colocalization in biological microscopy. *J Microsc*, **252**(3): 295–302. https://doi.org/10.1111/jmi.12093
McEwen, D. P., & Isom, L. L. 2004. Heterophilic interactions of sodium channel beta1 subunits with axonal and glial cell adhesion molecules. *J Biol Chem*, **279**(50): 52744–52752. https://doi.org/10.1074/jbc.M405990200
Meadows, L. S., & Isom, L. L. 2005. Sodium channels as macromolecular complexes: Implications for inherited arrhythmia syndromes. *Cardiovasc Res*, **67**(3): 448–458. https://doi.org/10.1016/j.cardiores.2005.04.003
Messner, D. J., & Catterall, W. A. 1986. The sodium channel from rat brain: Role of the β1 and β2 subunits in saxitoxin binding. *J Biol Chem*, **261**(1): 211–215. http://www.ncbi.nlm.nih.gov/pubmed/2416745
Messner, D. J., Feller, D. J., Scheuer, T., & Catterall, W. A. 1986. Functional properties of rat brain sodium channels lacking the beta 1 or beta 2 subunit. *J Biol Chem*, **261**(32): 14882–14890. http://www.ncbi.nlm.nih.gov/pubmed/2429961
Milescu, M., Bosmans, F., Lee, S., Alabi, A. A., Kim, J. Il, & Swartz, K. J. 2009. Interactions between lipids and voltage sensor paddles detected with tarantula toxins. *Nat Struct Mol Biol*, **16**(10): 1080–1085. https://doi.org/10.1038/nsmb.1679
Misonou, H., Menegola, M., Mohapatra, D. P., Guy, L. K., Park, K.-S., & Trimmer, J. S. 2006. Bidirectional activity-dependent regulation of neuronal ion channel phosphorylation. *J Neurosci*, **26**(52): 13505–13514. https://doi.org/10.1523/JNEUROSCI.3970-06.2006
Misonou, H., Mohapatra, D. P., Menegola, M., & Trimmer, J. S. 2005. Calcium- and metabolic state-dependent modulation of the voltage-dependent Kv2.1 channel regulates neuronal excitability in response to ischemia. *J Neurosci*, **25**(48): 11184–11193. https://doi.org/10.1523/JNEUROSCI.3370-05.2005
Misonou, Hiroaki, Mohapatra, D. P., Park, E. W., Leung, V., Zhen, D., Misonou, K., Anderson, A. E., & Trimmer, J. S. 2004. Regulation of ion channel localization and phosphorylation by neuronal activity. *Nat Neurosci*, **7**(7): 711–718. https://doi.org/10.1038/nn1260
Misonou, Hiroaki, Thompson, S. M., & Cai, X. 2008. Dynamic regulation of the Kv2.1 voltage-gated potassium channel during brain ischemia through neuroglial interaction. *J Neurosci*, **28**(34): 8529–8538. https://doi.org/10.1523/JNEUROSCI.1417-08.2008
Mohapatra, D. P., Misonou, H., Pan, S. J., Held, J. E., Surmeier, D. J., & Trimmer, J. S. 2009. Regulation of intrinsic excitability in hippocampal neurons by activity-dependent modulation of the Kv2.1 potassium channel. *Channels*, **3**(1): 46–56. https://doi.org/7655 [pii]
Moran, O., Nizzari, M., & Conti, F. 2000. Endogenous expression of the β1A sodium channel subunit in HEK-293 cells. *FEBS Lett*, **473**(2): 132–134. https://doi.org/10.1016/S0014-5793(00)01518-0
Moran, O., Traverso, S., Elia, L., & Pusch, M. 2003. Molecular modeling of p-

chlorophenoxyacetic acid binding to the CLC-0 channel. *Biochemistry*, **42**(18): 5176–5185. https://doi.org/10.1021/bi027368o

Morgan, K., Stevens, E. B., Shah, B., Cox, P. J., Dixon, A. K., Lee, K., Pinnock, R. D., Hughes, J., Richardson, P. J., Mizuguchi, K., & Jackson, A. P. 2000. Beta 3: An additional auxiliary subunit of the voltage-sensitive sodium channel that modulates channel gating with distinct kinetics. *Proc Natl Acad Sci U S A*, **97**(5): 2308–2313. https://doi.org/10.1073/pnas.030362197

Mulholland, P. J., Carpenter-Hyland, E. P., Hearing, M. C., Becker, H. C., Woodward, J. J., & Chandler, L. J. 2008. Glutamate transporters regulate extrasynaptic NMDA receptor modulation of Kv2.1 potassium channels. *J Neurosci*, **28**(35): 8801–8809. https://doi.org/10.1523/JNEUROSCI.2405-08.2008

Murakoshi, H., Shi, G., Scannevin, R. H., & Trimmer, J. S. 1997. Phosphorylation of the Kv2.1 K^+ channel alters voltage-dependent activation. *Mol Pharmacol*, **52**(5): 821–828. https://doi.org/10.1124/mol.52.5.821

Nagaya, N., & Papazian, D. M. 1997. Potassium channel alpha and beta subunits assemble in the endoplasmic reticulum. *J Biol Chem*, **272**(5): 3022–3027. https://doi.org/10.1074/jbc.272.5.3022

Nakajo, K., & Kubo, Y. 2015. KCNQ1 channel modulation by KCNE proteins via the voltage-sensing domain. *J Physiol*, **593**(12): 2617–2625. https://doi.org/10.1113/jphysiol.2014.287672

Nguyen, H. M., Miyazaki, H., Hoshi, N., Smith, B. J., Nukina, N., Goldin, A. L., & Chandy, K. G. 2012. Modulation of voltage-gated K^+ channels by the sodium channel 1 subunit. *Proc Natl Acad Sci U S A*, **109**(45): 18577–18582. https://doi.org/10.1073/pnas.1209142109

Niday, Z., & Tzingounis, A. V. 2018. Potassium channel gain of function in epilepsy: An unresolved paradox. *Neuroscientist*, **24**(4): 368–380. https://doi.org/10.1177/1073858418763752

O'Connell, K. M. S., Loftus, R., & Tamkun, M. M. 2010. Localization-dependent activity of the Kv2.1 delayed-rectifier K^+ channel. *Proc Natl Acad Sci U S A*, **107**(27): 12351–12356. https://doi.org/10.1073/pnas.1003028107

Palacio, S., Chevaleyre, V., Brann, D. H., Murray, K. D., Piskorowski, R. A., & Trimmer, J. S. 2017. Heterogeneity in Kv2 channel expression shapes action potential characteristics and firing patterns in CA1 versus CA2 hippocampal pyramidal neurons. *ENeuro*, **4**(4): 1–12. https://doi.org/10.1523/ENEURO.0267-17.2017

Park, J. B., Kim, H. J., Ryu, P. D., & Moczydlowski, E. 2003. Effect of phosphatidylserine on unitary conductance and Ba^{2+} block of the BK Ca^{2+}-activated K^+ channel: Re-examination of the surface charge hypothesis. *J Gen Physiol*, **121**(5): 375–397. https://doi.org/10.1085/jgp.200208746

Park, K.-S., Mohapatra, D. P., Misonou, H., & Trimmer, J. S. 2006. Graded regulation of the Kv2.1 potassium channel by variable phosphorylation. *Science*, **313**(5789): 976–979. https://doi.org/10.1126/science.1124254

Patino, G. A., Claes, L. R. F., Lopez-Santiago, L. F., Slat, E. A., Dondeti, R. S. R., Chen, C., O'Malley, H. A., Gray, C. B. B., Miyazaki, H., Nukina, N., Oyama, F., De Jonghe, P., & Isom, L. L. 2009. A functional null mutation of SCN1B in a patient with Dravet syndrome. *J Neurosci*, **29**(34): 10764–10778. https://doi.org/10.1523/JNEUROSCI.2475-09.2009

Peltola, M. A., Kuja-Panula, J., Lauri, S. E., Taira, T., & Rauvala, H. 2011. AMIGO is an auxiliary subunit of the Kv2.1 potassium channel. *EMBO Rep*, **12**(12): 1293–1299.

https://doi.org/10.1038/embor.2011.204

Peltola, M. A., Kuja-Panula, J., Liuhanen, J., Võikar, V., Piepponen, P., Hiekkalinna, T., Taira, T., Lauri, S. E., Suvisaari, J., Kulesskaya, N., Paunio, T., & Rauvala, H. 2015. AMIGO-Kv2.1 potassium channel complex is associated with schizophrenia-related phenotypes. *Schizophr Bull*, **42**(1): 105. https://doi.org/10.1093/schbul/sbv105

Plant, L. D., Dowdell, E. J., Dementieva, I. S., Marks, J. D., & Goldstein, S. A. N. 2011. SUMO modification of cell surface Kv2.1 potassium channels regulates the activity of rat hippocampal neurons. *J Gen Physiol*, **137**(5): 441–454. https://doi.org/10.1085/jgp.201110604

Ponce, A., Castillo, A., Hinojosa, L., Martinez-Rendon, J., & Cereijido, M. 2018. The expression of endogenous voltage-gated potassium channels in HEK293 cells is affected by culture conditions. *Physiol Rep*, **6**(8): e13663. https://doi.org/10.14814/phy2.13663

Ramu, Y., Xu, Y., & Lu, Z. 2006. Enzymatic activation of voltage-gated potassium channels. *Nature*, **442**(7103): 696–699. https://doi.org/10.1038/nature04880

Rockman, M. E., Vouga, A. G., & Rothberg, B. S. 2020. Molecular mechanism of BK channel activation by the smooth muscle relaxant NS11021. *J Gen Physiol*, **152**(6). https://doi.org/10.1085/jgp.201912506

Romer, S. H., Deardorff, A. S., & Fyffe, R. E. W. 2019. A molecular rheostat: Kv2.1 currents maintain or suppress repetitive firing in motoneurons. *J Physiol*, **597**(14): 3769–3786. https://doi.org/10.1113/JP277833

Sack, J. T., & Aldrich, R. W. 2006. Binding of a gating modifier toxin induces intersubunit cooperativity early in the Shaker K channel's activation pathway. *J Gen Physiol*, **128**(1): 119–132. https://doi.org/10.1085/jgp.200609492

Schindelin, J., Arganda-Carreras, I., Frise, E., Kaynig, V., Longair, M., Pietzsch, T., Preibisch, S., Rueden, C., Saalfeld, S., Schmid, B., Tinevez, J.-Y., White, D. J., Hartenstein, V., Eliceiri, K., Tomancak, P., & Cardona, A. 2012. Fiji: An open-source platform for biological-image analysis. *Nat Methods*, **9**(7): 676–682. https://doi.org/10.1038/nmeth.2019

Schmidt, J. W., & Catterall, W. A. 1986. Biosynthesis and processing of the alpha subunit of the voltage-sensitive sodium channel in rat brain neurons. *Cell*, **46**(3): 437–444. https://doi.org/10.1016/0092-8674(86)90664-1

Scholle, A., Dugarmaa, S., Zimmer, T., Leonhardt, M., Koopmann, R., Engeland, B., Pongs, O., & Benndorf, K. 2004. Rate-limiting reactions determining different activation kinetics of Kv1.2 and Kv2.1 channels. *J Membr Biol*, **198**(2): 103–112. https://doi.org/10.1007/s00232-004-0664-0

Schoppa, N. E., & Sigworth, F. J. 1998. Activation of Shaker potassium channels. I. Characterization of voltage-dependent transitions. *J Gen Physiol*, **111**(2): 271–294. https://doi.org/10.1085/jgp.111.2.271

Shen, H., Liu, D., Wu, K., Lei, J., & Yan, N. 2019. Structures of human Nav1.7 channel in complex with auxiliary subunits and animal toxins. *Science*, **1308**(March): 1303–1308. https://doi.org/10.1126/science.aaw2493

Sigworth, F. J., & Sine, S. M. 1987. Data transformations for improved display and fitting of single-channel dwell time histograms. *Biophys J*, **52**(6): 1047–1054. https://doi.org/10.1016/S0006-3495(87)83298-8

Speca, D. J., Ogata, G., Mandikian, D., Bishop, H. I., Wiler, S. W., Eum, K., Wenzel, H. J., Doisy, E. T., Matt, L., Campi, K. L., Golub, M. S., Nerbonne, J. M., Hell, J. W., Trainor, B. C., Sack, J. T., Schwartzkroin, P. A., & Trimmer, J. S. 2014. Deletion of the Kv2.1 delayed

rectifier potassium channel leads to neuronal and behavioral hyperexcitability. *Genes Brain Behav*, **13**(4): 394–408. https://doi.org/10.1111/gbb.12120

Stewart, R., Cohen, B. E., & Sack, J. T. 2021. Fluorescent toxins as ion channel activity sensors. *Methods Enzymol,* **653:** 295-318. https://doi.org/10.1016/bs.mie.2021.02.014

Sun, J., & MacKinnon, R. 2020. Structural Basis of Human KCNQ1 Modulation and Gating. *Cell*, **180**(2): 340-347.e9. https://doi.org/10.1016/j.cell.2019.12.003

Tao, X., Lee, A., Limapichat, W., Dougherty, D. A., & MacKinnon, R. (2010). A gating charge transfer center in voltage sensors. *Science*, **328**(5974): 67–73. https://doi.org/10.1126/science.1185954

Thapa, P., Stewart, R., Sepela, R. J., Vivas, O., Parajuli, L. K., Lillya, M., Fletcher-Taylor, S., Cohen, B. E., Zito, K., & Sack, J. T. 2021. Optical measurement of voltage sensing by endogenous ion channels. *bioRxiv*, 541805. https://doi.org/10.1101/541805

Thiffault, I., Speca, D. J., Austin, D. C., Cobb, M. M., Eum, K. S., Safina, N. P., Grote, L., Farrow, E. G., Miller, N., Soden, S., Kingsmore, S. F., Trimmer, J. S., Saunders, C. J., & Sack, J. T. 2015. A novel epileptic encephalopathy mutation in KCNB1 disrupts Kv2.1 ion selectivity, expression, and localization. *J Gen Physiol*, **146**(5): 399–410. https://doi.org/10.1085/jgp.201511444

Tilley, D. C., Angueyra, J. M., Eum, K. S., Kim, H., Chao, L. H., Peng, A. W., & Sack, J. T. 2019. The tarantula toxin GxTx detains K^+ channel gating charges in their resting conformation. *J Gen Physiol*, **151**(3): 292–315. https://doi.org/10.1085/jgp.201812213

Tilley, D. C., Eum, K. S., Fletcher-Taylor, S., Austin, D. C., Dupre, C., Patron, L. A., Garcia, R. L., Lam, K., Yarov-Yarovoy, V., Cohen, B. E., & Sack, J. T. (2014). Chemoselective tarantula toxins report voltage activation of wild-type ion channels in live cells. *Proc Natl Acad Sci U S A*, **111**(44): E4789–E4796. https://doi.org/10.1073/pnas.1406876111

Torkamani, A., Bersell, K., Jorge, B. S., Bjork, R. L., Friedman, J. R., Bloss, C. S., Cohen, J., Gupta, S., Naidu, S., Vanoye, C. G., George, A. L., & Kearney, J. A. 2014. De novo KCNB1 mutations in epileptic encephalopathy. *Ann Neurol*, **76**(4): 529–540. https://doi.org/10.1002/ana.24263

Trapani, J. G., Andalib, P., Consiglio, J. F., & Korn, S. J. 2006. Control of single channel conductance in the outer vestibule of the Kv2.1 potassium channel. *J Gen Physiol*, **128**(2): 231–246. https://doi.org/10.1085/jgp.200509465

Trapani, J. G., & Korn, S. J. 2003. Control of ion channel expression for patch clamp recordings using an inducible expression system in mammalian cell lines. *BMC neurosci*, **4**(15). https://doi.org/10.1186/1471-2202-4-15

Trimmer, J. S. 1993. Expression of Kv2.1 delayed rectifier K^+ channel isoforms in the developing rat brain. *FEBS Lett*, **324**(2): 205–210. https://doi.org/10.1016/0014-5793(93)81394-F

Vacher, H., Mohapatra, D. P., & Trimmer, J. S. 2008. Localization and targeting of voltage-dependent ion channels in mammalian central neurons. *Physiol Rev*, **88**(4): 1407–1447. https://doi.org/10.1152/physrev.00002.2008

Vagin, O., Kraut, J. A., & Sachs, G. 2009. Role of N-glycosylation in trafficking of apical membrane proteins in epithelia. *Am J Physiol Renal Physiol*, **296**(3): F459-69. https://doi.org/10.1152/ajprenal.90340.2008

Vierra, N. C., Kirmiz, M., van der List, D., Santana, L. F., & Trimmer, J. S. 2019. Kv2.1 mediates spatial and functional coupling of L-type calcium channels and ryanodine receptors in mammalian neurons. *Elife*, **8**(e49953). https://doi.org/10.7554/eLife.49953

1836 Wang, Y. W., Ding, J. P., Xia, X. M., & Lingle, C. J. 2002. Consequences of the stoichiometry
1837 of Slo1, α and auxiliary β subunits on functional properties of large-conductance Ca^{2+}-
1838 activated K^+ channels. *J Neurosci*, **22**(5): 1550–1561. https://doi.org/10.1523/jneurosci.22-
1839 05-01550.2002
1840 Wilson, M. J., Zhang, M. M., Azam, L., Olivera, B. M., Bulaj, G., & Yoshikami, D. 2011. Navβ
1841 subunits modulate the inhibition of Nav1.8 by the analgesic gating modifier μO-conotoxin
1842 MrVIB. *J Pharmacol Exp Ther*, **338**(2): 687–693. https://doi.org/10.1124/jpet.110.178343
1843 Xu, H., Li, T., Rohou, A., Arthur, C. P., Tzakoniati, F., Wong, E., Estevez, A., Kugel, C.,
1844 Franke, Y., Chen, J., Ciferri, C., Hackos, D. H., Koth, C. M., & Payandeh, J. 2019.
1845 Structural basis of Nav1.7 inhibition by a gating-modifier spider toxin. *Cell*, **176**(4). 702–
1846 715. https://doi.org/10.1016/j.cell.2018.12.018
1847 Yan, J., & Aldrich, R. W. 2012. BK potassium channel modulation by leucine-rich repeat-
1848 containing proteins. *Proc Natl Acad Sci U S A*, **109**(20): 7917–7922.
1849 https://doi.org/10.1073/pnas.1205435109
1850 Yan, Jiusheng, & Aldrich, R. W. 2010. LRRC26 auxiliary protein allows BK channel activation
1851 at resting voltage without calcium. *Nature*, **466**(7305): 513–516.
1852 https://doi.org/10.1038/nature09162
1853 Yu, F. H., Westenbroek, R. E., Silos-Santiago, I., McCormick, K. A., Lawson, D., Ge, P.,
1854 Ferriera, H., Lilly, J., DiStefano, P. S., Catterall, W. A., Scheuer, T., & Curtis, R. 2003.
1855 Sodium channel beta4, a new disulfide-linked auxiliary subunit with similarity to beta2. *J*
1856 *Neurosci*, **23**(20): 7577–7585. https://doi.org/10.1523/JNEUROSCI.23-20-07577.2003
1857 Yu, S. P., & Kerchner, G. A. 1998. Endogenous voltage-gated potassium channels in human
1858 embryonic kidney (HEK293) cells. *J Neurosci Res*, **52**(5): 612–617.
1859 https://doi.org/10.1002/(SICI)1097-4547(19980601)52:5<612::AID-JNR13>3.0.CO;2-3
1860 Zagotta, W. N., Hoshi, T., Dittman, J., & Aldrich, R. W. 1994. Shaker potassium channel gating.
1861 II: Transitions in the activation pathway. *J Gen Physiol*, **103**(2): 279–319.
1862 https://doi.org/10.1085/jgp.103.2.279
1863 Zhang, J., & Yan, J. 2014. Regulation of BK channels by auxiliary γ subunits. *Front Physiol*, **5**:
1864 401. https://doi.org/10.3389/fphys.2014.00401
1865 Zhao, X., Kuja-Panula, J., Sundvik, M., Chen, Y.-C., Aho, V., Peltola, M. A., Porkka-Heiskanen,
1866 T., Panula, P., & Rauvala, H. 2014. Amigo adhesion protein regulates development of
1867 neural circuits in zebrafish brain. *J Biol Chem*, **289**(29): 19958–19975.
1868 https://doi.org/10.1074/jbc.M113.545582
1869

Supplemental Material

Supplemental Figure 1. SCN1β did not detectably modulate Kv2.1 conductance in HEK293 cells.

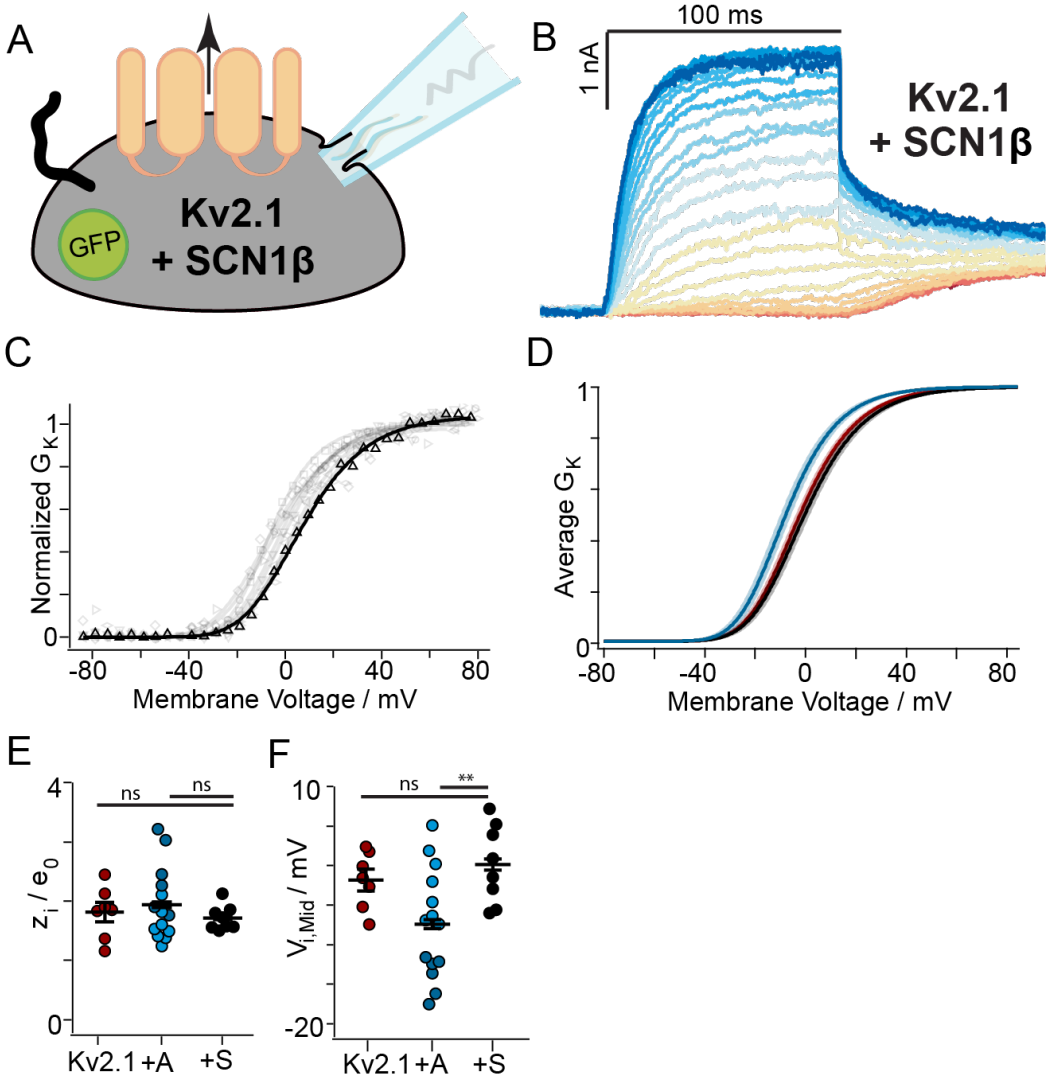

Supplemental Figure 1. SCN1β did not detectably modulate Kv2.1 conductance in HEK293 cells. (**A**) Experimental set up: HEK293 cells were co-transfected 48 hours prior to whole-cell recording with mKv2.1 and SCN1β–pIRES2–GFP (black). Macroscopic K^+ ionic current was recorded (black arrow). Recording solutions are depicted in Fig. 1A. The human voltage–gated sodium channel auxiliary subunit, subtype 1 (SCN1β) was used as a control to assess the effects of overexpressing mKv2.1 with an unrelated single-pass transmembrane protein that contains an extracellular immunoglobulin domain (Isom et al., 1992; Isom & Catterall, 1996; Morgan et al., 2000; Yu et al., 2003). (**B**) Representative Kv2.1 current response elicited from a mKv2.1 + SCN1β (10.0 pF) HEK293 cell. Cells were given 100 ms voltage steps ranging from -80 mV (red) to +85 mV (dark blue) and then stepped to 0 mV to record tail currents. The holding potential was -80 mV. 8 of 27 mKv2.1 + SCN1β cells satisfied our outward I_K density inclusion threshold for analysis (**C**) Normalized *G–V* relationships for mKv2.1 + SCN1β HEK293 cells. Different symbols correspond to individual cells and the bolded trace corresponds to the representative current response shown in panel B. Solid lines represent 4th order Boltzmann relationships (Eqn. C). (**D**) Reconstructed 4th order Boltzmann fits using the average $V_{i,Mid}$ and the average z_i (Table 1). Shaded areas represent $V_{i,Mid}$ ± SEM. (**E**) Steepness and (**F**) midpoint of 4th order Boltzmann fits. Bars are mean ± SEM. SCN1β co-transfection modulates the

function of Nav, $K_V1.1$, $K_V1.2$, $K_V1.3$, $K_V1.6$, $K_V4.2$ and $K_V7.2$ channels (Marionneau et al., 2012; Nguyen et al., 2012), yet, in our study, SCNβ1 gave no indication of mKv2.1 modulation. (**Statistics, E, F**) Unpaired, two-tailed, T–tests p-values are in Table 1. **: p = ≤0.01, ns: not significant.

Supplemental Figure 2. Kv2.1 current density ± AMIGO1 in HEK293 and Kv2.1–CHO cells.

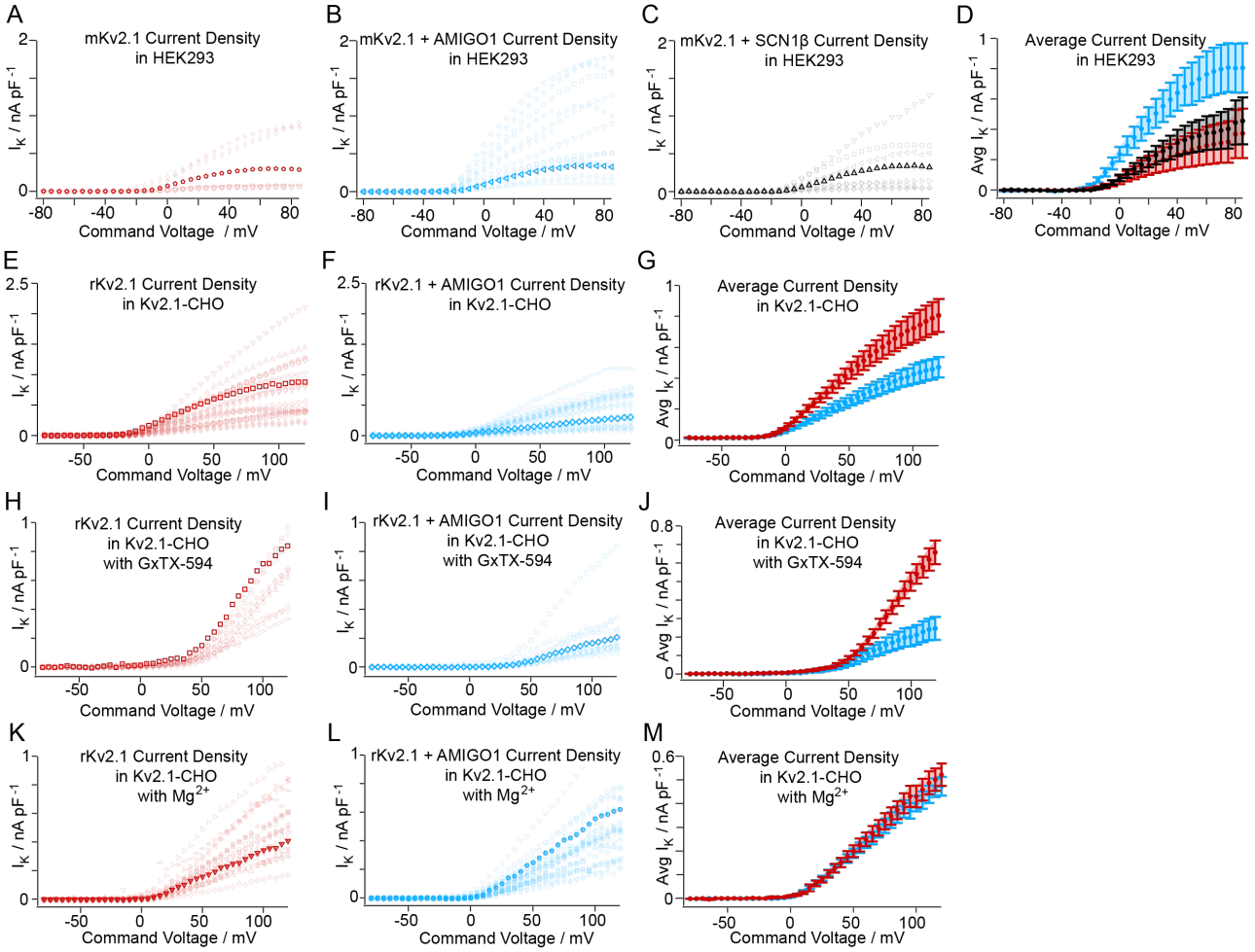

Supplemental Figure 2. Kv2.1 current density ± AMIGO1 in HEK293 and Kv2.1–CHO cells.

AMIGO1 has mixed effects on current density in HEK293 and Kv2.1–CHO cells. Outward current densities normalized by cell capacitance were calculated from mean of the last 10 ms of each voltage step and plotted against the command voltage. Symbols represent individual cells. (**A, B, C respectively**) HEK293 cells co-transfected with mKv2.1 + GFP, mKv2.1 + AMIGO1–pIRES2–GFP, or mKv2.1 SCN1B–pIRES2–GFP. Respectively, 11 of 17, 14 of 28, and 19 of 28 cells that did not meet the inclusion criteria are not pictured. Thus, the full variability of current densities is more extreme than depicted here. Bolded star or triangle data corresponds to exemplar cell shown in Fig. 1B, 1C, and Supplemental Fig. 1C. (**D**) Arithmetic means and standard error for aggregate data in A, B, and C. (**E, F respectively**) Kv2.1–CHO cells transfected with GFP or AMIGO1–YFP and induced for Kv2.1 expression for 1-2 h. Bolded square or diamond data corresponds to exemplar cell shown in Fig. 4B or 4C. (**G**) Arithmetic means and standard error for aggregate data in E and F. (**H, I respectively**) Kv2.1–CHO cells transfected with GFP or with AMIGO1–YFP and induced for Kv2.1 expression for 1-2 h. Recordings were made in 100 nM GxTX–594. Bolded square or diamond corresponds to exemplar cell shown in Fig. 6B or 6C. Unique cells are symbol matched between E/H and F/I to represent the same cell both before and after GxTX–594 addition. (**J**) Arithmetic means and standard error for aggregate data in H and I. (**K, L respectively**) Kv2.1–CHO transfected cells with GFP or AMIGO1–YFP and induced for Kv2.1 expression for 1-2 h. Recordings were made in 3.5 mM K^+/100 mM Mg^{2+} external recording solution. Bolded triangle or circle data corresponds to exemplar cell shown in Fig. 10B or 10C. (**M**) Arithmetic means and standard error for aggregate data in H and I.

Supplemental Figure 3. AMIGO1 does not impede GxTX–594 binding to Kv2.1.

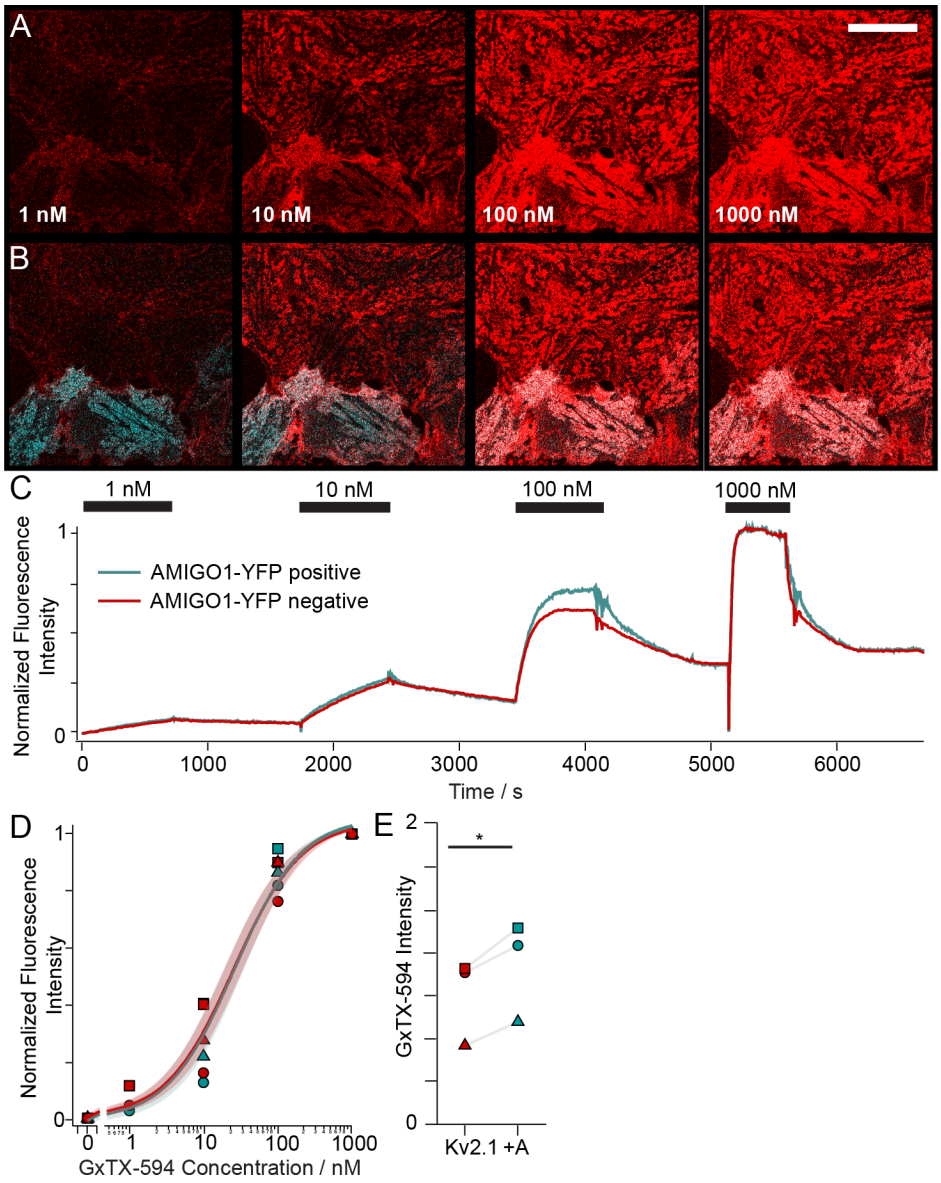

Supplemental Figure 3. AMIGO1 does not impede GxTX–594 binding to Kv2.1.

(**A**) Confocal image of the fluorescence from Kv2.1–CHO cells transfected with AMIGO1–YFP, induced for Kv2.1 expression for 48 hours and labeled with indicated concentrations of the Alexa594 conjugate of GxTX, GxTX–594, (Thapa et al., 2021) (red). In this cell preparation AMIGO1 impacts Kv2.1 voltage sensor movement, consistent with most, if not all Kv2.1 proteins assembling with AMIGO1 (Fig. 7 and Fig. 8). The imaging plane was near the glass-adhered cell membrane surface. Scale bar is 20 μm. (**B**) Overlap (white) between AMIGO1–YFP (cyan) and GxTX–594 fluorescence signals (**C**) Mean fluorescence intensities from ROIs encompassing either all of the AMIGO1–YFP positive or AMIGO1–YFP negative cells from the dose-response experiment shown in A. (**D**) Background-subtracted fluorescence intensity after 500 s at each concentration as in panel C. Symbol shapes represent data from each of 3 experiments. Curves and shaded regions represent the mean ± SEM of a Langmuir binding isotherm (Eqn. K) fit to individual experiments, respectively. K_d = 27.5 ± 8.3 nM without AMIGO1–YFP expression and 27.9 ± 7.2 nM with AMIGO1–YFP. K_d from fits are likely an overestimate due to incomplete equilibration at 1 and 10 nM. (**E**) Cells expressing AMIGO1–YFP had brighter GxTX–594 fluorescence. Symbols are mean GxTX–594 fluorescence intensity values acquired from 1000 nM GxTX–594 labeling. Symbols correspond with D.

1927 Supplemental Table 1. Split Pseudo–Voigt fitting parameters.

GxTX(JP) conjugate	AMIGO1–YFP Expression	fitting component	a0	a1	a2	a3	a4	a5	R^2
GxTX Ser13Pra(JP)	- AMIGO	1	0.229	670.4	47.88	11.41	1.075	2.323	0.999
		2	0.813	647.0	25.73	21.77	0.631	1.685	
	+ AMIGO	1	0.893	646.7	23.30	25.63	1.822	0.721	0.997
		2	0.006	-1610	-15206	-1877	4967	461.2	
GxTX Lys27Pra(JP)	- AMIGO	1	0.352	594.3	12.11	-11.53	0.568	5.364	0.998
		2	0.719	608.2	9.71	59.05	0.359	-0.264	
	+ AMIGO	1	0.715	597.8	16.07	18.08	1.578	2.912	0.997
		2	0.632	616.3	9.05	26.28	-1.657	1.488	

1928 *Supplemental Table 1. Split Pseudo–Voigt fitting parameters.*
1929 Fluorescence emission spectra split pseudo–Voigt fitting parameters and root-mean squared values.